New Approximate Analyses of some Slender Structures: with Hysteresis, Impulsive Loading, and Motion Constraints

A thesis submitted in fulfilment of the requirements

for the degree of Doctor of Philosophy

by

Bidhayak Goswami

18105264

Department of Mechanical Engineering

INDIAN INSTITUTE OF TECHNOLOGY KANPUR

April 2024

CERTIFICATE

It is certified that the work contained in the thesis titled "New Approximate Analyses of some Slender Structures: with Hysteresis, Impulsive Loading, and Motion Constraints" by Bidhayak Goswami has been carried out under my supervision and that this work has not been submitted elsewhere for a degree.

Signature of the Supervisor

Name: Anindya Chatterjee
Department: Mechanical Engg
I.I.T. Kanpur

April, 2024

Declaration

This is to certify that the thesis titled **"New Approximate Analyses of some Slender Structures: with Hysteresis, Impulsive Loading, and Motion Constraints"** has been authored by me. It presents the research conducted by me under the supervision of **Dr. Anindya Chatterjee**.

To the best of my knowledge, it is an original work, both in terms of research content and narrative, and has not been submitted elsewhere, in part or in full, for a degree. Further, due credit has been attributed to the relevant state-of-the-art and collaborations with appropriate citations and acknowledgments, in line with established norms and practices.

Bidhayak Goswami
Roll No. 18105264
Mechanical Engineering Department
Indian Institute of Technology Kanpur
April, 2024

Abstract

Name of the student: **Bidhayak Goswami** Roll No: **18105264**

Degree for which submitted: **PhD** Department: **ME Department**

Thesis title: **New Approximate Analyses of some Slender Structures: with Hysteresis, Impulsive Loading, and Motion Constraints**

Thesis supervisor: **Dr. Anindya Chatterjee**

Month and year of thesis submission: **April 2024**

This thesis presents several almost-independent studies in the dynamics of slender structures. In particular, we are concerned with small vibrations of structures with one independent spatial coordinate along with the usual independent coordinate of time. Slender structures are commonly used in engineering, e.g., beams, columns, struts, chains, and cables. In this thesis we consider only such slender one-dimensional structures. In addition to their practical importance, such slender structures are excellent for purposes of introduction to the dynamics and vibrations of continuous structures in general. Here, we will address several interesting problems involving such structures which have not appeared in either the usually available textbooks or the research literature.

The first problem deals with nonlinear rate independent material damping which is common in structural dynamics. The most common rate independent[1] models are hysteresis models. An extremely popular rate independent hysteresis model used in structural dynamics is the Bouc-Wen model. In the Bouc-Wen model, there are slope discontinuities at each reversal of the rate of deformation. When a refined finite element model is made for a structure with such damping, mesh refinement introduces the further complication of very high natural frequencies. When we attempt to compute dynamic responses for

[1]The energy dissipated during a forcing cycle is independent of the forcing frequency.

such structures, we run into the double difficulty of potential numerical instabilities due to high frequencies as well as numerical difficulties due to the nonsmooth Bouc-Wen model. Here, we propose a semi-implicit time marching algorithm where the structural part is integrated implicitly, and the nonanalytic hysteresis is integrated explicitly. For systems with very many degrees of freedom, we propose a model order reduction technique. Both good stability and good accuracy are obtained, as is demonstrated with several examples.

In the next problem, we examine the short time response of an undamped beam subjected to an instantaneous impulse. In prior work linear impulses, or impulsive forces, have been considered. Here we investigate the response of a beam with rotary inertia effects included, to a concentrated instantaneous moment impulse (or angular impulse). Our study has a reasonable practical motivation, e.g., when a spinning motor with significant inertia, mounted on a long beam, is suddenly brought to a stop. Here, we idealize the problem as a simply supported beam subjected to a moment impulse at its mid span. The time response obtained is an anharmonic[2] series, and we present a detailed asymptotic calculation for the short time approximation of the response. A power series in nondimensionalized time is obtained and verified through detailed direct FEM simulations.

Next, we study the catenary, which is an inextensible chain with zero bending rigidity. We can think of it as a limiting case of an inextensible beam or elastica. We study small in-plane oscillations of a slack catenary suspended between two points under gravity. Due to the pointwise inextensibility, the displacement components are not independent. We expand the vertical displacement component using assumed modes and calculate the horizontal displacement from the inextensibility criterion. The distal end fixity (i.e. the zero displacement condition at the far end) of the obtained displacement is enforced as a constraint on the system, within the Lagrangian approach. Deriving the linearized equations, we observe that the restoring force originates from the end fixity rather than the gravitational potential energy term in the Lagrangian. This problem offers some uncommon

[2]In this context: a series of sinusoidal functions where the frequencies are not integer multiples of a fundamental frequency.

insights into the assumed modes method and constraints in Lagrangian mechanics. It also leads to the next two problems studied, which involve an elastica.

Finally, we consider small motions of an inextensible slender beam with large initial deflection, also known as an elastica. We study the small vibrations of an elastica in pre-bent and constrained configurations. We consider two such problems. In one problem, the elastica is held fixed at one end, then bent and tied to a taut inextensible string at its distal end, fixing that end's distance from a point in space. In the second problem an elastica, pinned at both ends, is bent to form an arch. We use assumed modes and the Lagrangian approach with constraints for both the elastica problems. Excellent performance (as in rapid convergence of the first few natural frequencies) is obtained with a few assumed modes. The role of constraints provides some extensions to the insights obtained from the catenary problem.

In summary, the problems studied in this thesis successively involve non-analytic nonlinear damping, short-time asymptotics, assumed mode approximations, and nontrivial constrained behavior that requires special treatment. Each problem is simplified and idealized, but springs from a practical application. An attempt is made to combine numerical accuracy, analytical rigor, and physical insights in the assessment of each problem.

Acknowledgements

This is my 62nd month at Indian Institute of Technology Kanpur. I am gradually realizing that I will never be able to put what I owe this institute into words. Writing this section of the thesis has been really agonizing. Several times, whenever I have tried to start writing, words have fled leaving me in a pensive sadness. Our well-being is made possible by numerous people working silently and thanklessly. There is a possibility that some names which deserve to be mentioned are missed below. However, I will try to be as complete as I can.

Life as a PhD student at IITK, in some aspects, is easier compared to the students living abroad. We do not have to prepare our food, find rented rooms, take care of the garden, clean our places, or think about our safety. A cup of tea and a plate of hot noodles is easily available even at 2 a.m. In our system, a large number of people work round the clock to pay the price of the leisure in which we gossip, play football, read books, watch movies, play piano, or just sit idle. The summer is unbearably hot over here. We are fortunate enough to have air conditioned classrooms and labs. We have access to uninterrupted electricity and unlimited internet where the town outside the campus witnesses 4 to 6 hours of daily load shedding on an average. I humbly acknowledge the contribution of the mess workers, sanitation workers, gardeners, security guards, maintenance staff, and canteen workers in whatever I have accomplished so far. Most of them had a terrible time during COVID. Yet, they are back with a smiling face. I am grateful to Mishra Ji, Azhar, Dharmendra, Guddu, and Jaan Mohammed for showing up with their autorikshaw even at 3 a.m., and saving me multiple times from missing trains.

I am indebted to Prof. Anindya Chatterjee for agreeing to be my doctoral advisor. I came to IITK with a wish to work with him. I was fascinated by his lectures on Euler angles and linear algebra, and I really liked his approaches to unconventional problems. His clarity of thinking and his ability to put ideas into words are impeccable. I will cherish all the conversations with him; be it in his office or the long walks in the campus. I found his view on statistics (once he told me about fat-tailed distributions) really interesting, and I hope someday he will write it as a paper or maybe as a book. I worked as a teaching assistant with him in most of the semesters and I thoroughly enjoyed it. During this journey, he has been supportive in every possible way. At the time of COVID, every phone call and zoom meeting with him had been therapeutic. Always ready to help troubleshoot

problems, eager to discuss new ideas, and willing to listen to students, he has never shown a sign of annoyance for once. On several occasions, I have taken inexplicably long times to write, made stupid mistakes, and missed deadlines. He always remained strict about the mistakes, and yet forgiving about me.

I thank Prof. Basant Lal Sharma. He taught me the calculus of variations. I did not have training in rigorous mathematics. His course made me delve into topics like functional analysis, abstract algebra, and differential geometry. The semester was interrupted by COVID, and we had to start attending online classes. Nevertheless, the skype discussions on symmetry groups, infinitesimal generators, and Noether conservation laws were really intriguing. I am thankful to Prof. Ishan Shrama. I attended his lectures on granular flows, and tutored the course ESO209 (dynamics) with him as the instructor. He is an incredibly good teacher and an even better thinker. It was an honour that he involved me in the question paper finalization process and asked for my opinion while deciding the grading policies. I thank Prof. Pankaj Wahi and Prof. Anurag Gupta for being helpful on several occasions. I also thank Prof. K. R. Jayaprakash from IIT Gandhinagar for his technical help in a part of my work. I am thankful to Dr. Indrasis Chakraborty. We have not met in person, but I benefited from his work through Prof. Chatterjee. I thank Prof. Mainak Sadhukhan for the amazing time we spent sharing our thoughts on academics, movies, music, and literature.

It is awkward to *thank* our parents and siblings for what they have done for us. Words are insufficient to express such gratitude. I just acknowledge that my father and my mother have helped me realize how difficult it is to become a responsible parent. My elder brother Binayak, to whom I dedicate this thesis, stood by my decision to pursue higher study after quitting a stable job, and single-handedly supported the family. It is a debt that can never be repaid. My sister-in-law Samanwita is extremely kind to me, and she treats me like a child. My cousin Dr. Pinakpani Bhattacharyya, whom I call *Mejda*, has been an unending source of inspiration and enthusiasm.

Finally, coming to my friends, I thank Abhirup, Debnath, Supratik, Arnab, Aritra, and Rony whom I know since my school days. They have always been by my side during hard times. Shauri, a friend since my days in the second standard, is an uncomplaining listener, a wise advisor, and a benevolent taskmaster. I am thankful to my PhD batch mates: Manoj, Deepankar, Debartha, James, Ravi, and Rohit. I express my sincere gratitude to

Ritama, Avideep, Tanay, Hansaraj, Kingshuk, Arnesh, Rajiv, Krishnendu and Soumadeb, my closest friends at IITK. They made all these years worth remembering for the rest of my life.

I thank my seniors Sankalp, Arindam, Ashok, and Abhishek (Ghosh), and also my lab mates Dhananjay, Abdul Hannan, Sourav, and Kundan for their cooperation and companionship.

Before concluding this section I apologize if I have missed any name that deserved to be mentioned here.

Contents

List of Figures

List of Tables

Abbreviations

FEM	**F**inite **E**lement **M**ethod
ODE	**O**rdinary **D**ifferential **E**quation
PDE	**P**artial **D**ifferential **E**quation

List of Publications

Publications from Thesis

1. Paper 1: Semi-implicit integration and data-driven model order reduction in structural dynamics with hysteresis (ASME Journal of Computational and Nonlinear Dynamics, *10.1115/1.4057042*).

2. Paper 2: Short time angular impulse response of Rayleigh beams (Springer Journal of Engineering Mathematics, *10.1007/s10665-023-10302-6*).

3. Paper 3: Small in-plane oscillations of a slack catenary using assumed modes (under review).

Others

1. Paper 1: Balancing a stick with eyes shut: Inverted pendulum on a cart without angle measurement (ASME Journal of Dynamic Systems, Measurement, and Control, *10.1115/1.4056702*).

Dedicated to my elder brother Binayak.

Chapter 1

Introduction

1.1 Motivation

Mechanics of slender structures has a centuries-old strong theoretical foundation. Structural members like beams, chains, and columns have a wide range of applications in various fields, and they are analyzed using well established theories. Such structures very often involve phenomena/situations like rate-independent damping, counter-intuitive transient responses[1], and motion constraints[2] for which the analysis is not straightforward. In such cases conventional methods of analysis may be insufficient. Some such problems are taken up in this thesis.

In this thesis, we present five almost-independent problems involving the dynamics of slender structures. These problems involve hysteretic dissipation, reduced order modeling of nonsmooth high-dimensional systems, the short time impulse response behaviour of slender beams, and vibration characteristics of a slack catenary and as well as two prebent elasticas. The novelty and the academic interest in these problems are described in the next section.

[1] A finite jump discontinuity in the response while its analytical expression is a series of continuous functions.

[2] Constraints forced upon the state variables of a dynamic system.

1.2 Contribution of this thesis

The first problem taken up in this thesis involves hysteretic dissipation in structures. Structural damping is often empirically rate-independent wherein the dissipative part of the stress depends on the history of deformation but not its rate of change. Hysteresis models are popular for rate-independent dissipation; and a popular hysteresis model is the Bouc-Wen model. If such hysteretic dissipation is incorporated in a refined finite element model, then the model involves the usual structural dynamics equations[3] along with nonlinear nonsmooth ordinary differential equations for a large number of internal hysteretic states at Gauss points[4] used within the virtual work calculation. For such systems, numerical integration is difficult due to both the distributed non-analytic nonlinearity[5] of hysteresis as well as large natural frequencies in the finite element model. Here we offer two contributions. First, we present a simple semi-implicit integration approach where the structural part is handled implicitly based on the work of Piché, while the hysteretic part is handled explicitly. A cantilever beam example is solved in detail using high mesh refinement. Convergence is good for lower damping and a smoother hysteresis loop. For a less smooth hysteresis loop and/or higher damping, convergence is noted to be roughly linear on average. Encouragingly, the time step needed for stability is much larger than the time period of the highest natural frequency of the structural model. Subsequently, data from several simulations conducted using the above semi-implicit method are used to construct reduced order models of the system, where the structural dynamics is projected onto a few modes and the number of hysteretic states is reduced significantly as well. Convergence studies of error against the number of retained hysteretic states show very good results. The above study of a hysteretically damped beam is presented in chapter 2 of this thesis.

Chapter 3 of this thesis considers the short-time transient response of a finite-sized vibrating structure. In the dynamics of linear structures, the impulse response function is

[3] Equations of motion written in terms of inertia, stiffness, damping, and forcing.

[4] Gauss point approximation is a method to evaluate integrals in FEA. In the treatment of hysteretic dissipation, a local hysteretic variable is continuously computed at the Gauss points.

[5] Hysteresis is non-smooth in nature as there is a slope change in every reversal of the local strain rate.

of fundamental interest. In some cases one examines the short term response wherein the disturbance is still local and the boundaries have not yet come into play, and for such short-time analysis the geometrical extent of the structure may be taken as unbounded[6]. Here we examine the response of slender beams to angular impulses. The Euler-Bernoulli model, which does not include rotary inertia of cross sections, predicts an unphysical and unbounded initial rotation at the point of application. A finite length Euler-Bernoulli beam, when modeled using finite elements, predicts a mesh-dependent response that shows fast large-amplitude oscillations setting in very quickly. The simplest introduction of rotary inertia yields the Rayleigh beam model, which has more reasonable behavior including a finite wave speed at all frequencies. If a Rayleigh beam is given an impulsive moment at a location away from its boundaries, then the predicted behavior has an instantaneous finite jump in local slope or rotation, followed by smooth evolution of the slope for a finite time interval until reflections arrive from the boundary, causing subsequent slope discontinuities in time. We present a detailed study of the angular impulse response of a simply supported Rayleigh beam, starting with dimensional analysis, followed by modal expansion including all natural frequencies, culminating with an asymptotic formula for the short-time response. The asymptotic formula is obtained by breaking the series solution into two parts to be treated independently term by term, and leads to a polynomial in time. The polynomial matches the response from refined finite element (FE) simulations. In particular, the coefficients of the polynomial depend upon L, the length of the beam, but rapidly approach constant values as L increases.

In the fourth chapter we study a problem in oscillations wherein the assumed modes method offers some theoretical peculiarities. Specifically, we study small in-plane oscillations of a slack catenary, or a sagging inextensible chain fixed at both endpoints. The horizontal and vertical displacements cannot be approximated independently because of pointwise inextensibility in the chain. Moreover, the potential energy is a linear function of the generalized coordinates, and does not directly cause oscillations. Using assumed modes for the vertical displacements only, integrating from one endpoint to compute the required

[6] An infinitely long structure.

horizontal displacements, treating the horizontal fixity at the distal end[7] as an added scalar constraint, and obtaining linearized equations, we construct an eigenvalue problem which contains a Lagrange multiplier. For generic assumed modes, the Lagrange multiplier is determined by enforcing equilibrium in the undeflected shape. However, when the modes thus determined are reinserted in the assumed mode expansion and the calculation done afresh, then the Lagrange multiplier is indeterminate at first order. Upon retaining terms at the next order, the distal end fixity constraint introduces quadratic terms into a Lagrangian without constraints. Results from these two approaches match perfectly. Our approach offers nontrivial insights into both oscillations and Lagrangian mechanics. It is also potentially applicable to other problems with inextensibility in one-dimensional slender members, and we turn to such a problem next.

An *elastica* is an inextensible slender beam that can have large deflections. An elastica "robot" consists of an elastica, fixed at one end with a taut inextensible string tied to its other end with for actuation [1]. In the fifth chapter of this thesis we study the small in-plane oscillations of an elastica robot in a given configuration. We compute natural frequencies and mode shapes of small oscillations of a pre-bent elastica robot where the string remains taut. We use an assumed mode expansion for the slope angle of the beam and formulate the problem as a system with a scalar constraint. Using the Lagrangian formulation, we derive the equations of motion and discuss the role of the constraint in dynamics of this system. In particular, we point out how the choice of a curvilinear coordinate makes this system a little easier to handle than the catenary where Cartesian coordinates were used.

In the sixth chapter, we study the in plane oscillations of an inextensible elastica pinned at both ends, pre-bent to form an arch. We consider an assumed mode expansion for the perturbation about the equilibrium configuration. This system has two fixity constraints at the distal end making it different from the previous two cases. Now the linearized equations of motion have *two* unknown Lagrange multipliers. Physical arguments suggest

[7] The horizontal displacement component at the distal end is zero.

that the approximate solution strategy, and numerical results bear out the validity of the same.

Finally, in chapter 7, we present some concluding remarks.

Chapter 2

Semi-implicit Integration and Model Reduction in Structural Dynamics with Hysteresis

2.1 Introduction

Modelling of damping in materials is a classical problem in structural dynamics, and not a fully solved one. The high dimensionality of structural finite element models combine with the non-analyticity of physically realistic damping models to produce numerical challenges in dynamic simulation. This work makes two contributions in this area. The first contribution, which concerns simple but effective numerical integration, leads to the second contribution, which is in data-driven model order reduction.

Although the linear viscous damping model is simple and convenient, it is not always correct. For many materials subjected to periodic loading, the internal dissipation per cycle is frequency-independent [2]. In the linear viscous damping model the dissipation per cycle is proportional to frequency. Hysteretic dissipation, which is a rate-independent [3] mechanism, is preferred by many structural dynamicists because it is more realistic.

However, hysteresis involves nonanalytic behavior with slope changes at every reversal of loading direction. Numerical integration for structural dynamics with hysteretic damping needs more care than with linear viscous damping. The difficulty grows greatly with finite element models wherein mesh refinement leads to high structural frequencies requiring tiny time steps; and wherein the nonanalytic hysteretic damping is finely resolved in space as well.

In this chapter[1] we first consider time integration of the vibration response for beams[2] with distributed hysteretic damping, and then consider model order reduction by projecting the dynamics onto a few vibration modes. Model order reduction is not trivial in this case because the distributed hysteresis needs to be projected onto lower dimensions as well. Initial numerical solutions of the full system, using a *semi-implicit* integration scheme developed in this chapter, are subsequently used to construct lower order models with hysteretic damping. Our newly introduced integration scheme provides an efficient way to generate the data needed for the second part of the chapter. In principle, other integration methods could be used as well, but they are either more complicated or more slow.

2.1.1 Explicit, implicit, and semi-implicit integration

A key idea in numerical integration of ordinary differential equations (ODEs) is outlined here for a general reader.

We consider ODE systems written in first order form, $\dot{\boldsymbol{y}} = \boldsymbol{f}(\boldsymbol{y}, t)$, where $\boldsymbol{y}$ is a state vector and t is time. In single-step methods, which we consider in this study, we march forward in time by a step h using some algorithm equivalent to

$$\boldsymbol{y}(t+h) = \boldsymbol{y}(t) + h \cdot \boldsymbol{H}(t, h, \boldsymbol{y}(t), \boldsymbol{y}(t+h)). \tag{2.1}$$

Equation 2.1 is merely used to communicate an idea. Hence, we consider $\boldsymbol{y}$, $\boldsymbol{H}$, t, and h dimensionless to avoid unnecessary complications. The specific form of $\boldsymbol{H}$ above is derived

[1] Work presented in chapter 2 has been published in [62].

[2] Our approach extends directly to frames modeled using beam elements. The approach may eventually be generalized to two or three dimensional elements.

from the form of $\boldsymbol{f}(\boldsymbol{y}, t)$ and depends on the integration algorithm. The actual evaluation of $\boldsymbol{H}$ may involve one or multiple stages, but that is irrelevant: the method is single-step in time. For smooth systems, $\boldsymbol{H}$ is guided by the first few terms in Taylor expansions of various quantities about points of interest in the current time step. In such cases, as $h \to 0$, the error in the computed solution goes to zero like h^m for some $m > 0$. If $m > 1$, the convergence is called superlinear. If $m = 2$, the convergence is called quadratic. Values of $m > 2$ are easily possible for smooth systems with moderate numbers of variables: see, e.g., the well known Runge-Kutta methods [4]. Unfortunately, for large structural systems, for the asymptotic h^m rate to hold, h may need to be impractically small. For example, the highest natural frequency of a refined finite element (FE) model for a structure may be, say, 10^6 Hz. This structure may be forced at, say, 10 Hz. A numerical integration algorithm that requires time steps that resolve the highest frequency in the structure, i.e., time steps much smaller than 10^{-6} seconds in this example, is impractical. A high order of convergence that requires time steps smaller than 10^{-6} seconds is of little use. We seek accurate results with time steps much smaller than the forcing period, but much larger than the time period of the highest natural frequency of the FE model of the structure, e.g., 10^{-2} or 10^{-3} seconds. To develop such practically useful algorithms, we must consider the stability of the numerical solution for larger values of h, i.e., $10^{-6} < h < 10^{-2}$, say.

Now consider the nature of $\boldsymbol{H}$. If $\boldsymbol{H}$ does not depend explicitly on $\boldsymbol{y}(t+h)$, the algorithm is explicit. Otherwise it is implicit. For nonlinear systems, $\boldsymbol{H}$ is a nonlinear function of its $\boldsymbol{y}$-arguments. Then each implicit integration step requires iterative solution for $\boldsymbol{y}(t+h)$. For linear dynamics, with $\boldsymbol{H}$ linear in its $\boldsymbol{y}$-arguments, the $\boldsymbol{y}(t+h)$ can be moved over to the left hand side and integration proceeds without iteration, although usually with matrix inversion. The algorithm is still called implicit in such cases: implicitness and iteration are not the same. An algorithm can be neither fully implicit nor fully explicit, and we will present one such algorithm in detail.

2.1.2 Contribution of this study

We present a semi-implicit approach that can be used for high dimensional finite element models with distributed hysteresis. For simplicity, we adopt the popular Bouc-Wen model [5, 6, 7] as our damping mechanism. After presenting and validating our numerical integration method, we present a way to obtain useful lower order models for the structure, starting from a refined FE model. A key issue is that the refined or full FE model computes hysteretic variables at a large number of Gauss points in the structure, and a smaller subset needs to be used for the model order reduction to be practical.

Thus, our contribution is twofold. First, we present a simple semi-implicit algorithm for a structural FE model with distributed hysteresis and demonstrate its convergence and utility. Second, we use this algorithm to compute some responses of the structure and use those responses to construct accurate lower order models with reduced numbers of both vibration modes and hysteretic variables. These lower order models can be used later for quick simulations under similar initial conditions or loading.

2.1.3 Representative literature review

We begin with a review of some numerical integration methods that are available in popular software or research papers.

Structural systems with Bouc-Wen hysteresis continue to be studied in research papers using algorithms that are not as efficient as the one we will present below. For example, as recently as 2019, Vaiana et al. [8] considered a lumped-parameter model and used an explicit time integration method from Chang's family [9]. That method requires tiny time steps: the authors used *one hundredth* of the time period of the highest structural mode. Such small time steps are impractical for refined FE models. Our algorithm allows much larger time steps. Thus, in the area of FE models with distributed hysteresis, our work makes a useful contribution.

Next, we acknowledge that the commercial finite element software Abaqus [10] allows users to specify complex material responses and also to choose between explicit and implicit numerical integration options. For many nonlinear and nonsmooth dynamic problems, explicit integration needs to be used in Abaqus. As outlined above, implicit or semi-implicit algorithms can be useful for somewhat simpler material modeling and in-house FE codes.

Considering general purpose software for numerical work, many analysts dealing with hysteresis may begin with Matlab [11]. Matlab's built in function `ode15s` is designed for stiff systems but not specifically for systems with hysteresis. We have found that `ode15s` can handle ODEs from FE models with a modest number of elements and with hysteresis, but it struggles with higher numbers of elements because its adaptive time steps become too small. In this work we will use `ode15s` to obtain numerically accurate solutions for systems of moderate size. Results obtained from our own algorithm will then be validated against `ode15s` results. Subsequently, for larger systems, our algorithm will continue to work although `ode15s` freezes and/or crashes.

For those programming their own integration routines in structural dynamics, the well known Newmark method [12] from 1959 remains popular (see, e.g., [13, 14]), although it cannot guarantee stability and may require tiny time steps as noted in, e.g., [15]. In that paper [15] of 1977, Hilber, Hughes and Taylor modified the Newmark method and showed unconditional stability for linear structural problems. However, their method (known as HHT-α) can show spurious oscillations of higher modes even without hysteretic damping (see, e.g., Fig. 7 of the paper by Piché [32], which we will take up below).

An appreciation of the issues faced for full three-dimensional (3D) simulation with hysteretic damping can be gained, e.g., from the work of Triantafyllou and Koumousis [16]. Their formulation is actually based on plasticity in 3D; they compare their solutions with those from Abaqus; and they include dynamics through the Newmark algorithm. Their algorithm is rather advanced for a typical analyst to implement quickly. Note that our present application is easier than theirs because we have only one-dimensional Bouc-Wen

hysteresis. Additionally, our primary application here is in model order reduction. And so we develop for our current use a numerical integration approach that is simpler than that in [16].

Finally, readers interested in hybrid simulations (with an experimental structure in the loop) may see, e.g., Mosqueda and Ahmadizadeh [17, 18] who used a modified version of the HHT-α for calculating the seismic response of a multi-degree-of-freedom structure. Purely simulation-based studies such as the present one can hopefully provide theoretical inputs into planning for such hybrid simulations in future work.

We close this section with a brief discussion of model order reduction. While there are very many papers on the topic, we make special note of the condensation approaches of Guyan [19] and Irons [20], wherein finding normal modes of the full system was avoided. With growth in computational power, system eigenvectors become more easily available, and direct modal projection has become common. For a recent discussion of this and related methods, see [21]. We will use straightforward modal projection for our displacement degrees of freedom. However, we will also have a large number of internal hysteretic state variables. We will present a sequential approach to selecting a subset of these hysteretic variables, using an algorithm which is related closely to a method called "QR with column pivoting" in [22]. Minor differences from [22] here are that we work with rows and not columns, and our data matrix is not rank deficient: we separately impose a termination criterion.

Note that modal reduction, without the added complication of hysteretic damping, is well known. For example, Stringer et al. [23, 24] successfully applied modal reduction to rotor systems, including ones with gyroscopic effects. Other recent examples in dynamics and vibrations can be seen in [25, 26]. Proper Orthogonal Decomposition (POD) [27] based reduced order models are often used in fluid mechanics: a representative sample may be found in [28, 29, 30, 31].

2.1.4 Overview of our approach

We will begin by adopting an existing implicit scheme for linear structural dynamics without hysteresis that is both simple and significantly superior to both the Newmark and HHT-α methods. Our adopted scheme, due to Piché [32], is an L-stable method from the Rosenbrock family (see [33] and references therein) which is stable, implicit without iteration for linear structures, and second order accurate. For smooth nonlinear systems of the form

$$\mathbf{M}\ddot{\boldsymbol{x}} + \boldsymbol{f}(\boldsymbol{x}, \dot{\boldsymbol{x}}) = \mathbf{0},$$

Piché suggests a one-time linearization of $\boldsymbol{f}$ at the start of each time step. We will not use that linearization step because hysteresis is nonsmooth.

Here we extend Piché's formulation to include hysteretic damping in the otherwise-linear structural dynamics. In our method the stiffness and inertia terms are integrated implicitly (without iteration, being linear) and the nonsmooth hysteresis is monitored at Gauss points [34] and treated with explicit time-integration. Thus, overall, our method is semi-implicit. Our proposed approach, when applied to a refined FE model of an Euler-Bernoulli beam with distributed Bouc-Wen hysteretic damping, is easy to implement and can be dramatically faster than Matlab's `ode15s`. In fact, it continues to work well beyond refinement levels where `ode15s` stops working.

We emphasize that `ode15s` is not really designed for such systems. We use it here because it has adaptive step sizing and error estimation: when it does work, it can be highly accurate. For this reason, to examine the performance of our algorithm for modest numbers of elements, we will use results obtained from `ode15s` with a tight error tolerance. With higher number of elements, `ode15s` fails to run because the time steps required become too small.

Having shown the utility of our proposed semi-implicit integration algorithm, we will turn to our second contribution of this chapter, namely model order reduction. Such Reduced Order Models (ROMs) can save much computational effort. In the physical system, if

only a few lower modes are excited, the displacement vector can be approximated as a time-varying linear combination of those modes only. A remaining issue here is that the number of Gauss points used for the hysteresis can be reduced too, and that is where we offer an additional contribution.

In recent work related to ours, for an Euler-Bernoulli beam with hysteretic dissipation, Maity et al. [34] used the first few undamped analytically obtained modes to approximate the solution and performed the virtual work integration using a few Gauss points chosen over the full domain. However, they used a different hysteresis model motivated by distributed microcracks. Furthermore, in our finite element model, virtual work integrations are performed over individual elements and not the whole domain. The number of Gauss points in the finite element model increases with mesh refinement. When we project the response onto a few modes, we can explicitly reduce the number of Gauss points retained as well, and a practical method of doing so is one of the contributions of this chapter.

In what follows, we present the finite element model in section 2.2, outline the numerical integration algorithm in section 2.3, develop the approach for model order reduction in section 2.4, and present our results in section 2.5.

2.2 Governing equations and Finite Element formulation

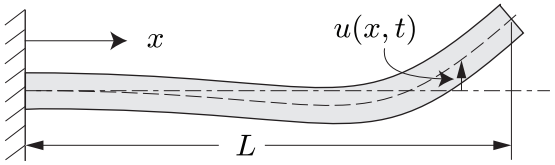

FIGURE 2.1: A cantilever beam.

The governing equation of the deflection $u(x,t)$ of a cantilever beam (shown in Fig. 2.1) with a dissipative bending moment $M_{\mathrm{d}} = \gamma_{\mathrm{h}} z(x,t)$ is

$$\rho A \frac{\partial^2 u}{\partial t^2} + \frac{\partial^2}{\partial x^2}\left(EI \frac{\partial^2 u}{\partial x^2} + \gamma_{\mathrm{h}} z \right) = 0, \tag{2.2}$$

where the beam's material density, cross section and flexural rigidity are ρ, A and EI respectively. The parameter γ_{h} is the strength of hysteretic dissipation. The hysteretic damping variable z is defined at each x-location along the beam length, is governed pointwise by the Bouc-Wen model, and is driven pointwise by the local curvature

$$\chi(x,t) \approx \frac{\partial^2 u}{\partial x^2}$$

in the governing equation

$$\dot{z} = \left(\bar{A} - \alpha \,\mathrm{sign}\left(\dot{\chi}\, z\right) |z|^{n_{\mathrm{h}}} - \beta \,|z|^{n_{\mathrm{h}}}\right) \dot{\chi} \tag{2.3}$$

where the Bouc-Wen model parameters satisfy

$$\bar{A} > 0,\ \alpha > 0,\ \beta \in (-\alpha, \alpha) \text{ and } n_{\mathrm{h}} > 0. \tag{2.4}$$

The parameters in Eq. 2.4 and the hysteretic variable z are dimensionless. The dissipation strength parameter γ_{h} has units of Nm (i.e., units of moments).

The FE model involves beam elements for displacement variables, virtual work calculations for the hysteretic moment through domain integrals based on Gauss points within each element, and ODE solution in time. We use the Galerkin method wherein we look for an admissible solution $\hat{u}(x,t)$ so that the residual,

$$\mathcal{R}(\hat{u}) = \rho A \frac{\partial^2 \hat{u}}{\partial t^2} + \frac{\partial^2}{\partial x^2}\left(EI \frac{\partial^2 \hat{u}}{\partial x^2} + \gamma_{\mathrm{h}} z\right), \tag{2.5}$$

is orthogonal to basis functions for the space of $\hat{u}$. Mathematically,

$$< \mathcal{R}(\hat{u}), \phi_i > = \int_\Omega \mathcal{R}(\hat{u}) \phi_i(x)\, \mathrm{d}\Omega = 0, \tag{2.6}$$

where

$$< f_1, f_2 > = \int_\Omega f_1(x) f_2(x)\, \mathrm{d}\Omega$$

is the inner product between two functions, Ω is the spatial domain over which the basis functions are defined, and ϕ_i is the i^{th} basis function.

2.2.1 Element matrices and virtual work integrals

The elemental stiffness and inertia matrices are routine and given in many textbooks: each beam element has two nodes, and each node has one translation and one rotation. The hysteresis variable z is a scalar quantity distributed in space. However, it enters the discretized equations through integrals, and so z values only need to be known at Gauss points within each element. The evolution of z at the Gauss points is computed using Eq. 2.3, and is thus driven by displacement variables. Some further details are given in appendix A.

2.2.2 Global equations

In this section we first present the global equations, and then we introduce the variables and constants that appear in those equations. The element level formulation details are given in appendix A.

After assembly we obtain a system of equations of the form

$$\underset{\text{Mass}}{\mathbf{M}\,\ddot{\boldsymbol{q}}} + \underset{\text{Stiffness}}{\mathbf{K}\,\boldsymbol{q}} + \underset{\text{Hysteresis}}{\mathbf{A}\,\boldsymbol{z}} = \underset{\text{Forcing}}{\boldsymbol{f}_0(t)}\,, \tag{2.7a}$$

where $\mathbf{A} \in \mathbb{R}^{N \times n_{\text{g}} n_{\text{e}}}$, $\boldsymbol{q} \in \mathbb{R}^N$, and $\boldsymbol{z} \in \mathbb{R}^{n_{\text{g}} n_{\text{e}}}$. The hysteresis rate equations are given by

$$\dot{\boldsymbol{z}} = (\bar{A} - \alpha\,\text{sign}(\dot{\boldsymbol{\chi}} \circ \boldsymbol{z}) \circ |\boldsymbol{z}|^{\circ\, n_{\text{h}}} - \beta\,|\boldsymbol{z}|^{\circ\, n_{\text{h}}}) \circ \dot{\boldsymbol{\chi}},\ \boldsymbol{\chi} = \mathbf{B}\,\boldsymbol{q}, \tag{2.7b}$$

where $\mathbf{B} \in \mathbb{R}^{n_{\text{e}} n_{\text{g}} \times N}$ and the different symbols mean the following:

1. $\boldsymbol{q}$ is a column vector of nodal displacements and rotations for n_{e} beam elements, with $N = 2n_{\text{e}}$ for a cantilever beam,

2. $\mathbf{M}$ and $\mathbf{K}$ are mass and stiffness matrices of size $2\,n_\mathrm{e} \times 2\,n_\mathrm{e}$,

3. $\boldsymbol{z}$ is a column vector of length $n_\mathrm{g} n_\mathrm{e}$ from n_g Gauss points per element,

4. $(\cdot \circ \cdot)$ and $(\cdot)^{\circ\,(\cdot)}$ denote elementwise multiplication and exponentiation,

5. $\mathbf{A}$ is a matrix of weights used to convert $\boldsymbol{z}$ values into virtual work integrals,

6. $\boldsymbol{\chi}$ is a column vector of curvatures at the Gauss points,

7. $\mathbf{B}$ maps nodal displacements and rotations $\boldsymbol{q}$ to curvatures $\boldsymbol{\chi}$ at the Gauss points, and

8. $\boldsymbol{f}_0(t)$ incorporates applied forces.

In Eq. 2.7a above we can include viscous damping by adding $\mathbf{C}\,\dot{\boldsymbol{q}}$, for some suitable $\mathbf{C}$, on the left hand side. As this work focuses on hysteretic damping, we have taken $\mathbf{C} = \mathbf{0}$.

2.3 Time integration

We will develop a semi-implicit method adapted from Piché's [32] work. Equation 2.7a has a structural part (stiffness and inertia) and a hysteresis part. The structural part is integrated implicitly (section 2.3.1) and the hysteresis part marches in time, following an explicit algorithm which takes care of the nonsmooth slope changes due to zero-crossing of the time derivative of the curvature (section 2.3.2). In section 2.4, our semi-implicit algorithm will be used to generate a large amount of data which will be used to construct reduced order models.

2.3.1 Implicit integration for the structural part

Piché's algorithm uses a numerical parameter $1 - \frac{1}{\sqrt{2}}$ which is written as γ for compact presentation. The symbol should not be confused for Euler's constant. We now proceed as follows. This subsection presents implicit integration for the structural part alone: the

hysteretic variable vector $\boldsymbol{z}$ is not integrated in an implicit step: this compromise simplifies the algorithm greatly.

1. Define

$$\boldsymbol{z}(t_0) = \boldsymbol{z}_0, \quad \boldsymbol{F}_0 = -\mathbf{A}\boldsymbol{z}_0 + \boldsymbol{f}_0(t_0),$$

$$\boldsymbol{y}_0 = \boldsymbol{q}(t_0), \quad \boldsymbol{v}_0 = \dot{\boldsymbol{q}}(t_0), \quad \dot{\boldsymbol{\chi}}_0 = \mathbf{B}\boldsymbol{v}_0,$$

$$\dot{\boldsymbol{z}}_0 = \left(\bar{A} - \alpha\,\mathrm{sign}(\dot{\boldsymbol{\chi}}_0 \circ \boldsymbol{z}_0) \circ |\boldsymbol{z}_0|^{\circ n_\mathrm{h}} - \beta\,|\boldsymbol{z}_0|^{\circ n_\mathrm{h}}\right) \circ \dot{\boldsymbol{\chi}}_0,$$

$$\dot{\boldsymbol{F}}_0 = -\mathbf{A}\dot{\boldsymbol{z}}_0 + \frac{\mathrm{d}}{\mathrm{d}t}\boldsymbol{f}_0(t)\bigg|_{t=t_0},$$

$$\boldsymbol{r}_0 = \mathbf{K}\boldsymbol{y}_0 + \mathbf{C}\boldsymbol{v}_0$$

   (The $\mathbf{C}\boldsymbol{v}_0$ is dropped if linear viscous damping is no included.)

2. Define

$$\tilde{\mathbf{M}} = \mathbf{M} + \gamma h\mathbf{C} + (\gamma h)^2\,\mathbf{K}.$$

3. Define (first stage)

$$\tilde{\boldsymbol{e}} = h\,\tilde{\mathbf{M}}^{-1}\left(\boldsymbol{F}_0 - \boldsymbol{r}_0 + h\gamma(\dot{\boldsymbol{F}}_0 - \mathbf{K}\boldsymbol{v}_0)\right).$$

$$\tilde{\boldsymbol{d}} = h(\boldsymbol{v}_0 + \gamma\tilde{\boldsymbol{e}}).$$

4. Define (second stage)

$$\boldsymbol{F}_{\frac{1}{2}} = -\mathbf{A}\left(\boldsymbol{z}_0 + \frac{h}{2}\dot{\boldsymbol{z}}_0\right) + \boldsymbol{f}_0\left(t_0 + \frac{1}{2}\,h\right),$$

$$\boldsymbol{r}_{\frac{1}{2}} = \mathbf{K}\left(\boldsymbol{y}_0 + \frac{1}{2}\,\tilde{\boldsymbol{d}}\right) + \mathbf{C}\left(\boldsymbol{v}_0 + \frac{1}{2}\,\tilde{\boldsymbol{e}}\right),$$

$$\boldsymbol{e} = h\tilde{\mathbf{M}}^{-1}\left(\boldsymbol{F}_{\frac{1}{2}} - \boldsymbol{r}_{\frac{1}{2}} + (h\gamma)\left(2\gamma - \frac{1}{2}\right)\mathbf{K}\tilde{\boldsymbol{e}} + \gamma\mathbf{C}\tilde{\boldsymbol{e}}\right),$$

   and

$$\boldsymbol{d} = h\left(\boldsymbol{v}_0 + \left(\frac{1}{2} - \gamma\right)\tilde{\boldsymbol{e}} + \gamma\boldsymbol{e}\right).$$

5. Finally

$$\boldsymbol{y}(t_0 + h) = \boldsymbol{y}_0 + \boldsymbol{d}, \qquad \boldsymbol{v}(t_0 + h) = \boldsymbol{v}_0 + \boldsymbol{e}.$$

6. Define

$$\dot{\boldsymbol{\chi}}_1 = \dot{\boldsymbol{\chi}}(t_0 + h) = \mathbf{B}(\boldsymbol{v}_0 + \boldsymbol{e})$$

Note that the assignment of $\dot{\boldsymbol{\chi}}_1$ to $\dot{\boldsymbol{\chi}}(t_0 + h)$ above is tentative at this stage; if there is a sign change, we will make a correction, as discussed in the next subsection.

2.3.2 Explicit integration for the hysteretic part

Due to the nonanalyticity of hysteresis models, we integrate the hysteresis part using an explicit step. There are slope changes in the hysteretic response whenever $\dot{\chi}$ at any Gauss point crosses zero in time. We will accommodate the sign change of $\dot{\chi}$ within an explicit time step in a second sub-step, after first taking a time step assuming that there is no sign change. Since each $\dot{z}_i$ depends on $\dot{\chi}_i$ only, accounting for zero crossings can be done individually for individual Gauss points and after such a preliminary step.

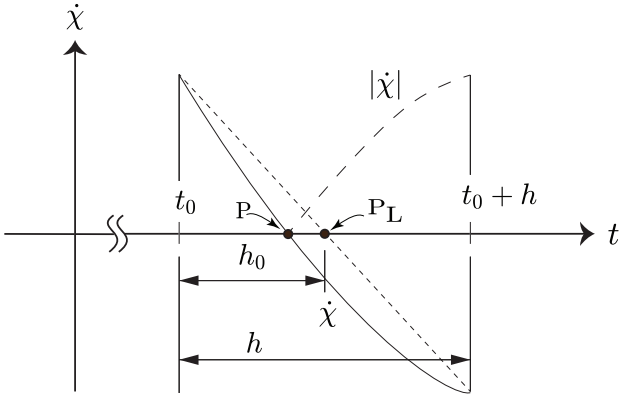

FIGURE 2.2: Zero-crossing of $\dot{\chi}$ at any particular Gauss point within a time step. For details on associated quantities shown, see the main text.

We first check elementwise and identify the entries of $\dot{\boldsymbol{\chi}}_0$ and $\dot{\boldsymbol{\chi}}_1$ that have same sign, and construct sub-vectors $\dot{\boldsymbol{\chi}}_{0\mathrm{u}}$ and $\dot{\boldsymbol{\chi}}_{1\mathrm{u}}$ out of those entries. The corresponding elements from the vector $\boldsymbol{z}_0$ are used to construct a sub-vector $\boldsymbol{z}_{0\mathrm{u}}$. Here the subscript "u" stands for "unchanged". These elements can be used in a simple predictor-corrector step for

improved accuracy as follows.

$$\boldsymbol{s}_1 = \left(\bar{A} - \alpha\,\mathrm{sign}(\dot{\boldsymbol{\chi}}_{0\mathrm{u}} \circ \boldsymbol{z}_{0\mathrm{u}}) \circ |\boldsymbol{z}_{0\mathrm{u}}|^{\circ n_\mathrm{h}} - \beta\,|\boldsymbol{z}_{0\mathrm{u}}|^{\circ n_\mathrm{h}}\right) \circ \dot{\boldsymbol{\chi}}_{0\mathrm{u}},$$

$$\boldsymbol{z}_{\mathrm{iu}} = \boldsymbol{z}_{0\mathrm{u}} + h\boldsymbol{s}_1,$$

$$\boldsymbol{s}_2 = \left(\bar{A} - \alpha\,\mathrm{sign}(\dot{\boldsymbol{\chi}}_{1\mathrm{u}} \circ \boldsymbol{z}_{\mathrm{iu}}) \circ |\boldsymbol{z}_{\mathrm{iu}}|^{\circ n_\mathrm{h}} - \beta\,|\boldsymbol{z}_{\mathrm{iu}}|^{\circ n_\mathrm{h}}\right) \circ \dot{\boldsymbol{\chi}}_{1\mathrm{u}},$$

and

$$\boldsymbol{z}_{1\mathrm{u}} = \boldsymbol{z}_{0\mathrm{u}} + h\,\frac{(\boldsymbol{s}_1 + \boldsymbol{s}_2)}{2}. \tag{2.8}$$

Next, we address the remaining entries of $\dot{\boldsymbol{\chi}}_0$ and $\dot{\boldsymbol{\chi}}_1$, those that have crossed zero and flipped sign. We construct sub-vectors $\dot{\boldsymbol{\chi}}_{0\mathrm{f}}$ and $\dot{\boldsymbol{\chi}}_{1\mathrm{f}}$ out of them, where the "f" subscript stands for "flipped". The corresponding elements from the vector $\boldsymbol{z}_0$ are used to construct sub-vector $\boldsymbol{z}_{0\mathrm{f}}$. Using linear interpolation to approximate the zero-crossing instants within the time step, we use

$$\boldsymbol{h}_0 = -h\,\frac{\dot{\boldsymbol{\chi}}_{0\mathrm{f}}}{(\dot{\boldsymbol{\chi}}_{1\mathrm{f}} - \dot{\boldsymbol{\chi}}_{0\mathrm{f}})} \quad \text{(defined elementwise)}.$$

We define

$$\boldsymbol{s}_1 = \left(\bar{A} - \alpha\,\mathrm{sign}(\dot{\boldsymbol{\chi}}_{0\mathrm{f}} \circ \boldsymbol{z}_{0\mathrm{f}}) \circ |\boldsymbol{z}_{0\mathrm{f}}|^{\circ n_\mathrm{h}} - \beta\,|\boldsymbol{z}_{0\mathrm{f}}|^{\circ n_\mathrm{h}}\right) \circ \dot{\boldsymbol{\chi}}_{0\mathrm{f}},$$

and

$$\boldsymbol{z}_{\mathrm{mf}} = \boldsymbol{z}_{0\mathrm{f}} + \boldsymbol{h}_0 \circ \frac{\boldsymbol{s}_1}{2},$$

which is consistent with Eq. 2.8 because $\dot{\boldsymbol{\chi}} = \boldsymbol{0}$ at the end of the sub-step. Next we complete the step using

$$\boldsymbol{s}_2 = \left(\bar{A} - \alpha\,\mathrm{sign}(\dot{\boldsymbol{\chi}}_{1\mathrm{f}} \circ \boldsymbol{z}_{\mathrm{mf}}) \circ |\boldsymbol{z}_{\mathrm{mf}}|^{\circ n_\mathrm{h}} - \beta\,|\boldsymbol{z}_{\mathrm{mf}}|^{\circ n_\mathrm{h}}\right) \circ \dot{\boldsymbol{\chi}}_{1\mathrm{f}}$$

and

$$\boldsymbol{z}_{1\mathrm{f}} = \boldsymbol{z}_{\mathrm{mf}} + (\boldsymbol{h} - \boldsymbol{h}_0) \circ \frac{\boldsymbol{s}_2}{2}$$

where $\boldsymbol{h}$ is a vector of the same dimensions as $\boldsymbol{h}_0$ and with all elements equal to h. Finally, having the incremented values $\boldsymbol{z}_1$ at all locations, those with signs unchanged and those with signs flipped, we use

$$\boldsymbol{z}(t_0 + h) = \boldsymbol{z}_1.$$

We clarify that the explicit integration of the hysteretic variables, as outlined in this subsection, is a compromise adopted to avoid difficulties due to the nonanalyticity of the hysteresis model. Continuing to integrate the inertia and stiffness parts implicitly will still allow us to use usefully large steps, as will be seen in section 2.5.

Having the numerical integration algorithm in place, however, we must now turn to the second contribution of this chapter, namely model order reduction.

2.4 Model order reduction

For reduced order modeling, we must reduce both the number of active vibration modes as well as the number of Gauss points used to compute the hysteretic dissipation. Of these two, the first is routine.

2.4.1 Reduction in the number of vibration modes

The undamped normal modes and natural frequencies are given by the eigenvalue problem

$$(\mathbf{K} - \omega^2 \mathbf{M})\boldsymbol{v} = \mathbf{0} \tag{2.9}$$

for N eigenvector-eigenvalue pairs $(\boldsymbol{v}_i, \omega_i)$. In a finely meshed FE model, N is large. In such cases, we may compute only the first several such pairs using standard built-in iterative routines in software packages.

The N dimensional displacement vector $\boldsymbol{q}$ is now approximated as a linear combination of $r \ll N$ modes. To this end, we construct a matrix $\mathbf{R}$ with the first r eigenvectors as

columns so that

$$\boldsymbol{q}(t) \approx \sum_{k=1}^{r} \boldsymbol{v}_k \, \xi_k(t) = \mathbf{R}\, \boldsymbol{\xi}(t), \tag{2.10}$$

where $\mathbf{R} = [\boldsymbol{v}_1 \;\; \boldsymbol{v}_2 \; \ldots \; \boldsymbol{v}_r]$, and where the elements of $\boldsymbol{\xi}(t)$ are called modal coordinates. Substituting Eq. 2.10 in Eq. 2.7a and pre-multiplying with the transposed matrix $\mathbf{R}^\top$, we obtain

$$\mathbf{R}^\top \mathbf{M}\, \mathbf{R}\, \ddot{\boldsymbol{\xi}} + \mathbf{R}^\top \mathbf{K}\, \mathbf{R}\, \boldsymbol{\xi} + \mathbf{R}^\top \mathbf{A}\, \boldsymbol{z} = \mathbf{R}^\top \boldsymbol{f}_0(t), \tag{2.11}$$

obtaining equations of the form

$$\tilde{\mathbf{M}}\, \ddot{\boldsymbol{\xi}} + \tilde{\mathbf{K}}\, \boldsymbol{\xi} + \mathbf{R}^\top \mathbf{A}\, \boldsymbol{z} = \mathbf{R}^\top \boldsymbol{f}_0(t), \tag{2.12a}$$

$$\dot{\boldsymbol{z}} = (\bar{A} - \alpha \, \mathrm{sign}(\dot{\boldsymbol{\chi}}_\mathrm{a} \circ \boldsymbol{z}) \circ |\boldsymbol{z}|^{\circ n_\mathrm{h}} - \beta \, |\boldsymbol{z}|^{\circ n_\mathrm{h}}) \circ \dot{\boldsymbol{\chi}}_\mathrm{a}, \;\; \dot{\boldsymbol{\chi}}_\mathrm{a} = \mathbf{B}\mathbf{R}\dot{\boldsymbol{\xi}}. \tag{2.12b}$$

In the above, due to orthogonality of the normal modes, the matrices $\tilde{\mathbf{M}}$ and $\tilde{\mathbf{K}}$ are diagonal. Also, $\boldsymbol{\chi}_\mathrm{a}$ is an approximation of the original $\boldsymbol{\chi}$ because we have projected onto a few vibration modes, but it still has the same number of elements as $\boldsymbol{\chi}$ and requires numerical integration of the same number of nonsmooth hysteresis equations. A reduction in the number of hysteretic variables is necessary.

2.4.2 Reduction in the number of hysteretic variables

The system still has a large number ($n_\mathrm{g} n_\mathrm{e}$) of hysteretic damping variables. These are arranged in the elements of $\boldsymbol{z}$ in Eq. 2.7a. Selecting a smaller set of basis vectors and projecting the dynamics of the evolving $\boldsymbol{z}$ onto those has analytical difficulties. Here we adopt a data-driven approach to select a submatrix of $\boldsymbol{z}$, say

$$\boldsymbol{z}_\mathrm{s} = [z_{j_1} \; z_{j_2} \; \ldots, z_{j_m}]^\top, \; m \ll n_\mathrm{g} n_\mathrm{e}. \tag{2.13}$$

The indices j_1, j_2, $\ldots j_m$ must now be chosen from the set $\{1, 2, \ldots, n_\mathrm{e} n_\mathrm{g}\}$, along with a matrix $\mathbf{P}$, such that

$$\mathbf{P}\boldsymbol{z}_\mathrm{s}(t) \approx \mathbf{R}^\top \mathbf{A}\, \boldsymbol{z}(t). \tag{2.14}$$

Working with that reduced set of hysteretic variables, we will be able use a reduced set of driving local curvatures

$$\dot{\boldsymbol{\chi}}_{\mathrm{s}} = [\dot{\chi}_{\mathrm{a}_{j_1}}\ \dot{\chi}_{\mathrm{a}_{j_2}}\ \cdots\ \dot{\chi}_{\mathrm{a}_{j_m}}]^{\top}, \tag{2.15}$$

a submatrix of $\dot{\boldsymbol{\chi}}_{\mathrm{a}}$. In other words, we will work with a subset of the original large number of Gauss points used to compute virtual work integrals for the hysteretic dissipation. In our proposed data-driven approach, selection of the indices j_1, j_2, $\ldots j_m$ is the only significant issue. The matrix $\mathbf{P}$ can then be found by a simple matrix calculation.

However, for implementing our approach, we must first generate a sufficiently large amount of data using numerical integration of the full equations with representative initial conditions and/or forcing.

These initial conditions are randomly generated as follows. The hysteretic states are uniformly distributed random numbers in the interval (0, 0.1). For the displacement and rotation degrees of freedom, the initial conditions have nonzero values along only the first three modes. These initial conditions, in all cases, are scaled to make the tip displacement to be 2 cm. The three modal coordinate values are three randomly chosen, positive, independent and identically distributed numbers, subsequently rearranged so that the first mode had the largest displacement and the third mode had the smallest displacement. The initial values of the velocity degrees of freedom are taken to be zero. In applications, users who have other preferred criteria for choosing representative initial conditions can freely use them with no consequences for the rest of the algorithm.

Having selected initial conditions, we must simulate the system by integrating the equations forward in time. To that end, we use the semi-implicit integration method presented in section 2.3.

The data generation process is relatively slow, but once it is done and the reduced order model is constructed, we can use it for many subsequent quicker calculations. Beyond its academic interest, our approach is practically useful in situations where the reduced order model will be used repeatedly after it is developed.

2.4.2.1 Selecting a subset of hysteretic variables

For data generation, we numerically integrate the full system, over some time interval $[0, T]$ with N_t points in time. This process is carried out N_s times with different random representative initial conditions as described above. The integration duration T is chosen as 1 second, which gives several cycles of oscillation of the lowest mode along with some significant decay in oscillation amplitude. For each such solution with a random initial condition, upon arranging the z variables' solutions side by side in columns, a matrix of size $n_\mathrm{g}\, n_\mathrm{e} \times N_t$ is generated. This matrix is divided by its Frobenius norm, i.e., the square root of the sum of squares of all elements. We stack N_s such normalized matrices, one from each simulation, side by side to form a bigger matrix $\mathbf{Z}$ of size $n_\mathrm{g}\, n_\mathrm{e} \times N_t\, N_\mathrm{s}$. Clearly, the dimension of the row-space of $\mathbf{Z}$ is at most $n_\mathrm{g} n_\mathrm{e}$, because that is the total number of rows. Identification of a useful subset of hysteretic variables is equivalent to identifying a useful subset of the rows of $\mathbf{Z}$. Therefore the problem we face now is that of selecting rows of $\mathbf{Z}$ which contain a high level of independent information.

Selecting a finite subset of the rows of $\mathbf{Z}$ is a combinatorial optimization problem. For example, if we start with $n_\mathrm{g} n_\mathrm{e} = 900$ and want to select a subset of size, say, 100, then the total number of subsets possible is extremely large and only a modest number of them can realistically be checked. Sometimes low-rank approximations to data matrices can be obtained using the proper orthogonal decomposition (POD) [27], but that technique is not useful here because it does not select a subset of rows.

Here, for a simple practical solution, we use a greedy algorithm that is closely related to a use of the QR decomposition (rank deficient least squares solutions) discussed in [22]. Although it is not guaranteed to give the best solution, we will see that it does give a reasonably good solution.

1. Of all the rows of $\mathbf{Z}$, we first select the one with the largest 2-norm and set it aside; we also record its index (or row number), which we call j_1. We scale the j_1^{th} row to unit

norm, calculate its inner products with the rest of the rows of $\mathbf{Z}$, and subtract from them their respective components along the j_1^{th} row direction, yielding a modified $\mathbf{Z}$.

2. Next, of all the so far unselected rows of the modified $\mathbf{Z}$, we select the one with the largest 2-norm; we record its row number in the original $\mathbf{Z}$, and call it j_2. We normalize the row and subtract its component along the still-remaining rows. This yields a further modified $\mathbf{Z}$.

3. To clarify, we now have two indices selected (j_1 and j_2); and $n_{\text{g}}n_{\text{e}} - 2$ rows of $\mathbf{Z}$ remaining in contention, where for each of these remaining rows their components along the already-selected rows have been removed.

4. Proceeding as above, we select a third row (largest 2-norm among the $n_{\text{g}}n_{\text{e}} - 2$ rows). We record its row number (call it j_3), normalize the row, and remove its component from the remaining $n_{\text{g}}n_{\text{e}} - 3$ rows.

5. We proceed like this for as many rows as we wish to include in the reduced order model. A termination criterion based on the norm of the remaining part can be used if we wish.

6. In the end, we are interested only in the selected indices $j_1, j_2, \cdots, j_m$. What remains of the matrix $\mathbf{Z}$ is discarded.

7. In the above description, we could have removed the rows from $\mathbf{Z}$ after selecting them. That would leave a remaining matrix $\mathbf{Z}$ with progressively fewer rows as the calculation proceeded. That alternative algorithm is outlined below for ease of understanding.

For intuitive understanding through a simple example, we now describe the above procedure using small hypothetical numbers. The data matrix has, say, 10 rows (for simplicity). Let the 4^{th} row have the largest 2-norm. Let this row be denoted by r_4. We select the fourth row, remove it from the data matrix, and obtain a new matrix with 9 rows. We divide r_4 by its 2-norm to obtain a unit vector, say e_4. We take the inner product of e_4

with each of the 9 remaining rows, and subtract from these rows their components along e_4. The new data matrix has rows that are all orthogonal to e_4. Let the 5^{th} row of this remaining matrix have the largest 2-norm. We must remember that this index, namely 5, was actually 6 in the original 10-row data matrix. With that caveat, we are back to the second line of this paragraph, only with 9 rows instead of 10. We proceed in this way for as many rows as we wish to select, or until the 2-norms of the remaining rows become small enough. A numerical example is given in Appendix B .

2.4.2.2 Finding matrix P

With the indices chosen, a submatrix $\mathbf{Z}_\text{s}$ is assembled using the $(j_1, j_2, \ldots, j_m)^{\text{th}}$ rows ofthe original (and not the reduced) $\mathbf{Z}$. We now solve the straightforward least squares problem,

$$\mathbf{P} = \underset{\hat{\mathbf{P}} \in \mathbb{R}^{r \times m}}{\text{argmin}} \quad ||\mathbf{R}^\top \mathbf{A}\mathbf{Z} - \hat{\mathbf{P}}\mathbf{Z}_\text{s}||_\text{F}, \tag{2.16}$$

where $||\cdot||_\text{F}$ denotes the Frobenius norm. The above problem, upon taking matrix transposes, is routine in, e.g., Matlab. The final reduced order model becomes

$$\tilde{\mathbf{M}}\ddot{\boldsymbol{\xi}} + \tilde{\mathbf{K}}\boldsymbol{\xi} + \mathbf{P}\boldsymbol{z}_\text{s} = \mathbf{R}^\top \boldsymbol{f}_0(t). \tag{2.17a}$$

$$\dot{\boldsymbol{z}}_\text{s} = \left(\bar{A} - \alpha\, \text{sign}(\dot{\boldsymbol{\chi}}_\text{s} \circ \boldsymbol{z}_\text{s}) \circ |\boldsymbol{z}_\text{s}|^{\circ n_\text{h}} - \beta\, |\boldsymbol{z}_\text{s}|^{\circ n_\text{h}}\right) \circ \dot{\boldsymbol{\chi}}_\text{s}, \quad \dot{\boldsymbol{\chi}}_\text{s} = \mathbf{B}_\text{s}\, \mathbf{R}\, \dot{\boldsymbol{\xi}}, \tag{2.17b}$$

where $\mathbf{B}_\text{s}$ is a submatrix of $\mathbf{B}$ constructed by retaining the $(j_1, j_2, \ldots, j_m)^{\text{th}}$ rows of the latter.

Equations 2.17a and 2.17b are equivalent to a $2r + m$ dimensional system of first order equations (r modes and m hysteretic variables). Note that the right hand side of Eq. 2.17a may seem like it has a large number of elements, but in practice for many problems, external forcing is restricted to a few locations or can be reduced to a few effective locations (e.g., if the forces acting at several nodes maintain fixed proportions to each other). We do not investigate this aspect of size reduction because we have so far not made simplifying assumptions about $\boldsymbol{f}_0(t)$. When the forcing is zero, of course, the right hand side is zero.

We now turn to the results obtained using, first, our integration routine; and then our approach for developing reduced order models.

2.5 Results

Our main aim is accurate simulation of hysteretic dissipation, which is most easily seen in the unforced decaying response of the structure. So we will first consider some unforced transient responses of the structure to examine both stability and numerical accuracy of our semi-implicit integration algorithm. Subsequently we will present reduced order models and show their efficacy compared to the full model.

In the results from direct numerical integration using our proposed semi-implicit algorithm, we will check for three things: (i) the theoretically expected power law decay for small amplitude vibrations, (ii) the absence of instabilities arising from higher modes, and (iii) overall accuracy.

For error calculations with low dimensional systems, i.e., when the number of elements in the FE model is small, we will use Matlab's `ode15s` for comparison with both the absolute and relative error tolerances set to 10^{-10}; this is because `ode15s` has built-in adaptive step sizing and is accurate when it works. For high dimensional systems `ode15s` does not work and we will use the proposed semi-implicit algorithm itself with a very small step size $\left(h = 2^{-23}\right)$ for error estimates.

We now select some parameter values to be used in the simulation.

2.5.1 Choice of parameter values

We consider a cantilever beam with Young's modulus $E = 200$ GPa and density $\rho = 7850\,\mathrm{kg\,m^{-3}}$; of length 1 m and square cross section of $2\,\mathrm{cm} \times 2\,\mathrm{cm}$. This yields a flexural rigidity $EI = 2666.7\,\mathrm{Nm^2}$ and mass per unit length $\bar{m} = 3.14\,\mathrm{kg\,m^{-1}}$.

For many metals, 0.2% strain is near the border of elastic behavior. For the beam parameters above, if the beam is statically deflected under a single transverse tip load, then 0.2% strain at the fixed end of the beam corresponds to a tip deflection of 6 cm, which is taken as a reasonable upper bound for the vibration amplitudes to be considered in our simulations below.

Next, we consider the hysteretic damping itself. The index n_h in the Bouc-Wen model is primarily taken to be 0.5 for reasons explained a little later. A larger value is considered in subsection 2.5.4, and only in subsection 2.5.4, to clarify an issue in convergence. The parameters α and β are somewhat arbitrary; we have found that the values $\alpha = 0.8$ and $\beta = 0.5$ yield hysteresis loops of reasonable shape. It remains to choose the Bouc-Wen parameter $\bar{A}$.

It is known that for small amplitude oscillations, the Bouc-Wen dissipation follows a power law. An estimate for the upper limit of forcing amplitude in the Bouc-Wen model, below which the power law should hold, is given in [36] as

$$\chi_\mathrm{max} = \left(2 \, \frac{\bar{A}^{2-2\,n_\mathrm{h}} \, (1+n_\mathrm{h}) \, (1+2\,n_\mathrm{h}) \, (2+3\,n_\mathrm{h})}{(2\,{n_\mathrm{h}}^2\alpha^2 + 4\,n_\mathrm{h}\alpha^2 - n_\mathrm{h}\beta^2 + 2\,\alpha^2) \, (2+n_\mathrm{h})} \right)^{\frac{1}{2\,n_\mathrm{h}}} . \tag{2.18}$$

Choosing χ_max to correspond to the abovementioned 0.2% strain at the fixed end, in turn corresponding to a static free-end deflection of 6 cm for the above beam, we find from Eq. (2.18) that

$$\bar{A} = 0.065.$$

Only one physical model parameter remains to be chosen, namely γ_h. To choose this parameter value, we note that the amplitude decay in free vibrations with Bouc-Wen hysteretic dissipation is not exponential. Thus, the idea of percentage of damping is only approximately applicable. Upon looking at the reduction in amplitude after a certain number of oscillations (say M), an equivalent "percentage damping" can be approximated using the formula

$$\zeta_\mathrm{equiv} \approx \frac{1}{2\pi M} \ln \left(\frac{A_1}{A_{1+M}} \right) . \tag{2.19}$$

Metal structures often have 1-2 % damping [35]. We will choose values of the hysteretic dissipation γ_{h} (recall Eq. (2.2)) to obtain $0.01 \leq \zeta_{\mathrm{equiv}} \leq 0.02$. Numerical trial and error show that

$$\gamma_{\mathrm{h}} = 3000\,\mathrm{Nm}$$

is a suitable value (see figure 2.3). From here, to the end of this chapter, the unit of time is second.

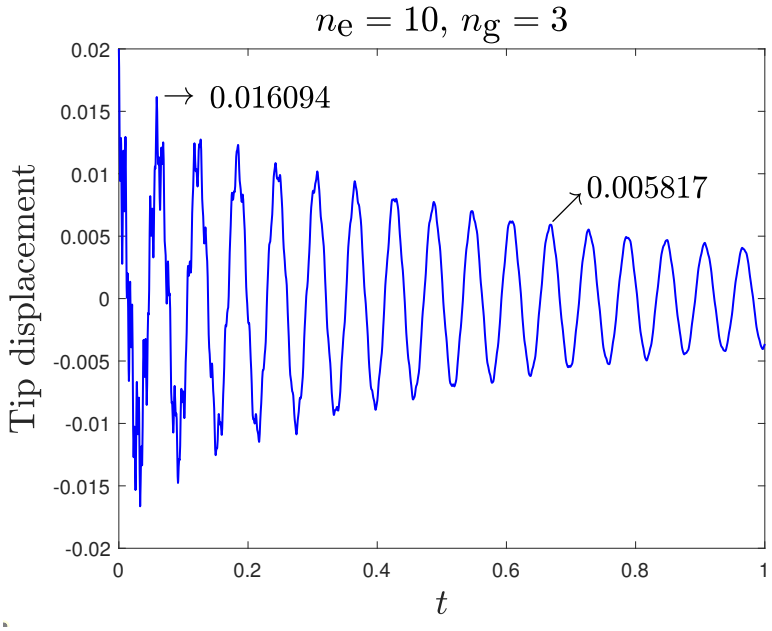

FIGURE 2.3: Tip displacement (m) for $\gamma_{\mathrm{h}} = 3000$ and $n_{\mathrm{h}} = 0.5$ shows an approximate equivalent damping of about 1.6%, as per Eq. (2.19). Here 10 beam elements were used, with 3 hysteresis Gauss points per element. Time integration was done using Matlab's `ode15s` with error tolerances set to 10^{-10}.

2.5.2 Semi-implicit integration: stability and accuracy

Before we examine the performance of our proposed semi-implicit integration method, we will verify that the FE model indeed displays power law damping at small amplitudes, as predicted by theoretical analyses of the Bouc-Wen model.

The small amplitude dissipation per cycle of the Bouc-Wen model is proportional to amplitude to the power $n_{\mathrm{h}} + 2$ [36]. Since the energy in the oscillation is proportional to

amplitude squared, we should eventually observe small amplitude oscillations in the most weakly damped mode with amplitude A obeying

$$A\dot{A} = \mathcal{O}\left(A^{n_\mathrm{h}+2}\right)$$

whence for $n_\mathrm{h} > 0$

$$A = \mathcal{O}\left(t^{-\frac{1}{n_\mathrm{h}}}\right). \tag{2.20}$$

For the Bouc-Wen model, letting $n_\mathrm{h} \to 0$ produces hysteresis loops of parallelogram-like shape, and so we prefer somewhat larger values of n_h; however, to have a significant decay rate even at small amplitudes, we prefer somewhat smaller values of n_h. As a tradeoff, we have chosen $n_\mathrm{h} = \frac{1}{2}$. We expect an eventual decay of vibration amplitudes like $1/t^2$.

For our beam model, with 10 elements and 3 Gauss points per element, and with our semi-implicit numerical integration algorithm[3], the computed tip displacement asymptotically displays the expected power law decay rate, as seen on linear axes in Fig. 2.4(a) and more clearly in the logarithmic plot of Fig. 2.4(b). The frequency of the residual oscillation is close to the first undamped natural frequency of the beam. Higher modes are not seen in the long-term power law decay regime.

Having checked the asymptotic power law decay rate, we next ensure that the semi-implicit algorithm does not produce spurious oscillations in higher modes within the computed solution. This issue is important because, with increasing mesh refinement in the FE model, very high frequencies are unavoidable. While those high frequency modes exist in principle, their response should be small if any external excitation is at low frequencies and initial conditions involve only the lower modes. To examine this aspect, we denote the time period of the highest mode present in the structural model by T_min. As the number of elements increases, T_min decreases, as indicated in Fig. 2.5(a).

We now use our semi-implicit method to simulate an FE model with 100 elements and with nonzero initial conditions along only the first 3 modes. In the computed solution,

[3]Matlab's `ode15s` struggles with such long simulations on a small desktop computer; our algorithm works quickly.

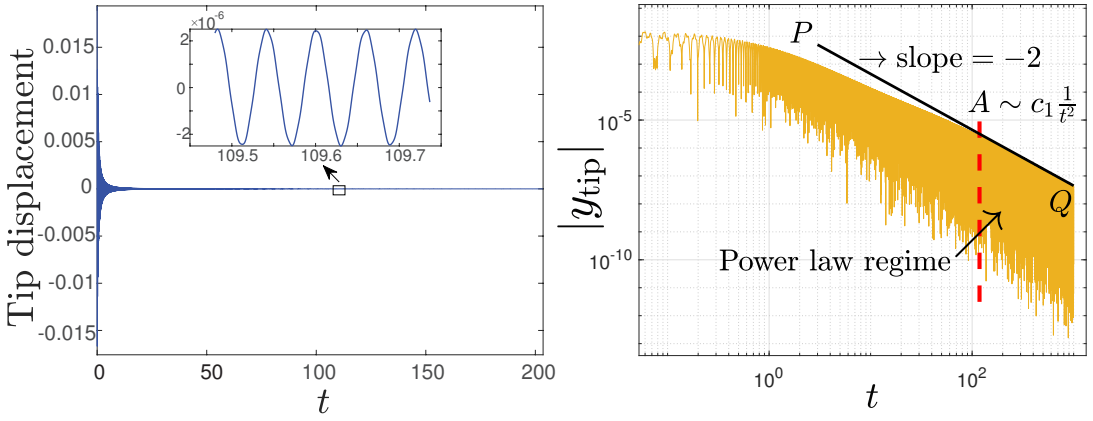

a) Small amplitude oscillations. b) Power law decay.

FIGURE 2.4: The long term oscillation in the beam tip response (m) shows very slow power law decay when $n_h = \frac{1}{2}$. A small portion of the solution is shown zoomed within the left subplot. The aim of this simulation is to show that the model and numerical integration method together retain the correct asymptotic behavior far into the small-amplitude regime.

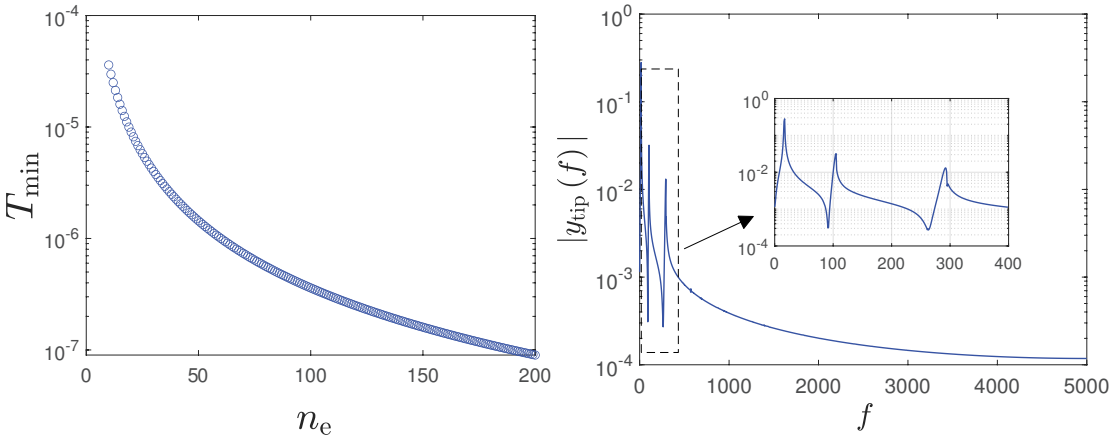

a) $T_{\min}$ vs. n_e. b) FFT of y_{tip}.

FIGURE 2.5: (a) Variation of $T_{\min}$ (second) with n_e and (b) Frequency content of the transient tip displacement response when the first three modes are disturbed in a uniform FE model with 100 elements with $n_h = 0.5$.

we expect to see frequency content corresponding to the first three modes only. Figure 2.5(b) indeed shows only three peaks. Spurious responses of the higher modes are not excited. Note that this simulation was done with a time step of $h = 10^{-4}$ s, which is more than 275 times larger than the time period of the highest mode for $n_e = 100$, which is $T_{\min} = 3.6 \times 10^{-7}$ sec (see Fig. 2.5(a)). It is the implicit part of the code that allows stable

numerical integration with such a large step size.

Having checked that spurious oscillations in very high modes are *not* excited, it remains to check that accurate results are obtained with time steps h which are sufficiently small compared to the highest mode of interest. To this end, the convergence of the solution with decreasing h is depicted in Fig. 2.6. For the beam modeled using 10 elements, the first five natural frequencies are

$$16.3,\ 102.2,\ 286.2,\ 561.3,\ \text{and } 929.3 \text{ Hz}.$$

Numerical simulation results using our semi-implicit algorithm are shown in Fig. 2.6 for $h = 10^{-3}$ s, 10^{-4} s, and 10^{-5} s. The overall solution is plotted on the left, and a small portion is shown enlarged on the right. Only 10 elements were used for this simulation to allow use of Matlab's `ode15s`, which has adaptive step sizing and allows error tolerance to be specified (here we used 10^{-10}). It is seen in the right subplot that although all three solutions from the semi-implicit method are stable, the one with $h = 10^{-3}$ s does not do very well in terms of accuracy; the one with $h = 10^{-4}$ s is reasonably close and may be useful for practical purposes; and the one with $h = 10^{-5}$ s is indistinguishable at plotting accuracy from the `ode15s` solution. The match between our semi-implicit integration with $h = 10^{-5}$ s and Matlab's `ode15s` with error tolerances set to 10^{-10} indicates that both these solutions are highly accurate.

2.5.3 Order of convergence

Using simulations with relatively few elements and over relatively short times, we can compare the results obtained from our semi-implicit method (SIM) with `ode15s`, and examine convergence as h is made smaller. Figure 2.6 shows the tip response for an FE model with 10 elements for different time step sizes and compares them with the `ode15s` solution. Here we will use two different error measures.

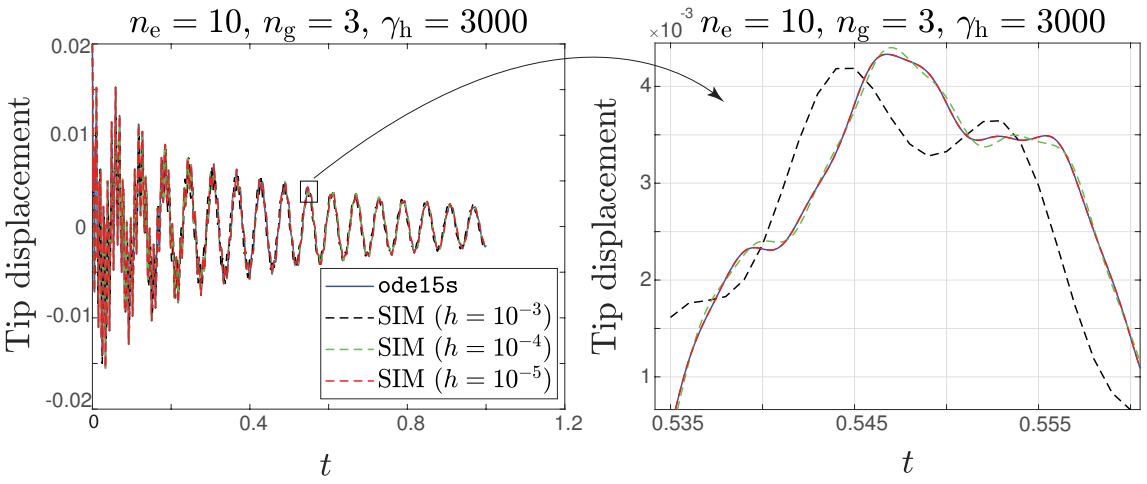

a) Tip displacement response. b) Enlarged view.

FIGURE 2.6: Tip displacement response (m) calculated using different time steps (second) (compared to `ode15s`) with $n_h = 0.5$.

2.5.3.1 RMS error

We choose a fairly large number ($N_E = 128$) of points evenly spaced in time, and for each h we calculate the response at those instants of time. The overall time interval was chosen to be [0,1]. Clearly, h can be successively halved in a sequence of simulations to ensure that the solution is always computed at exactly the N_E time instants of interest (along with other intermediate points).

We define our RMS error measure as

$$e_{\text{rms}}(h) = \sqrt{\frac{1}{N_E}\sum_{k=1}^{N_E}\left(y_h(t_k) - y_{\text{accurate}}(t_k)\right)^2}, \quad N_E = 128. \tag{2.21}$$

In the above, when the number of elements is modest (e.g., $n_e = 10$), we use the highly accurate solution obtained from `ode15s` as the "accurate" one. With larger numbers of elements, `ode15s` cannot be used for validation. Having seen the overall accuracy of the semi-implicit method (SIM) with fewer elements when compared with `ode15s`, we use the SIM solution with extremely small time steps as the "accurate" one for error estimation with larger number of elements (e.g., $n_e = 30$). Results are shown in Fig. 2.7. It is seen that for relatively smaller values of γ_h, a significant regime of approximately

quadratic convergence is obtained (Fig. (2.7(a), 2.7(c))). It means that for lightly damped structures the performance of the semi-implicit algorithm is excellent. For larger values of γ_h, however, the convergence plot is more complicated, and there is no significant regime of quadratic convergence (Fig. (2.7(b), 2.7(d))). This is because the damping model is strongly non-analytic, and strong damping makes the role of that non-analyticity stronger. However, over a significant regime and in an average sense, it appears that the convergence is superlinear (i.e., the average slope exceeds unity in a loglog plot), and so the integration algorithm still performs well. A larger value will be considered in subsection 2.5.4.

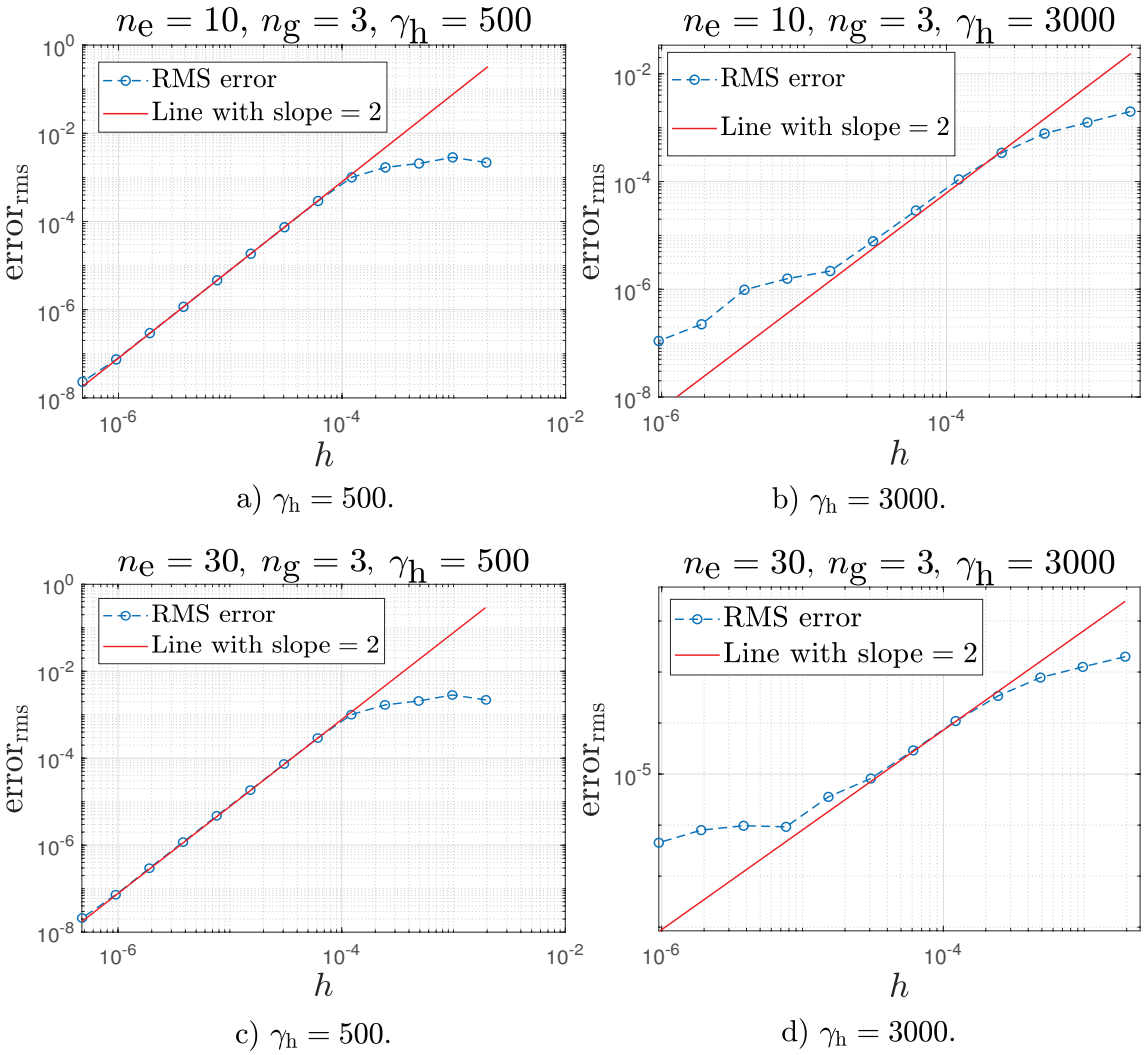

a) $\gamma_h = 500$. b) $\gamma_h = 3000$.

c) $\gamma_h = 500$. d) $\gamma_h = 3000$.

FIGURE 2.7: Time step (second) vs. RMS error (128 equispaced points in time) for $n_e = 10$ and 30 with $n_h = 0.5$.

The role of nonanalyticity in the Bouc-Wen model, and the way in which it is handled in

our semi-implicit algorithm, are worth emphasizing. See Fig. 2.8. In the figure, point A

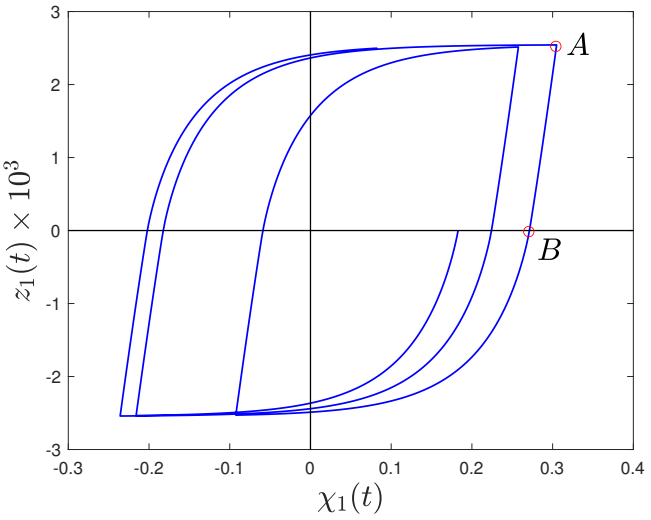

FIGURE 2.8: Hysteresis loop for the z_1 driven by χ_1 (at Gauss point "1" near the fixed end).

shows a discontinuous slope change due to the sign change of the driving term, $\dot{\chi}$. This point is handled with an *explicit* attempt to locate the instant of change in direction, with one integration step taken on each side of that instant. Point B indicates a sign change in z_1. Our proposed algorithm does not separately identify sign changes of z within one time step, in the interest of simplicity. Due to nonanalyticity at both points A and B, integration errors increase when the nonsmoothness dominates (high γ_{h} and/or small n_{h}). A larger value will be considered in subsection 2.5.4.

2.5.3.2 Error at a fixed instant of time

We now consider the absolute value of error at some fixed instant of time $t = \tau$,

$$e_\tau(h) = |y_h(\tau) - y_{\mathrm{accurate}}(\tau)|. \tag{2.22}$$

Here, we use $\tau = 1$.

Straight line fits on loglog plots of $e_\tau(h)$ versus h in Fig. (2.9(a), 2.9(b)) show average slopes that slightly exceed unity. While these slopes are not rigorously proved to exceed

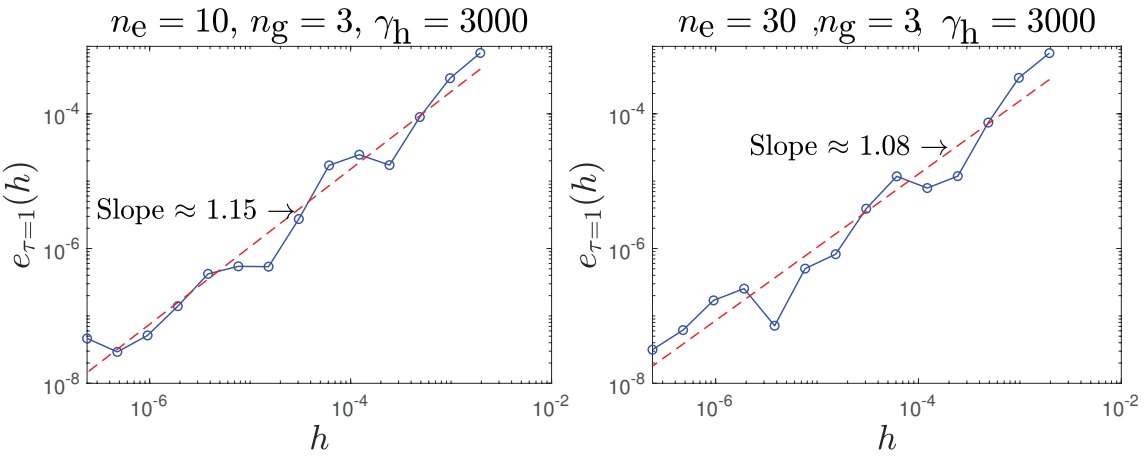

a) $n_e = 10$. b) $n_e = 30$.

FIGURE 2.9: Error at $t = 1$ sec, for FE models with 10 and 30 elements with $n_h = 0.5$.

unity, the overall convergence rate of the integration algorithm may be considered roughly linear (on average) over a sizeable range of step sizes. It is emphasized that these error computations are done in a regime where (i) Matlab's `ode15s` does not work at all, (ii) explicit methods are unstable unless extremely small time steps are used, (iii) properly implicit algorithms are both complex and not guaranteed to converge, and (iv) $n_h = 0.5$ in the Bouc-Wen model is relatively small. Considering these four difficulties, the semi-implicit method (SIM) proposed in this chapter may be said to be simple, effective, and accurate.

2.5.4 Larger n_h

Everywhere in this chapter except for this single subsection, we have used $n_h = 0.5$. In this subsection only, we consider $n_h = 1.5$. Due to the greater smoothness of the hysteresis loop near the point B of Fig. 2.8, we expect better convergence for this higher value of n_h.

Some parameter choices must be made again. Using the yield criteria used in section 2.5.1, for $n_h = 1.5$, we find we now require

$$\bar{A} = 608.9\,.$$

Subsequently, we find an approximate equivalent damping ratio $\zeta_{\text{equiv}} = 0.015$ for $\gamma_{\text{h}} = 0.3$. It is interesting to note that with the change in n_{h} and for the physical behavior regime of interest, $\bar{A}$ and γ_{h} have individually changed a lot but their product has varied only slightly (195 Nm for about 1.6% damping in the $n_{\text{h}} = 0.5$ case, and 183 Nm for about 1.5% damping in the $n_{\text{h}} = 1.5$ case).

The decay of tip response amplitude (Fig. 2.10) for these parameters (with $n_{\text{h}} = 1.5$) looks similar to the case studied in the rest of this chapter ($n_{\text{h}} = 0.5$, with attention to Fig. 2.3).

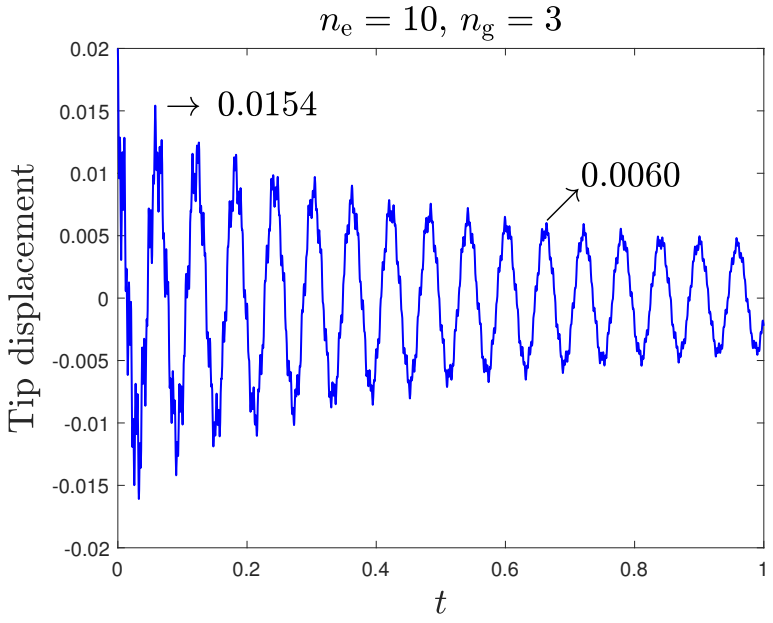

FIGURE 2.10: Tip displacement (m) for $\gamma_{\text{h}} = 0.3$ and $n_{\text{h}} = 1.5$ shows an approximate equivalent damping of about 1.5%, as per Eq. 2.19. Here 10 beam elements were used, with 3 hysteresis Gauss points per element. Time integration was done using Matlab's `ode15s` with error tolerances set to 10^{-10}.

The main point to be noted in this subsection is that with $n_{\text{h}} = 1.5$, $\bar{A} = 608.9$, $\gamma_{\text{h}} = 0.3$, and all other parameters the same as before, we do indeed observe superior convergence over a significant range of step sizes: see Fig. 2.11 for FE models with 10 and 30 elements, and compare with Fig. 2.7. For the case with 10 elements, the convergence is essentially quadratic. With 30 elements the convergence is slightly slower than quadratic, but much faster than linear. Note that these estimates are from numerics only: analytical estimates are not available.

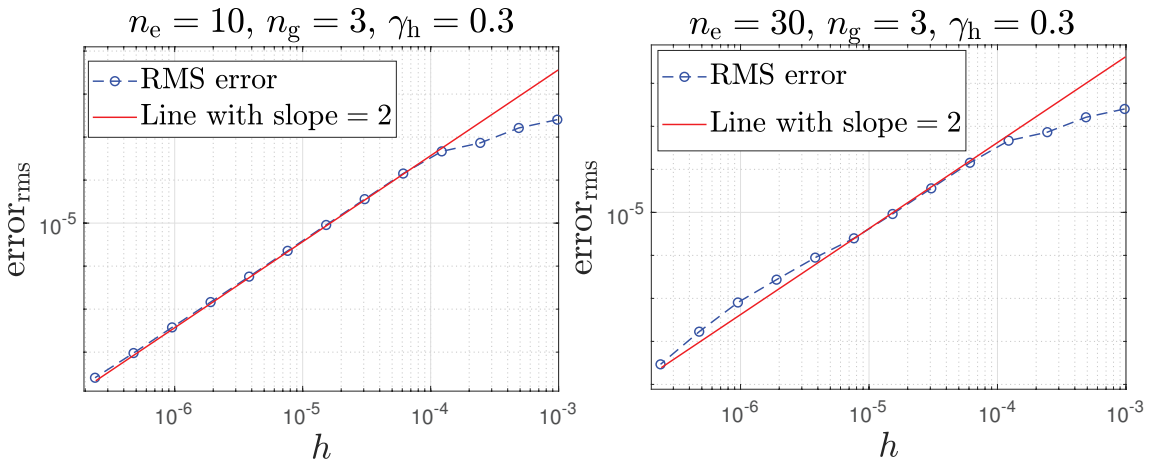

a) $n_e = 10$. b) $n_e = 30$.

FIGURE 2.11: Time step (sec) vs. RMS error (128 equispaced points in time) for $n_e = 10$ and 30 with $n_h = 1.5$. The linear fit for 10 elements has slope 2.0. The linear fit for 30 elements has slope 1.9; another line with slope 2 is shown for comparison.

As mentioned above some of the difficulty with accurate integration of hysteretically damped structures comes from the zero crossings of the hysteretic variable z itself. In this study, for simplicity, we have avoided special treatment of these zero crossings. However, the results of this subsection show that the effect of these zero crossings is milder if n_h is larger.

We now turn to using results obtained from this semi-implicit integration method to develop data-driven lower order models of the hysteretically damped structure.

2.5.5 Reduced order models

In our beam system, we have 2 degrees of freedom per node (one displacement and one rotation). Let the total number of differential equations being solved, in first order form, be called N_D. If there are n_e elements, we have $N_D = 4n_e + n_e n_g$ first order differential equations. In a reduced order model with r modes and m Gauss points, we have $N_D = 2r + m$ first order differential equations. Although the size of the problem is reduced significantly in this way, the accuracy can be acceptable.

For demonstration, we consider two FE models of a cantilever beam, with hysteresis, as follows:

(i) 100 elements with 3 Gauss points each ($N_{\mathrm{D}} = 700$).

(ii) 150 elements with 3 Gauss points each ($N_{\mathrm{D}} = 1050$).

For each of the two systems above, the datasets used for selecting the subset of hysteretic states (or Gauss points) were generated by solving the full systems 60 times each for the time interval 0 to 1 with random initial conditions and time step $h = 10^{-4}$, exciting only the first 3 modes ($r = 3$). Data from each of these 60 solutions were retained at 1000 equispaced points in time ($N_t = 1000$; recall subsection 2.4.2.1).

All reduced order model (ROM) results below are for $r = 3$ retained modes. Further, the number of hysteresis Gauss points is denoted by m. Results for $m = n_{\mathrm{e}}$ are shown in Fig. (2.12(a), 2.12(c)).

We now quantitatively assess the accuracy of the ROMs. To this end, we write $y^{(m)}_{\mathrm{tip(ROM)}}(t)$ and $y_{\mathrm{tip(FM)}}(t)$ for the ROM and full model outputs respectively. We then compute the error measure

$$\mathcal{E}_{\mathrm{rms}} = \sqrt{\frac{1}{N_{\mathrm{E}}} \sum_{k=1}^{N_{\mathrm{E}}} \left(y^{(m)}_{\mathrm{tip(ROM)}}(t_k) - y_{\mathrm{tip(FM)}}(t_k) \right)^2}, \; N_{\mathrm{E}} = 10001, \tag{2.23}$$

for different values of m and for an integration time interval $[0, 1]$ (with $h = 10^{-4}$). The variation of $\mathcal{E}_{\mathrm{rms}}$ with m, for both models, is shown in Fig. 2.13. This error measure is not normalized. If we wish to normalize it, then we should use the quantity obtained when we set $y^{(m)}_{\mathrm{tip(ROM)}}(t)$ identically to zero: that quantity is 0.006 for both models. Thus, reasonable accuracy is obtained for $m \geq 50$, and good accuracy (about 1% error) is obtained only for $m > 100$. These numbers refer to a specific case with random initial conditions; however, Fig. 2.13 is representative for other, similar, initial conditions (details omitted).

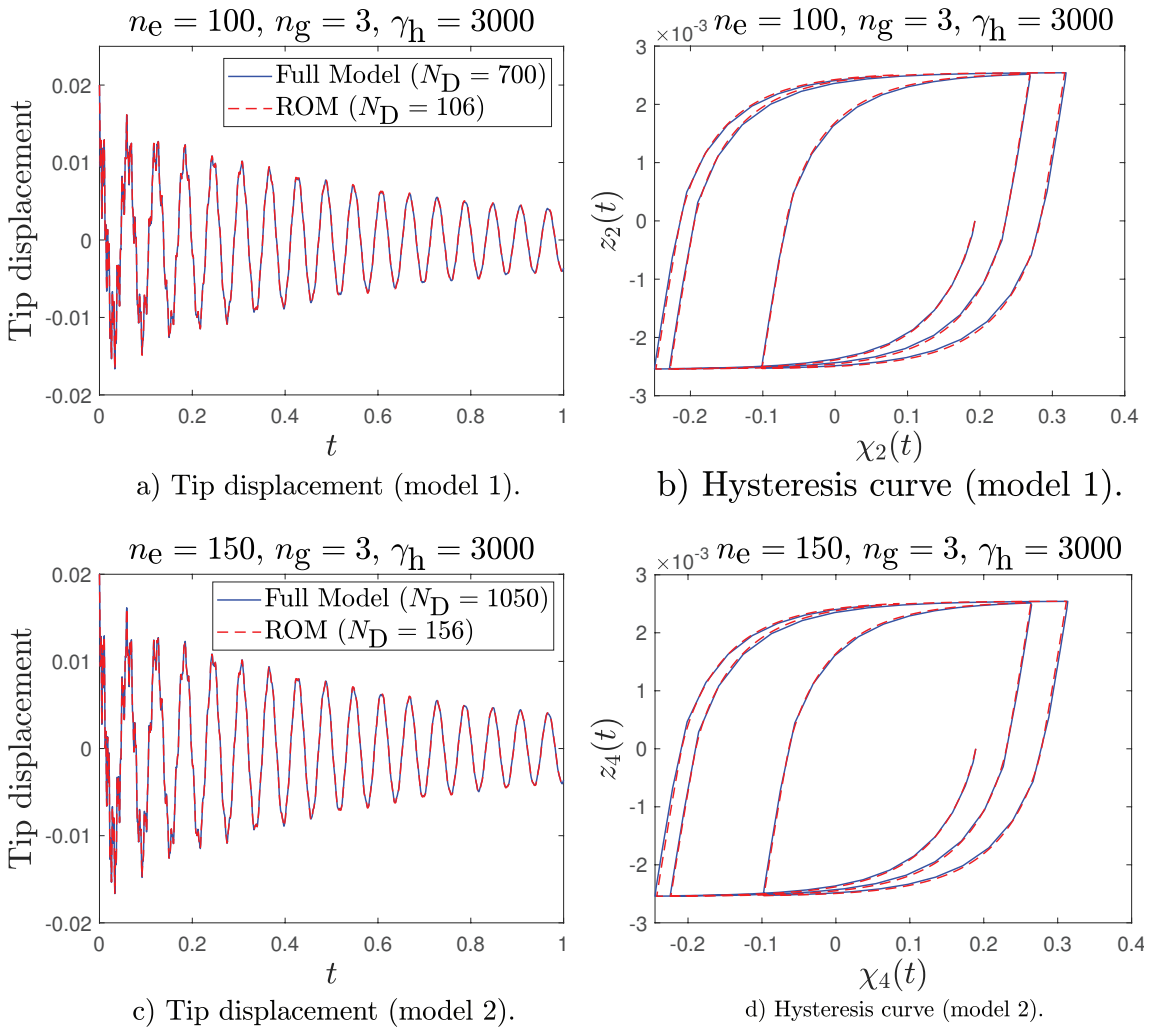

a) Tip displacement (model 1). b) Hysteresis curve (model 1).

c) Tip displacement (model 2). d) Hysteresis curve (model 2).

FIGURE 2.12: Comparison between ROM and full model, for two cases (see text for details). Tip displacements (left) and hysteresis curve (right) are shown. In subplots (b) and (d), the retained hysteresis Gauss point closest to the fixed end of the beam has been selected for display.

Finally, we report on run times needed on a modest laptop computer with the different levels of modeling described above. A representative initial conditions similar to the above was selected. The simulation duration was chosen to be 1 second, and the time step taken was 10^{-4} seconds. The following results were obtained after averaging run times for 4 runs each. (i) The full simulation with our algorithm took an average of 27.22 seconds per run. (ii) After projecting on to 3 normal modes but retaining all 450 hysteretic states, each run took an average of 1.3 seconds. (iii) Finally, with 3 normal modes and hysteretic states reduced from 450 to 150, each run took an average of 0.84 seconds. Note that we

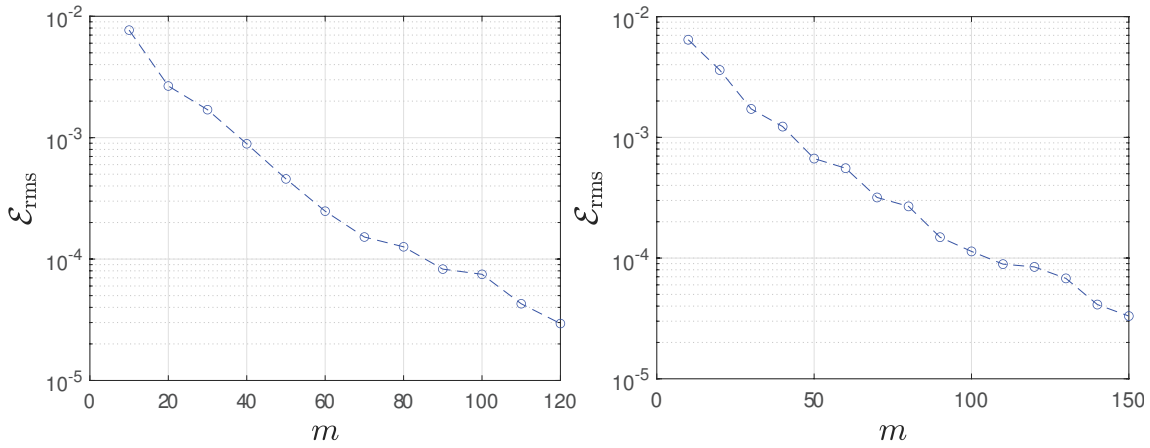

a) Model 1. b) Model 2.

FIGURE 2.13: Error convergence of ROM with increasing number of Gauss points retained. For comparison, if $y^{(m)}_{\text{tip(ROM)}}(t)$ is set identically to zero, the error measure obtained is 0.006 for both models. Thus, for reasonable accuracy, $m \geq 50$ may be needed.

could save further run time by taking larger time steps after model order reduction and/or retaining even fewer hsyteretic states.

2.6 Conclusions

Structural damping is nonlinear and, empirically, dominated by rate-independent mechanisms. Hysteresis models are therefore suitable, but present numerical difficulties when used in large finite element models. Fully implicit numerical integration of such highly refined FE models presents difficulties with convergence in addition to algorithmic complexities. With this view, we have proposed simpler but effective approaches, in two stages, to simulations of such structural dynamics. The first stage consists of a semi-implicit integration routine that is relatively simple to implement, and appears to give linear convergence or better. Moreover, the time steps required for stability can be much larger than the time period of the highest mode in the FE model. Subsequently, we have used the results from that semi-implicit integration to develop data-driven reduced order models for subsequent rapid case studies or other simulations.

Thus, our contribution is twofold: first, we present a simple and practical numerical integration method that can be easily implemented; second, we use the results from that integration algorithm to further reduce the size of the model.

Although we have worked exclusively with a cantilever beam in this chapter, our approach can be directly extended to frames that can be modeled using beam elements. We hope that future work will also examine ways in which the present approach can be extended to genuinely two- or three-dimensional structures. While we have not worked such cases out yet, we are hopeful that the issues addressed in the present study will help to tackle such higher-dimensional problems.

We now address some limitations of our work. First of all, hysteresis is scalar at a point. That is because, in a slender beam, the stress is predominantly uniaxial. In a structure with three dimensional state of stress, the development of the numerical algorithm may have to be done afresh. Secondly, some hysteresis models have larger number of internal states. There again, the algorithm will have to be extended. Third, for the reduced order model, the dataset has to be generated in advance. Perhaps future work will find a completely different algorithm where this initial data generating step will not be required.

Now, we move on to the second contribution of this thesis. In the next chapter we discuss the short-time dynamics of a linear beam subjected to an impulsive moment.

Chapter 3

Short Time Angular Impulse Response of Rayleigh Beams

3.1 Introduction

Beams are ubiquitous structural members in engineering, especially civil and mechanical engineering, and also encountered in applied physics, micro- and nano-mechanics. The mathematical study of these flexural members dates back to the 16th century [37] in the works of Jacob Bernoulli, followed by Euler. The basic assumptions with regard to the deformation kinematics, warp-free planes, planes perpendicular to the neutral axis, etc., come from the works of Euler and Bernoulli. The Euler-Bernoulli beam model is taught and studied widely owing to its simplicity and applicability for beams where either the length or the wavelength (in case of traveling waves) is large compared to the radius of gyration of the beam cross section. Many engineering beam structures obey this theory for many types of loading. One drawback of the Euler-Bernoulli beam is that the phase speed $c_p \propto \sqrt{\omega}$ is unbounded for large ω, where ω is the frequency of the wave [38]. A slightly more advanced beam model was proposed by Lord Rayleigh [39], who added rotary inertia of cross sections to the Euler-Bernoulli beam model without adding new field variables. Unlike the Timoshenko beam which adds shear deformations [40, 41], the Rayleigh beam

model is almost as easily tractable as the Euler-Bernoulli beam and has only one field variable, namely the transverse displacement $u(x,t)$. For the Rayleigh beam model, c_p approaches a finite limit as $\omega \to \infty$ [38].

In this chapter we take up the Rayleigh beam model because it is the simplest classical beam model that predicts *bounded* responses to an instantaneous *angular* impulse, i.e., an impulsive moment concentrated in both space and time. As we will show below, the response has several aspects of fundamental academic interest. Our results have practical value as well, because the impulse response function (IRF) forms the basis for evaluating the response to any arbitrary excitation using a convolution integral [42].

A basic element of the analytical treatment for such problems lies in assuming that boundaries are far enough away so that reflections of sufficient strength do not arrive too quickly, and an analysis of the short term response can be carried out by assuming either an unbounded structure or a finite structure with analytically convenient boundary conditions. A study of the response of an Euler-Bernoulli beam to a *linear* impulse gives interesting bounded results [43]. However, the Euler-Bernoulli beam model predicts unbounded responses to *angular* impulses. This is the motivation for taking up the Rayleigh beam for study in this chapter: it is the simplest model that incorporates rotary inertia and gives physically plausible results.

While our study is theoretical and limited to an ideal concentrated impulsive moment on an ideal Rayleigh beam, it will shed useful light on some practical situations as well. For example, the response of the beam to a localized angular impulse may be useful in computing the short time structural behavior upon the rapid stopping of a motor mounted on a beam with long span.

As indicated above, the transient response of beams excited by *linear* impulses (as opposed to angular impulses) is a well researched topic. A representative review of the literature follows. An early and clever article by Zener [44] studied the response of a thin plate subjected to a linear impulse for durations short enough that the effect of waves reflected from the boundaries can be neglected. Schwieger [45, 46] adapted Zener's analysis to

an Euler-Bernoulli beam, found the now well known $\sqrt{t}$ behavior in the linear impulse response, and conducted an experimental investigation that bore out the approximation. The detailed responses of an infinite beam as well as a simply supported beam were studied by Chatterjee [43] (2004), and some time later a large part of that work was developed independently by Meijaard [47] (2007). The $\sqrt{t}$ nature of the response of the infinite beam was used in computing detailed ball-impact responses in [48]. A symbolic calculation for plates subjected to impulses was presented by Claeyssen et al. [49] (2002). Numerous finite element (FE) studies of beam responses are available. Roy et al. [50] (1995) used an FE model of a beam and investigated the short time response under viscous damping with the impact at different locations along the beam. Impulse response studies have been carried out for more complicated structural members, accounting for viscoelastic layers [51] and composites [52]. There are also papers on related topics like vibro-impacting beams [53] and vibration-dominated impacts [54]. Finally, digressing from transversely acting linear impulse loading, Kenny et al. [55] (2000) studied the dynamic buckling of slender beams subjected to axial impulse loading and validated the results using FE analysis.

As the foregoing literature review indicates, there are many studies that examine the behavior of beams subjected to *linear* impulses, but not *angular* impulses. In this chapter we will study the transient behaviour of a beam subjected to an impulsive moment. We will have to abandon the Euler-Bernoulli beam model because its lack of rotary inertia leads to unbounded rotations; and we will take up instead the Rayleigh beam model, which has the same kinematics and strain energy, but in which the kinetic energy includes a contribution from the rotations of cross sections.

3.2 Euler-Bernoulli beams under impulsive moments

With reference to Fig. 3.1, consider a simply supported Euler-Bernoulli beam of length L, flexural rigidity EI, material density ρ, and cross sectional area A. Let this beam be subjected to an impulsive moment M_0 at its midpoint. The governing equation for the

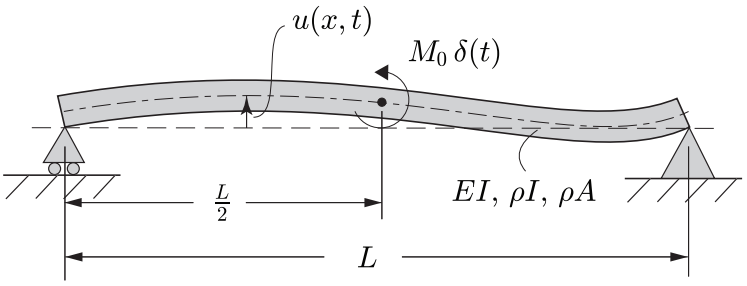

FIGURE 3.1: A slender beam subjected to a impulsive moment applied at the midpoint.

transverse displacement u is

$$\rho A\, u_{,tt} + EI\, u_{,xxxx} = -M_0\, \delta_{,x}\left(x - \frac{L}{2}\right)\delta(t), \tag{3.1}$$

where x is the spatial coordinate along the beam, t is time, subscripts denote partial derivatives, and $\delta(\cdot)$ denotes the Dirac delta function[1].

Let us approach this problem using dimensional analysis [56]. The angular *rotation* at the impulse location, namely $u_{,x}\left(\frac{L}{2}, t\right)$, is a function of five quantities, namely EI, ρA, M_0, L, and t. If we are interested in the short time response of the beam, we may tentatively assume that the beam length does not affect the solution because reflections of sufficient magnitude have not yet traveled back from the ends of the beam. By this assumption, the rotation must be a dimensionless function of EI, ρA, M_0, and t. These four quantities (three parameters and one variable) allow formation of a dimensionless variable, which we take to be

$$\pi_1 = (EI)^a\,(\rho A)^b\, t^c\, M_0^d. \tag{3.2}$$

However, since the system is linear, and starts from zero initial conditions, the response must be proportional to M_0, which means $d = 1$. Using routine calculations, the remaining constants must be

$$a = -\frac{3}{4},\ b = -\frac{1}{4},\ \text{and}\ \ c = -\frac{1}{2}. \tag{3.3}$$

In the above, $c = -1/2$ implies that the short time response is proportional to $1/\sqrt{t}$, which is unbounded as $t \to 0$. Mathematically, this unbounded response is due to non-inclusion

[1]The term $\delta_{,x}(\cdot)$ has dimension L^{-1}. The quantity M_0 is a Moment applied per unit length. So, its dimension is MLT^{-2}. Hence the dimension of RHS of Eq. 3.1 is MT^{-2}.

of rotary inertia in the Euler-Bernoulli beam model. Furthermore, for a finite-length beam, the assumption that reflections from the boundary are negligible is seen to be invalid. See Fig. 3.2. In FE simulations of a beam with unit length with large numbers of elements (we used 640 and 1280) and an implicit integration algorithm which damps out super-high frequencies, the computational result shows a short period of $1/\sqrt{t}$ behavior before high frequency oscillations appear. However, with the number of elements held fixed (at 640, which is high enough), if the time step is reduced, the duration of the $1/\sqrt{t}$ behavior shrinks as well. In the exact solution for a finite-length Euler-Bernoulli beam, reflections from the boundaries play a significant role immediately after application of the angular impulse.

With the above motivation we turn to the Rayleigh beam model, which incorporates rotary inertia but retains the simple deformation kinematics of the Euler-Bernoulli beam model [39, 57]. From an analytical perspective, the Rayleigh beam model is the preferred first step as compared to the Timoshenko beam model, which both includes rotary inertia and allows shear deformation. We hope that an analysis of the Timoshenko beam model may be undertaken in future work. In this chapter, we focus on developing asymptotic approximations for the short time angular impulse response of Rayleigh beams.

3.3 Rayleigh beams

We now consider the same elastic beam as in Fig. 3.1, but include rotary inertia equal to ρI per unit length in the mathematical model. In this formulation, for an angular impulse M_0 applied at the midpoint of the beam, the beam deflection $u(x,t)$ is governed by the equation

$$\rho A\, u_{,tt} + EI\, u_{,xxxx} - \rho I\, u_{,ttxx} = -M_0\, \delta_{,x}\left(x - \frac{L}{2}\right)\delta(t), \tag{3.4}$$

where subscripts denote partial derivatives. It is interesting to note that an Euler-Bernoulli beam incorporating nonlocal[2] effects based on Eringen's stress gradient theory [59, 58]

[2]In constitutive relations where the gradient of stress or strain is involved, the corresponding terms introduce a new length scale in the material model, and such models are called nonlocal.

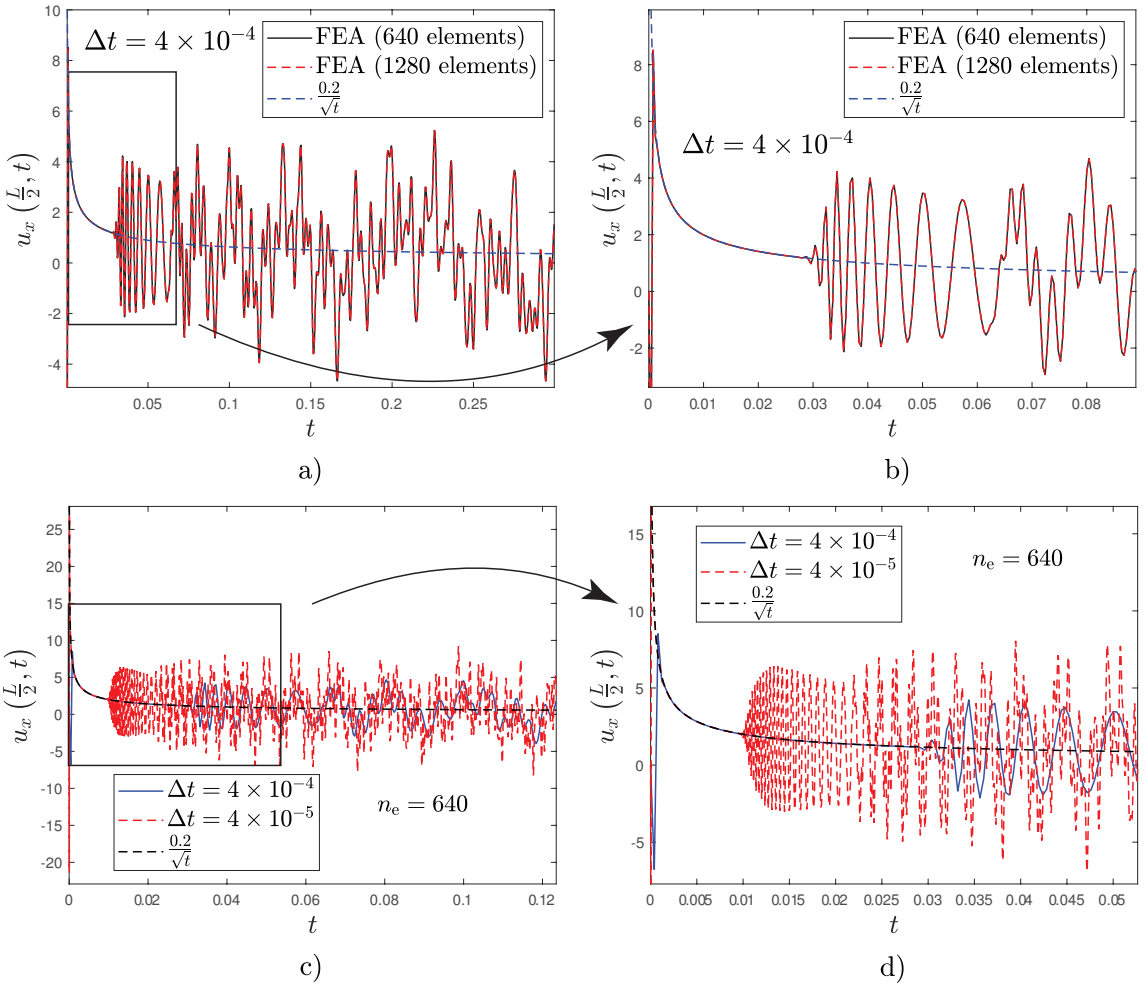

FIGURE 3.2: Computed response of a simply supported Euler-Bernoulli beam with $L = 1$, $EI = 1$, and $\rho A = 1$, to a central angular impulse for different mesh refinements and time steps. The 0.2 coefficient in the $1/\sqrt{t}$ response is numerically fitted. Between subplots (a) and (b), only the time scale is changed for visibility; so also for subplots (c) and (d). Subplots (a) and (b) show that, for a fixed time step, higher mesh refinement has no effect. Subplots (c) and (d) show that, for high enough mesh refinement, the duration of the computationally obtained $1/\sqrt{t}$ behavior shrinks as the time step is reduced. This $1/\sqrt{t}$ behavior is an artifact of implicit integration, which offers stability but damps out super-high modes, in turn removing super-quick reflections from boundaries.

assumes a similar governing equation as that of the Rayleigh beam model. However, the rotary inertia ρI per unit length of the Rayleigh beam model is replaced by the nonlocal scaling parameter $\rho A(e_0 a_c)^2$ in a nonlocal beam, e_0 is the nonlocal material parameter and a_c is the internal characteristic length.

3.3.1 Dimensional analysis

Proceeding along similar lines as in the previous section, and again dropping L because we are interested in the *short time* response, we recognize that the angular response is a function of M_0, EI, ρA, ρI, and t. There are now two dimensionless quantities, and we include M_0 in one of them and t in the other, to write

$$\eta_1 = (EI)^{a_1}\ (\rho I)^{b_1}\,(\rho A)^{c_1}\,(M_0)^{d_1} \text{ and } \eta_2 = (EI)^{a_2}\ (\rho I)^{b_2}\,(\rho A)^{c_2}\,(t)^{d_2}. \tag{3.5}$$

Setting $d_1 = d_2 = 1$ for definiteness, using routine methods, we obtain

$$a_1 = b_1 = -\frac{1}{2},\ c_1 = 0,\ \text{and } a_2 = c_2 = \frac{1}{2}, b_2 = -1, \tag{3.6}$$

or

$$\eta_1 = \frac{M_0}{I\sqrt{E\rho}},\ \eta_2 = t\sqrt{\frac{EA}{\rho I}}. \tag{3.7}$$

Accordingly, the *short-time* rotational response at the midpoint of the beam, being dimensionless, is of the form

$$u_{,x}\left(\frac{L}{2}, t\right) = f\left(\frac{M_0}{I\sqrt{E\rho}}, t\sqrt{\frac{EA}{\rho I}}\right). \tag{3.8}$$

Linearity of Eq. 3.4 implies the response is proportional to M_0, so we must have

$$u_{,x}\left(\frac{L}{2}, t\right) = \frac{M_0}{I\sqrt{E\rho}}\, f_0\left(t\sqrt{\frac{EA}{\rho I}}\right), \tag{3.9}$$

where f_0 is to be determined as a function of nondimensional time $\tau = t\sqrt{EA/\rho I}$. Since we have neglected reflections from the ends by dropping L from this dimensional analysis, Eq. 3.9 is expected to hold for $0 < \tau \ll 1$, and L large.

Next, we consider the exact solution using a modal expansion.

3.3.2 Modal solution

It may be verified that the differential operator of the Rayleigh beam is self-adjoint [57, 42] and the eigenfunctions of the resulting eigenvalue problem are orthonormal. By direct substitution, for a simply supported Rayleigh beam, the eigenfunctions are seen to be pure sines. Again assuming simple supports at both ends of the beam, and expanding the solution using the beam's eigenfunctions [57], we write

$$u(x,\tau) = \sum_{n=1}^{\infty} q_n(\tau) \sin\left(\frac{n\pi x}{L}\right), \tag{3.10}$$

where the time-varying coefficients $q_n(\tau)$ satisfy $q_n(0) = 0$.

With suitable choice of units of mass, length, and time, we can make $\rho A = 1$, $\rho I = 1$, and $EI = 1$. Now L can be treated as dimensionless. Substituting Eq. 3.10 in Eq. 3.4 yields

$$\sum_{n=1}^{\infty} \sin(p_n x)\left(q_n''(1+p_n^2) + p_n^4\, q_n\right) = -\delta_{,x}\left(x - \frac{L}{2}\right)\delta(\tau), \tag{3.11}$$

where $p_n = n\,\pi/L$, and the prime $(\cdot)'$ indicates a τ-derivative. Multiplying both sides with $\sin(p_k x)$ for positive integers k, and integrating over the length of the beam as usual, we obtain

$$q_k'' + \omega_k^2\, q_k = \frac{2\,p_k\,\cos\left(\frac{p_k\,L}{2}\right)}{L\,\left(1+p_k^2\right)}\delta(\tau), \tag{3.12}$$

where $\omega_k = p_k^2/\sqrt{1+p_k^2}$. For zero initial conditions, the solution of Eq. 3.12 is

$$q_k(\tau) = \frac{2\,p_k\,\cos\left(\frac{k\,\pi}{2}\right)}{L\,(1+p_k^2)\,\omega_k}\sin(\omega_k\,\tau), \tag{3.13}$$

yielding

$$u(x,\tau) = \frac{2}{L}\sum_{k=1}^{\infty} \frac{\cos\left(\frac{k\,\pi}{2}\right)}{p_k\,\sqrt{1+p_k^2}}\sin(p_k x)\sin\left(\frac{p_k^2}{\sqrt{1+p_k^2}}\,\tau\right). \tag{3.14}$$

Terms containing odd k drop out of the above sum, and the rotation at $x = L/2$ is then

$$u_{,x}\left(\frac{L}{2},\tau\right) = \frac{2}{L}\sum_{k=1}^{\infty}\frac{1}{\sqrt{1+4\,k^2\,a^2}}\,\sin\left(\frac{4\,k^2\,a^2}{\sqrt{1+4\,k^2\,a^2}}\,\tau\right), \tag{3.15}$$

where $a = \pi/L$. Taking a τ-derivative term by term, the angular velocity at $x = L/2$ is formally

$$u_{,x\tau}\left(\frac{L}{2},\tau\right) = \frac{2}{L}\sum_{k=1}^{\infty}\frac{4\,k^2\,a^2}{1+4\,k^2\,a^2}\,\cos\left(\frac{4\,k^2\,a^2}{\sqrt{1+4\,k^2\,a^2}}\,\tau\right), \tag{3.16}$$

but the series in Eq. 3.16 diverges at $\tau = 0$ [3]. We need more careful analysis.

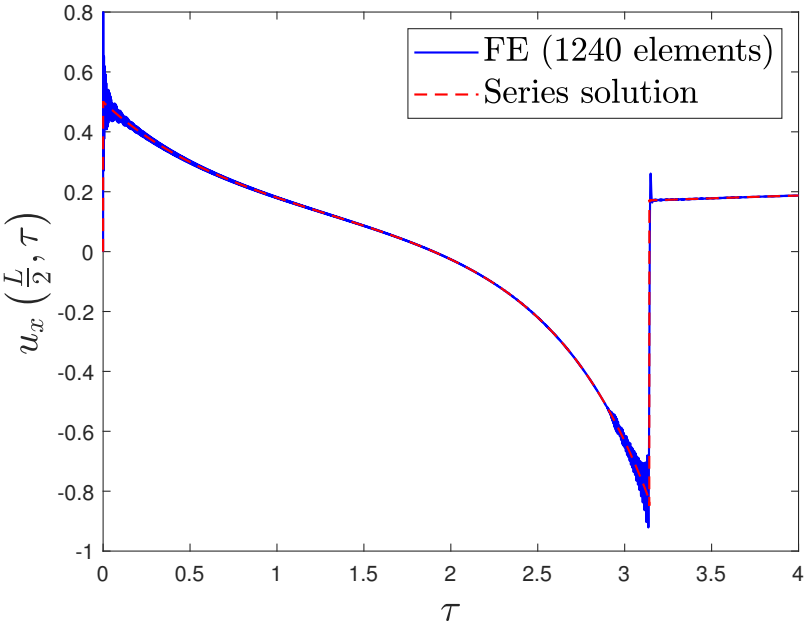

FIGURE 3.3: Angular impulse response at the midpoint of a Rayleigh beam of length $L = \pi$ calculated with a step size $h = 4\times10^{-4}$, from an FE model with 1280 elements and the series given in Eq. 3.15 summed to 10^5 terms. The series solution shows discontinuities at $\tau = 0$ and $\tau = \pi$. The discontinuity at $\tau = \pi$ is because of the arrival of high frequency reflections from the ends of the beam. The high frequency oscillations in the FE solution are numerical artifacts (see the main text).

The series solution in Eq. 3.15 for the slope at the center of the beam of length π exhibits a discontinuity at $\tau = 0$ (shown in Fig. 3.3), but the behavior is bounded unlike that of the Euler-Bernoulli beam. The discontinuity arrives some time later at points slightly separated from the point of application of the moment impulse. Further, the response is

[3] At $\tau = 0$, Eq. 3.16 yields the series $\frac{2}{L}\sum_{k=1}^{\infty}\frac{4\,k^2\,a^2}{1+4\,k^2\,a^2} = \frac{2}{L}\sum_{k=1}^{\infty}\left(1-\frac{1}{1+4\,k^2\,a^2}\right)$, which diverges.

discontinuous at $\tau = \pi$ as well. This is because of two reasons. First, for a beam length π, the travel distance from the center of the beam to either end and back is π. Second, with physical parameters set to unity as above, the phase velocity as a function of frequency ω approaches unity from below as $\omega \to \infty$. For this reason, infinitely many frequencies return after reflection as $\tau \to \pi$. We evaluate the series solution by summing 10^5 terms, and demonstrate the first two discontinuities. The series for longer times shows subsequent discontinuities at integer multiples of π (not displayed for brevity).

Finite element (FE) analysis of a Rayleigh beam with 1280 fixed-length elements (see details in **Appendix** C) yields results that match the series solution including the discontinuity at $\tau = \pi$, except for some high-frequency oscillations near the discontinuities. We believe the oscillations are artifacts of the level of mesh refinement, the chosen time step, and the implicit integration algorithm used. The analytical series solution is correct in principle, but should be verified by an independent calculation: the FE solution, which matches over a large region, provides that verification.

Equation 3.4 is a linear PDE which has been solved using a series expansion. In Fig. 3.3, the response of a beam of length π has been plotted to show the arrival of reflected waves from the boundary. However, in order to get physically more meaningful results, we should consider $L \gg 1$. This is because both ρA and ρI have been set to unity above, and so the lateral dimensions of the beam are of $\mathcal{O}(1)$. Hence, we must choose L large compared to unity so that the assumptions of a slender beam are valid.

For beams with $L \gg 1$, the short time impulse response is independent of the point of application of the load. Let us denote the rotational response at a point x at time τ due to an angular impulse applied at point x_0 by $v(x, x_0, \tau)$. Figure 3.4 shows the responses of a beam of length $L = 12$ subjected to an angular impulse at $x = L/2$ and at $x = L/4$.

Figure 3.4 establishes that the short time response is independent of the point of application of the load provided the beam is somewhat long and the load is not applied too close to one of the ends. For subsequent calculations, we choose the midpoint of the beam for analytical convenience because then half the terms drop out of the series solution

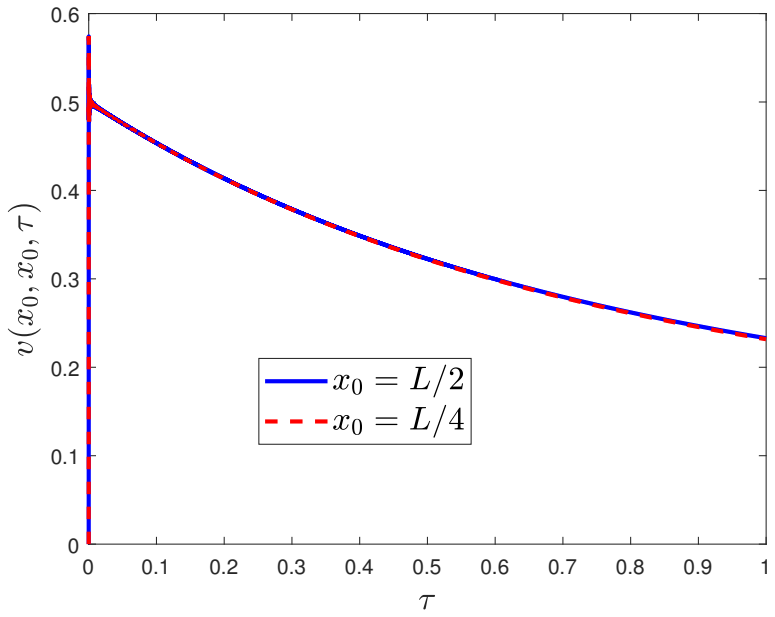

FIGURE 3.4: Responses $v(x_0, x_0, \tau)$ of a Rayleigh beam with $L = 12$ for $x_0 = L/2$ and $x_0 = L/4$. The two responses are clearly the same.

(Eq. 3.15). The series solution of Eq. 3.15 must now be treated analytically to obtain an asymptotic description of its behaviour for small τ.

We now come to the main academic research contribution of this chapter. We will show below that

$$\sum_{k=1}^{\infty} \frac{1}{\sqrt{1+4\,k^2\,a^2}} \sin\left(\frac{4\,k^2\,a^2}{\sqrt{1+4\,k^2\,a^2}}\tau\right) = \frac{\pi}{4\,a} - \frac{\pi\coth\left(\frac{\pi}{2\,a}\right)}{4\,a}\,\tau + \frac{3\pi}{16\,a}\,\tau^2 + \frac{\pi\left(\pi - 5\,a\sinh\left(\frac{\pi}{a}\right)\right)}{48\,a^2\left(\cosh\left(\frac{\pi}{a}\right)-1\right)}\,\tau^3 + \mathcal{O}\left(\tau^4\right), \quad a = \frac{\pi}{L}, \text{ and } 0 < \tau \ll 1. \tag{3.17}$$

3.4 Short time asymptotic solution

We begin with the infinite sum in Eq. 3.15,

$$S(\tau) = \sum_{k=1}^{\infty} \frac{1}{\sqrt{1+4\,k^2\,a^2}} \sin\left(\frac{4\,k^2\,a^2}{\sqrt{1+4\,k^2\,a^2}}\,\tau\right) \text{ for } 0 < \tau \ll 1. \tag{3.18}$$

It is an anharmonic[4] series, and if differentiated term by term it diverges. Let us consider a large number $N \approx 1/\sqrt{\tau}$, and split $S(\tau)$ as follows

$$S(\tau) = \sum_{k=1}^{N} f(k,\tau) + \sum_{k=N+1}^{\infty} f(k,\tau), \quad \text{where } f(k,\tau) = \frac{1}{\sqrt{1+4\,k^2\,a^2}} \sin\left(\frac{4\,k^2\,a^2}{\sqrt{1+4\,k^2\,a^2}}\,\tau\right). \tag{3.19}$$

We now state a basic result which we will use in our approximations. A formal proof is given in **Appendix** D.

Lemma 1 *Consider a function $g(y) : \mathbb{R} \to \mathbb{R}$. Let all its derivatives tend to 0 as $y \to \infty$, with higher derivatives being asymptotically smaller than lower derivatives as $y \to \infty$; and assume further that the sum $\sum_{k=N+1}^{\infty} g(k)$ and the integral $\int_N^{\infty} g(y)\,\mathrm{d}y$ exist. Then*

$$\sum_{k=N+1}^{\infty} g(k) = \int_N^{\infty} g(y)\,\mathrm{d}y - \frac{g(N)}{2} - \frac{g'(N)}{12} + \frac{g'''(N)}{720} - \frac{g^{(5)}(N)}{30240} + \frac{g^{(7)}(N)}{1209600} \cdots . \tag{3.20}$$

This result will be used repeatedly below. The known sums of some infinite series are given in **Appendix** E, which will be used below as well.

We now treat the two terms in the RHS of Eq. 3.19 separately.

3.4.1 First term of Eq. 3.19

Considering the first sum on the right hand side of Eq. 3.19, the argument of the 'sin' function, namely $\frac{4\,k^2\,a^2}{\sqrt{1+4\,k^2\,a^2}}\,\tau$, is small for all $k < N$ for $\tau \ll 1$. Thus, termwise Taylor series expansion is allowed, and it yields

$$S_1(\tau) = \sum_{k=1}^{N} f(k,\tau) = \sum_{k=1}^{N} \frac{4\,k^2\,a^2\,\tau}{4\,k^2\,a^2+1} - \sum_{k=1}^{N} \frac{32\,k^6\,a^6\,\tau^3}{3\,\left(4\,k^2\,a^2+1\right)^2} + \sum_{k=1}^{N} \frac{128\,k^{10}\,a^{10}\,\tau^5}{15\,\left(4\,k^2\,a^2+1\right)^3} + \text{h.o.t.} \tag{3.21}$$

[4] In this context: a series of sinusoidal functions where the frequencies are not integer multiples of a fundamental frequency.

The first term on the right hand side of Eq. 3.21 can be written as

$$S_{1,1} = \sum_{k=1}^{N} \frac{4\,k^2\,a^2\,\tau}{4\,k^2\,a^2+1} = N\tau - \tau \sum_{k=1}^{N} \frac{1}{4\,k^2\,a^2+1} = N\tau - \tau \sum_{k=1}^{\infty} \frac{1}{4\,k^2\,a^2+1} + \tau \sum_{k=N+1}^{\infty} \frac{1}{4\,k^2\,a^2+1}, \quad (3.22)$$

and therefore (see **Appendix** E)

$$S_{1,1} = N\tau + \tau \sum_{k=N+1}^{\infty} \frac{1}{4\,k^2\,a^2+1} - \left(\frac{\pi \coth\left(\frac{\pi}{2\,a}\right)}{4\,a} - \frac{1}{2} \right) \tau. \quad (3.23)$$

By Lemma 1, we can write

$$\begin{aligned} \sum_{k=N+1}^{\infty} \frac{1}{1+4\,k^2\,a^2} &\sim \int_N^{\infty} \frac{\mathrm{d}x}{1+4\,x^2\,a^2} - \frac{1}{8\,N^2a^2+2} + \frac{2\,Na^2}{3\,\left(4\,N^2a^2+1\right)^2} \\ &\quad - \frac{64\,N^3a^6}{15\,\left(4\,N^2a^2+1\right)^4} + \frac{8\,Na^4}{15\,\left(4\,N^2a^2+1\right)^3} + \cdots \\ &= \frac{\pi - 2\,\tan^{-1}(2Na)}{4\,a} - \frac{1}{8\,N^2a^2+2} + \frac{2\,Na^2}{3\,\left(4\,N^2a^2+1\right)^2} + \\ &\quad - \frac{64\,N^3a^6}{15\,\left(4\,N^2a^2+1\right)^4} + \frac{8\,Na^4}{15\,\left(4\,N^2a^2+1\right)^3} + \cdots . \end{aligned} \quad (3.24)$$

Substituting $N = 1/\sqrt{\tau}$ and expanding in a series for small τ,

$$\begin{aligned} \sum_{k=N+1}^{\infty} \frac{1}{1+4\,k^2\,a^2} &\approx \frac{1}{4\,a^2}\sqrt{\tau} - \frac{\tau}{8\,a^2} + \left(-\frac{1}{48\,a^4} + \frac{1}{24\,a^2} \right) \tau^{\frac{3}{2}} \\ &\quad + \frac{\tau^2}{32\,a^4} + \left(\frac{1}{320\,a^6} - \frac{1}{48\,a^4} - \frac{1}{120\,a^2} \right) \tau^{\frac{5}{2}} - \frac{\tau^3}{128\,a^6} + O\left(\tau^{\frac{7}{2}}\right). \end{aligned} \quad (3.25)$$

Substituting Eq. 3.25 in Eq. 3.23, we obtain

$$\begin{aligned} S_{1,1} = \sum_{k=1}^{N} \frac{4\,k^2\,a^2\,\tau}{4\,k^2\,a^2+1} &\approx \sqrt{\tau} + \left(-\frac{\pi \coth\left(\frac{\pi}{2\,a}\right)}{4\,a} + \frac{1}{2} \right) \tau + \frac{\tau^{\frac{3}{2}}}{4\,a^2} \\ &\quad - \frac{\tau^2}{8\,a^2} + \left(-\frac{1}{48\,a^4} + \frac{1}{24\,a^2} \right) \tau^{\frac{5}{2}} + \frac{\tau^3}{32\,a^4} + O\left(\tau^{\frac{7}{2}}\right). \end{aligned} \quad (3.26)$$

Next, the second term on the right hand side of Eq. 3.21, using partial fractions, takes the form

$$S_{1,2} = -\sum_{k=1}^{N} \frac{32\,k^6\,a^6\,\tau^3}{3\,(4\,k^2\,a^2+1)^2} = \tau^3 \sum_{k=1}^{N} \left(-\frac{2k^2\,a^2}{3} + \frac{1}{3} - \frac{1}{(8\,k^2\,a^2+2)} + \frac{1}{6\,(4\,k^2\,a^2+1)^2} \right), \tag{3.27}$$

which yields,

$$S_{1,2} = \tau^3 \left\{ \frac{2\,N}{9} \left(\frac{3}{2} - \left(N^2 + \frac{3\,N}{2} + \frac{1}{2} \right) a^2 \right) + \sum_{k=1}^{\infty} \left(-\frac{1}{(8\,k^2\,a^2+2)} + \frac{1}{6\,(4\,k^2\,a^2+1)^2} \right) \right\} - \tau^3 \sum_{k=N+1}^{\infty} \left(-\frac{1}{(8\,k^2\,a^2+2)} + \frac{1}{6\,(4\,k^2\,a^2+1)^2} \right), \tag{3.28}$$

which further yields (see **Appendix** E)

$$S_{1,2} = \tau^3 \frac{2\,N}{9} \left\{ \frac{3}{2} - \left(N^2 + \frac{3\,N}{2} + \frac{1}{2} \right) a^2 \right\} + \frac{\tau^3}{96\,a^2} \left\{ \left(\coth\left(\frac{\pi}{2\,a} \right) \right)^2 \pi^2 + 16\,a^2 \right\} + \frac{\tau^3}{96\,a^2} \left(-10\,\pi \coth\left(\frac{\pi}{2\,a} \right) a - \pi^2 \right) - \tau^3 \sum_{k=N+1}^{\infty} \left(-\frac{1}{(8k^2\,a^2+2)} + \frac{1}{6\,(4k^2\,a^2+1)^2} \right). \tag{3.29}$$

Using Lemma 1 (Eq. 3.20), we can approximate the sum after evaluating the integral,

$$\sum_{k=N+1}^{\infty} -\frac{1}{(8k^2\,a^2+2)} + \frac{1}{6\,(4k^2\,a^2+1)^2} = -\frac{20\,N^2\pi\,a^2 - 40\,N^2 \arctan(2\,Na)\,a^2 + 4\,N\,a}{(192\,N^2a^2+48)\,a} - \frac{5\,\pi - 10\,\arctan(2\,Na)}{(192\,N^2a^2+48)\,a} + \frac{1}{(16\,N^2a^2+4)} - \frac{1}{12\,(4\,N^2a^2+1)^2} - \frac{4\,Na^2}{3\,(8\,N^2a^2+2)^2} + \frac{2\,Na^2}{9\,(4\,N^2a^2+1)^3} + \cdots. \tag{3.30}$$

Substituting Eq. 3.30 in Eq. 3.29 followed by letting $N = 1/\sqrt{\tau}$, and expanding for small τ yields

$$S_{1,2} = -\frac{2\,a^2}{9}\tau^{\frac{3}{2}} - \frac{a^2\tau^2}{3} + \left(\frac{1}{3} - \frac{a^2}{9}\right)\tau^{\frac{5}{2}} + \frac{\tau^3}{96\,a^2}\left\{\pi^2\left(\coth\left(\frac{\pi}{2\,a}\right)\right)^2 - 10\,\pi\coth\left(\frac{\pi}{2\,a}\right)a - \pi^2 + 16\,a^2\right\} + \mathcal{O}\left(\tau^{\frac{7}{2}}\right). \quad (3.31)$$

The last term on the right hand side of Eq. 3.21 can be expressed in partial fractions as well, to yield

$$\begin{aligned}
S_{1,3} &= \sum_{k=1}^{N} \frac{128\,k^{10}\,a^{10}\tau^5}{15\,(4\,k^2\,a^2+1)^3} \\
&= \tau^5 \sum_{k=1}^{N}\left(\frac{2\,a^4k^4}{15} - \frac{a^2k^2}{10} + \frac{1}{20} - \frac{1}{48\,a^2k^2+12} - \frac{1}{120\,(4\,a^2k^2+1)^3} + \frac{1}{24\,(4\,a^2k^2+1)^2}\right) \\
&= \tau^5\left[\frac{2\,N}{75}\left\{\frac{15}{8} + \left(N^4 + \frac{5\,N^3}{2} + \frac{5\,N^2}{3} - \frac{1}{6}\right)a^4 + \left(-\frac{5\,N^2}{4} - \frac{15\,N}{8} - \frac{5}{8}\right)a^2\right\}\right] \\
&\quad + \tau^5\frac{2016\,N^4\arctan(2\,a\,N)\,a^4 - 1008\,N^4\pi\,a^4 - 272\,N^3a^3 + 1008\,N^2\arctan(2\,a\,N)\,a^2}{3840\,(4\,N^2a^2+1)^2\,a} \\
&\quad + \tau^5\frac{-504\,N^2\pi\,a^2 - 60\,a\,N + 126\,\arctan(2\,a\,N) - 63\,\pi}{3840\,(4\,N^2a^2+1)^2\,a} - \tau^5\sum_{k=1}^{\infty}\frac{1}{12\,(4\,k^2\,a^2+1)} \\
&\quad - \tau^5\sum_{k=1}^{\infty}\frac{1}{120\,(4\,k^2\,a^2+1)^3} + \tau^5\sum_{k=1}^{\infty}\frac{1}{24\,(4\,k^2\,a^2+1)^2} + \tau^5\sum_{k=N+1}^{\infty}\frac{1}{12\,(4\,k^2\,a^2+1)} \\
&\quad \tau^5\sum_{k=N+1}^{\infty}\frac{1}{120\,(4\,k^2\,a^2+1)^3} - \tau^5\sum_{k=N+1}^{\infty}\frac{1}{24\,(4\,k^2\,a^2+1)^2}.
\end{aligned} \quad (3.32)$$

Again using Lemma 1, evaluating the relevant integrals, considering $N = 1/\sqrt{\tau}$, and expanding for small τ, we obtain

$$S_{1,3} \approx \frac{2\,a^4}{75}\tau^{\frac{5}{2}} + \frac{a^4\tau^3}{15} + \mathcal{O}\left(\tau^{\frac{7}{2}}\right). \quad (3.33)$$

Finally, the first term of Eq. 3.19 for small τ is

$$S_1(\tau) \approx S_{1,1} + S_{1,2} + S_{1,3} = \sqrt{\tau} + \frac{\tau}{4\,a}\left(-\pi \coth\left(\frac{\pi}{2\,a}\right) + 2\,a\right) + \left(\frac{1}{4\,a^2} - \frac{2\,a^2}{9}\right)\tau^{\frac{3}{2}} + \left(-\frac{1}{8\,a^2} - \frac{a^2}{3}\right)\tau^2 + \left(-\frac{1}{48\,a^4} + \frac{1}{24\,a^2} + \frac{1}{3} - \frac{a^2}{9} + \frac{2\,a^4}{75}\right)\tau^{\frac{5}{2}} + \left[\frac{1}{32\,a^4} + \frac{1}{96\,a^2}\left\{\left(\coth\left(\frac{\pi}{2\,a}\right)\right)^2\pi^2 - 10\coth\left(\frac{\pi}{2\,a}\right)\pi\,a - \pi^2 + 16\,a^2\right\} + \frac{a^4}{15}\right]\tau^3 + \mathcal{O}\left(\tau^{\frac{7}{2}}\right). \tag{3.34}$$

3.4.2 Second term of Eq. 3.19

Considering now the second term of Eq. 3.19, we will again write it as an integral plus a sum of discrete terms (Lemma 1). For the integral, writing y in place of k, treating y as large and τ as small, we obtain

$$\frac{1}{\sqrt{1+4\,y^2\,a^2}}\sin\left(\frac{4y^2\,a^2}{\sqrt{1+4\,y^2\,a^2}}\tau\right) \approx \frac{\sin(2\,a\,\tau\,y)}{2\,a\,y} - \frac{\cos(2\,a\,\tau\,y)\,\tau}{8\,a^2y^2} + \frac{1}{y^3}\left(-\frac{\sin(2\,a\,\tau\,y)}{16\,a^3} - \frac{\sin(2\,a\,\tau\,y)\,\tau^2}{64\,a^3}\right) + \frac{1}{y^4}\left(\frac{\cos(2\,a\,\tau\,y)\,\tau}{64\,a^4} + \frac{\cos(2\,a\,\tau\,y)\,\tau\,\left(\tau^2+18\right)}{768\,a^4}\right) + \frac{1}{y^5}\left(\frac{3\sin(2\,a\,\tau\,y)}{256\,a^5} + \frac{\sin(2\,a\,\tau\,y)\,\tau^2}{512\,a^5} + \frac{\sin(2\,a\,\tau\,y)\,\tau^2\left(\tau^2+72\right)}{12288\,a^5}\right) + \text{h.o.t.} \tag{3.35}$$

The first term in the RHS of Eq. 3.35, when integrated over $[N,\infty)$, can be expressed as

$$\int_N^\infty \frac{\sin(2\,a\,\tau\,y)}{2\,a\,y}\,\mathrm{d}y = \int_0^\infty \frac{\sin(2\,a\,\tau\,y)}{2\,a\,y}\,\mathrm{d}y - \int_0^N \frac{\sin(2\,a\,\tau\,y)}{2\,a\,y}\,\mathrm{d}y = \frac{\pi}{4\,a} - \int_0^N \frac{\sin(2\,a\,\tau\,y)}{2\,a\,y}\,\mathrm{d}y. \tag{3.36}$$

A trick used in Eq. 3.36 may be noted. Although the integrand has been obtained using a large-y expansion, as far as the integral itself goes, Eq. 3.36 is exact. In Eq. 3.36, y is simply a dummy variable of integration. In particular, the last integral uses small values of the argument of the sine. In that final integral, since $y\tau$ is small for all $y \in (0, N)$, series expansion of $\sin(2ay\tau)/2ay$ and then term by term integration is possible (details omitted for brevity). The rest of the terms in the right hand side of Eq. 3.35 can be routinely

integrated by parts to obtain asymptotic approximations (see page 252 of Bender and Orszag [60] for examples).

Accordingly, the integral on the right hand side of Eq. 3.35 with the limits $N = 1/\sqrt{\tau}$ to ∞ results in

$$\int_{\frac{1}{\sqrt{\tau}}}^{\infty} \frac{1}{\sqrt{1+4y^2\,a^2}} \sin\left(\frac{4\,a^2\,y^2}{\sqrt{1+4\,a^2\,y^2}}\tau\right) \mathrm{d}y = \frac{\pi}{4\,a} - \sqrt{\tau} - \frac{-1981808640\,a^4 + 2229534720}{8918138880\,a^2}\tau^{\frac{3}{2}} + \frac{3\,\pi\,\tau^2}{16\,a} - \frac{1}{8918138880\,a^4}\left(2972712960\,a^4 - 185794560 + \frac{1189085184\,a^8}{5}\right)\tau^{\frac{5}{2}} + \mathcal{O}\left(\tau^{\frac{7}{2}}\right). \tag{3.37}$$

The second term of Eq. 3.19 requires us to subtract some discrete terms as well:

$$\left(\frac{1}{2}\,f(N,\tau) + \frac{1}{12}\frac{\partial f(y,\tau)}{\partial y}\bigg|_{y=N} - \frac{1}{720}\frac{\partial^3 f(x,\tau)}{\partial x^3}\bigg|_{x=N}\right)\bigg|_{N=\frac{1}{\sqrt{\tau}}} = \frac{\tau}{2} - \frac{\tau^2\left(480\,a^4+180\right)}{1440\,a^2} - \frac{160\,a^4-60}{1440\,a^2}\tau^{\frac{5}{2}} - \frac{\tau^3\left(-96\,a^8-240\,a^4-45\right)}{1440\,a^4} + \mathcal{O}\left(\tau^{\frac{7}{2}}\right). \tag{3.38}$$

Hence,

$$S_2(\tau) \approx \frac{\pi}{4\,a} - \sqrt{\tau} - \frac{\tau}{2} + \frac{3}{16\,a^4}\left(\frac{32\,a^6}{27} - \frac{4\,a^2}{3}\right)\tau^{\frac{3}{2}} + \frac{3\,\tau^2}{16\,a^4}\left(\frac{16\,a^6}{9} + \pi\,a^3 + \frac{2\,a^2}{3}\right) + \frac{-18816\,a^{10} + 78400\,a^8 - 235200\,a^6 - 29400\,a^4 + 14700\,a^2}{705600\,a^6}\tau^{\frac{5}{2}} + \frac{3\,\tau^3}{16\,a^4}\left(-\frac{16\,a^8}{45} - \frac{8\,a^4}{9} - \frac{1}{6}\right) + \mathcal{O}\left(\tau^{\frac{7}{2}}\right). \tag{3.39}$$

We now have both terms needed for Eq. 3.19. Adding them up, Eq. 3.18 for small τ yields

$$S(\tau) = \frac{\pi}{4\,a} - \frac{\pi}{4\,a}\coth\left(\frac{\pi}{2\,a}\right)\tau + \frac{3\,\pi\,\tau^2}{16\,a} + \frac{\left(\pi^2 - 5\,\pi\,a\sinh\left(\frac{\pi}{a}\right)\right)}{\cosh\left(\frac{\pi}{a}\right)-1}\frac{\tau^3}{48\,a^2} + \mathcal{O}\left(\tau^4\right) \text{ for small } \tau. \tag{3.40}$$

Therefore, the central slope or rotation of the simply supported Rayleigh beam of length L, with all other parameters set to unity, and with a unit angular impulse acting at $x = \frac{L}{2}$,

is

$$u_{,x}\left(x=\frac{L}{2},\tau\right)=\frac{2}{L}\,S(\tau)=\frac{2\,a}{\pi}\,S(\tau)=\frac{1}{2}-\frac{\coth\left(\frac{\pi}{2\,a}\right)}{2}\,\tau+\frac{3}{8}\,\tau^2+\frac{\left(\pi-5\,a\sinh\left(\frac{\pi}{a}\right)\right)}{\left(\cosh\left(\frac{\pi}{a}\right)-1\right)}\frac{\tau^3}{24\,a}$$
$$+\,\mathcal{O}\left(\tau^4\right)\ \text{for small}\ \tau. \quad (3.41)$$

For long beams, $a=\frac{\pi}{L}\to 0$, and the response any point x is asymptotically given by

$$u_{,x}(x,\tau)=\frac{1}{2}-\frac{\tau}{2}+\frac{3}{8}\tau^2-\frac{5}{24}\tau^3+\mathcal{O}\left(\tau^4\right). \quad (3.42)$$

Now, if a less violent moment $M(\tau)$ acts there for some short time interval, then the angular rotation at that location will be given by the convolution integral

$$\frac{2}{L}\int_0^\tau M(\tau-\xi)\,S(\xi)\,\mathrm{d}\xi. \quad (3.43)$$

In particular, if $M(\tau)=M_0$, a constant, then we have

$$\frac{2M_0}{L}\int_0^\tau S(\xi)\,\mathrm{d}\xi=M_0\left(\frac{\tau}{2}-\frac{\coth\left(\frac{\pi}{2\,a}\right)}{4}\tau^2+\cdots\right). \quad (3.44)$$

For a long beam, $\coth\left(\frac{\pi}{2\,a}\right)\to 1$, and we have

$$M_0\left(\frac{\tau}{2}-\frac{\coth\left(\frac{\pi}{2\,a}\right)}{4}\tau^2+\cdots\right)\to M_0\left(\frac{\tau}{2}-\frac{1}{4}\tau^2+\cdots\right). \quad (3.45)$$

We note that the response to a suddenly applied constant moment causes a sudden change in angular velocity but not in rotation, and so it involves bounded strains in the beam.

3.5 Numerical verification

The accuracy of the asymptotic approximation in Eq. 3.41 is displayed in Fig. 3.5. It is clear that the match is good for small τ.

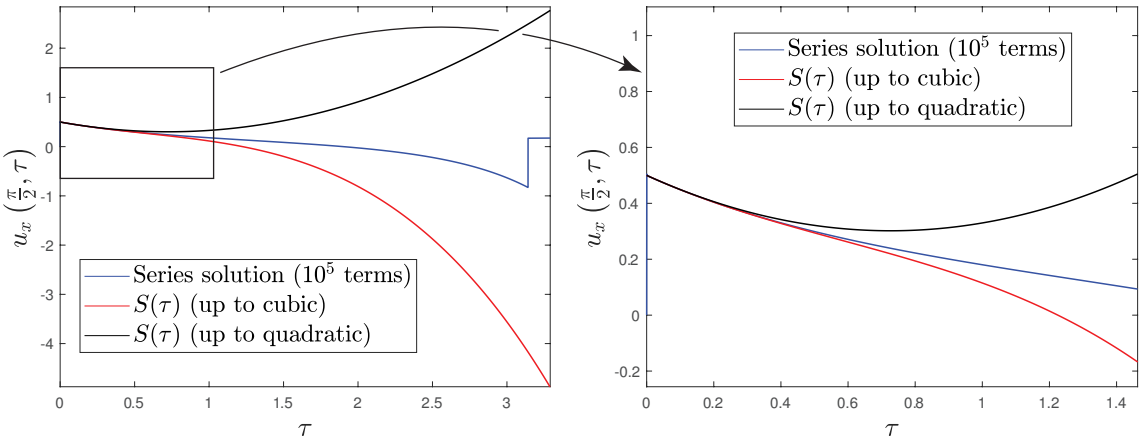

FIGURE 3.5: The series solution (10^5 terms) of $u_x\,(L/2,\tau)$ and its asymptotic approximation for small τ when $L=\pi$. Both plots show both quadratic and cubic approximations. The plot on the right shows a smaller time interval to ease comparison for small τ.

To verify numerically that all terms computed in Eq. 3.41 are correct, we subtract the asymptotic expression from the series solution (with 10^5 terms). The remaining error term should be proportional to τ^4. A plot of that error against τ^4 for small τ^4 should be close to a straight line passing through zero. Such is indeed the case, as seen in Fig. 3.6. The spike seen Fig. 3.6 for super-small τ is actually not from the asymptotic approximation but from fast Gibbs oscillations in the truncated series solution. We conclude that, from the numerical evidence, the series computed indeed is correct up to $\mathcal{O}(\tau^3)$.

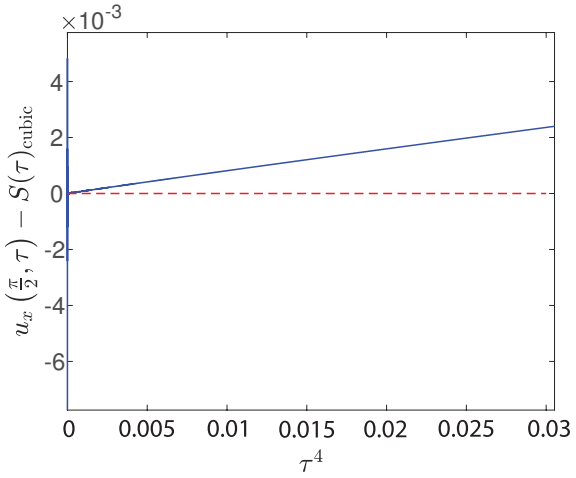

FIGURE 3.6: Numerical verification of $S(\tau)$ up to cubic term.

3.6 Results and discussion

The prior literature contains several papers on the short time response of some slender structures to *linear* impulses, or impulsive forces, concentrated at points in space. However, the rotational response of slender structures to angular impulses has not been studied. The simplest slender structure, namely the Euler-Bernoulli beam, predicts strongly unphysical responses to angular impulses. The infinite beam has an instantaneously unbounded rotational response, while a finite-length beam shows strong arrivals of high frequency reflections from the boundary.

In contrast to the Euler-Bernoulli beam (which does not incorporate cross-sectional rotary inertia), the Rayleigh beam incorporates rotary inertia and yet retains simplicity because it uses the same kinematics. This gives more physically reasonable results under impulsive moments. Interestingly the Rayleigh beam and an Eringen stress gradient theory based beam are governed by the same equation. A study of such structures under impulsive moments can have some practical value in that it may shed light on peculiarities observed in some experimental situations like long beams on which a motor is suddenly braked to a halt. However, in this case our interest has been primarily academic. Using dimensional analysis followed by asymptotic approximations, we have computed the short-time response of such a beam to an angular impulse. The response is found to contain an instantaneous finite jump (unlike an unbounded jump for the Euler-Bernoulli beam), followed by regular behavior well described by a polynomial in nondimensional time for a finite duration, until simultaneous arrival of multi-frequency reflections from boundaries causes further discontinuities in the response. We note that, although the rotational response to the angular impulse is bounded as $t \to 0$, the resulting strain in the beam is unbounded. As a result, for realistic modeling of beams with such an angular impulse, a nonlinear material model will be needed. However, if the actual moment applied is in fact a smooth function of time, and the impulse response computed above is used merely as a Green's function, then finite responses with finite strains will occur. Recall, e.g., Eq. 3.44. With these thoughts, we acknowledge that nonlinearity may play a role in some situations with

some loadings for some problems. But our basic elastic solution has its own fundamental theoretical validity, and is the main contribution of this paper.

We have investigated this problem using dimensional analysis, modal expansion, series solutions, finite element simulations, and asymptotic approximations for the short-time polynomial behavior. Agreement between solutions obtained using different means has been excellent. This work provides new theoretical results for a problem that has not been examined before. These results shed some light on some peculiarities of the response as explained above. Moreover, we hope that that methods used here will be of interest to a general readership interested in both asymptotic analyses as well as structural vibrations.

We now move on to the next contribution of this thesis. A catenary is a limiting case of a beam where the flexural rigidity goes to zero. In the next chapter, the dynamics of a slack catenary will be discussed.

Chapter 4

Small In-plane Oscillations of a Slack Catenary using Assumed Modes

4.1 Introduction

The dynamics of hanging chains has been studied by several authors over more than a century. Routh [63] wrote equations for the uniform chain but provided analytical solutions for a non-uniform chain whose equilibrium shape is a cycloid. The equilibrium shape of a sagging inextensible chain with uniform mass per unit length is in fact a hyperbolic cosine (see, e.g., [64]). Pugsley [65] conducted experiments and gave semi-empirical expressions for first three natural frequencies of a catenary. Saxon and Cahn [66] studied the problem analytically and gave an asymptotic solution for small sag to span ratio. Their results were in agreement with Pugsley [65]. An approximate solution of equations from Routh [63] and Saxon et al. [66] was found by Goodey [67]. The expressions obtained were close to the empirical formulas of Pugsley [65].

The catenary with small sag to span ratio leads to an apparent contradiction, as noted by Irvine and Caughey [68]. For very small sag to span ratios, the first mode is antisymmetric. However, for a flat and taut string, the first mode is symmetric. The contradiction arises because at extremely small sag, the tension is very high, and an extensible-chain treatment is needed to obtain the flat-string behavior. However, in this chapter, we are not interested in that regime: we examine the catenary in the regime where the sag to span ratio is neither very small nor very large.

With newer computational techniques, more detailed studies of more complex chain systems were possible. Simpson [69] used a transfer matrix approach to study a multi-span transmission line. Finite Element Analysis (FEA) was used as well [70, 71]. Karoumi [72] examined a model with catenary cables supporting a bridge deck.

Rega [73, 74] has presented a detailed discussion of the dynamics of *extensible* cables beginning from a continuum mechanics framework and considering both various analytical simplifications as well as detailed solution aspects only obtainable using numerical methods. The reader may refer to these two excellent papers for many more references relevant to the dynamics of a catenary and related problems.

In contrast to the above papers which either allow extensibility, or assume small sag, or discretize the system using finite elements and move to a fully numerical treatment, in this study we address the strictly inextensible catenary, with large sag, using the Lagrangian approach and assumed modes[1]. The assumed modes approach has enjoyed wide adoption in mechanics because of its conceptual simplicity, ease of refinement to useful accuracy, focus on essential kinematics, sidestepping of natural boundary conditions, and direct use in the Lagrangian approach. The interested reader may see a few examples in the following papers: drum vibrations in [75], rotor dynamics in [76, 77], flexible multibody systems in [78], an application in piezoelectric energy harvesting in [79], and the dynamics of flexible robots in [80], among many more in the literature. We note that the catenary itself continues to appear in research papers devoted to more complicated interactions,

[1]The assumed modes approach is also called the Rayleigh-Ritz approach.

such as cable robots [81] and catenary risers in marine applications [82]. However, we have not found any assumed-mode treatment of the catenary in literature.

Following the above discussion, we can now introduce the problem studied in this chapter and point out its interesting features to motivate our work. We study small in-plane oscillations of an inextensible catenary with considerable sag, i.e., a slack catenary. We begin with the well known static equilibrium configuration of the catenary. We use the horizontal spatial coordinate as an independent variable during the initial setup of the problem. After introducing assumed modes for small vertical displacements of the chain, as is usual within the Lagrangian formulation, we retain only time as an independent variable. The pointwise inextensibility of the chain relates small vertical and horizontal displacements through a differential equation, which we can integrate to obtain the horizontal displacements. Taking one endpoint of the chain to be fully fixed and the vertical location of the other, or distal, endpoint to be fixed as well, it is convenient to impose the horizontal location of the distal endpoint through an explicit scalar constraint equation which introduces a Lagrange multiplier. A key aspect of this approach is that the potential energy of the system is *linear* and not *quadratic* in the displacements, and so the equations of motion obtained using the Lagrangian approach have some nonzero terms, including the Lagrange multiplier, that survive even when the displacements are set to zero. Since zero displacement represents equilibrium, these nonzero terms must necessarily add up to zero. Setting their sum to zero determines the Lagrange multiplier. Physically, this means the frequency remains indeterminate until horizontal fixity of the second endpoint of the chain is enforced. Furthermore, in a subsequent calculation, when we do not use arbitrary shape functions in the assumed modes and instead use the correct modes as determined in the first part, then those erstwhile nonzero terms become identically zero and the Lagrange multiplier becomes indeterminate within the linear approximation. In this case, retaining quadratic terms in a nonlinear treatment leads to a potential energy which includes quadratic terms, and the problem becomes determinate. In this way, this seemingly simple classical problem leads to clear, potentially useful, and in our opinion pleasing academic insights into both oscillations as well as the role of constraints within

Lagrangian mechanics.

4.2 Problem setup

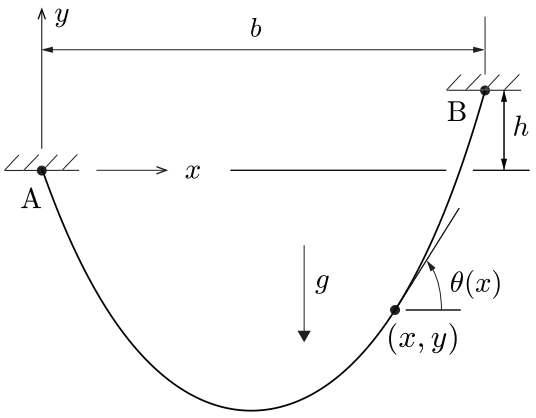

FIGURE 4.1: A slack catenary hanging from two fixed points. Gravity acts downward. Without loss of generality, we take $h \geq 0$.

We consider an inextensible, slack catenary (Fig. 4.1) of length L and a uniform mass $\bar{m}$ per unit length, hanging from two fixed ends A and B. We use a coordinate system with origin at A. The end B is at the point (b, h), with $h \geq 0$. Gravity acts along the negative y direction. The tangent to the equilibrium curve at location x makes an angle $\theta(x)$ with the positive x direction. Denoting the equilibrium shape as $y(x)$, we have

$$y(0) = 0 \quad \text{and} \quad y(b) = h. \tag{4.1}$$

By nondimensionalization or by choice of units, we take $L = 1$, $\bar{m} = 1$, and $g = 1$. Although our treatment is general, analytical intractability forces us to use numerical integrals. So we will study two cases in detail: $h = 0$ and $h = 0.1$, with $b = 0.6$ in both cases.

4.2.1 Equilibrium

If T is the spatially varying tension in the chain, equilibrium requires

$$\frac{\mathrm{d}}{\mathrm{d}x}\left(T\cos(\theta)\right) = 0, \text{ and} \tag{4.2}$$

$$\frac{\mathrm{d}}{\mathrm{d}x}\left(T\sin(\theta)\right) = \bar{m}\,g\,\sec(\theta). \tag{4.3}$$

From Eq. 4.2, $T\cos(\theta) = T_0$, a constant, whence Eq. 4.3 yields

$$\frac{\mathrm{d}^2y}{\mathrm{d}x^2} = \frac{1}{W}\sqrt{1+\left(\frac{\mathrm{d}y}{\mathrm{d}x}\right)^2} = \frac{1}{W}\sec(\theta), \quad \text{where } W = \frac{T_0}{\bar{m}\,g}. \tag{4.4}$$

Solution of Eq. 4.4 with $y(0) = 0$ yields

$$y = -W\cosh(C) + W\cosh\left(C + \frac{x}{W}\right), \tag{4.5}$$

where W and C are constants to be determined numerically from the boundary condition $y(b) = h$ and the length condition

$$\int_0^b \sec(\theta)\,\mathrm{d}x = \int_0^b \sqrt{1+\left(\frac{\mathrm{d}y}{\mathrm{d}x}\right)^2}\,\mathrm{d}x = L. \tag{4.6}$$

For example, with $b = 0.6$ and $h = 0$, we have $W = 0.1631683$ and $C = -1.8385927$; and with $b = 0.6$ and $h = 0.1$, we have $W = 0.1640525$ and $C = -1.7283471$.

4.2.2 Inextensibility constraint

Let $u(x,t)$ and $v(x,t)$ be the displacement components along x and y directions respectively. The length of a small element, even after displacement, remains unchanged. In Fig. 4.2, the endpoints P and Q of an element of length $\mathrm{d}s$ move to P′ and Q′. Inextensibility requires

$$\mathrm{d}s^2 = \mathrm{d}x^2 + \mathrm{d}y^2 = \left(1+\frac{\partial u}{\partial x}\right)^2\mathrm{d}x^2 + \left(\frac{\mathrm{d}y}{\mathrm{d}x} + \frac{\partial v}{\partial x}\right)^2\mathrm{d}x^2. \tag{4.7}$$

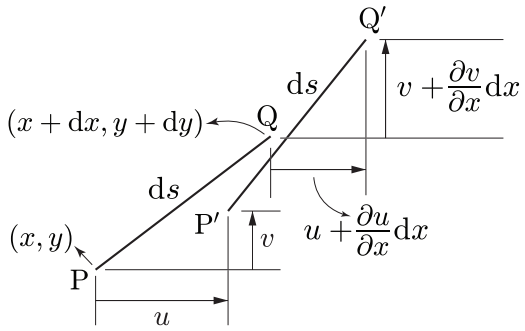

FIGURE 4.2: An element of length 'ds' in equilibrium and displaced configuration.

Using subscripts and primes to denote partial and ordinary derivatives with respect to x, we obtain the pointwise *differential* constraint

$$1 + y'^2 = (1 + u_x)^2 + \left(y' + v_x\right)^2 = (1 + u_x)^2 + y'^2 + 2\,y'\,v_x + v_x^2. \tag{4.8}$$

Therefore

$$(1 + u_x)^2 = 1 - 2\,y'\,v_x - v_x^2, \tag{4.9}$$

which simplifies to

$$u_x = \sqrt{1 - 2\,y'\,v_x - {v_x}^2} - 1, \tag{4.10}$$

where the sign on the square root is chosen to ensure that u is infinitesimal when v is infinitesimal. Note that, if v is expanded using assumed modes, then u can be found by integration with respect to x so that inextensibility is obeyed pointwise.

4.2.3 Horizontal fixity of the right endpoint

In an assumed modes approach, we can easily enforce $v(0,t) = v(b,t) = 0$ by using, e.g., a truncated Fourier sine series. Substituting that expression into Eq. 4.10, we can in principle integrate with respect to x to obtain $u(x,t)$. Enforcing $u(0,t) = 0$ is done by taking the lower limit of the integral to be $x = 0$. However, for a general assumed modes expansion, $u(b,t) = 0$ is not guaranteed and must be enforced as an additional constraint.

Since we are interested in small oscillations of the chain, we assume u, v, and their spatial derivatives to be small. For small v_x, Eq. 4.10 has a Taylor series approximation, i.e.,

$$u_x = -y'\, v_x - \frac{1}{2}\left(1 + y'^2\right) {v_x}^2 + \cdots . \tag{4.11}$$

Integrating Eq. 4.11 in space, the horizontal component u can be approximated using

$$u = \int_0^x \left(- y'(\xi)\, v_\xi - \frac{1}{2}\left(1 + y'(\xi)^2\right) {v_\xi}^2 + \cdots \right) \mathrm{d}\xi. \tag{4.12}$$

We now introduce our assumed modes

$$v(x,t) = \sum_{k=1}^{N} a_k(t) \sin\left(\frac{k\pi x}{b}\right), \tag{4.13}$$

as mentioned above. The corresponding horizontal displacement u does not automatically satisfy $u(b,t) = 0$. We therefore include the constraint

$$u(b,t) = \int_0^b \left(- y'(x)\, v_x - \frac{1}{2}\left(1 + y'(x)^2\right) {v_x}^2 + \cdots \right) \mathrm{d}x = 0. \tag{4.14}$$

Although the constraint is holonomic, we do not use it to eliminate a degree of freedom because we do not wish to make *a priori* assumptions about which term in the Fourier sine series can be eliminated. We now proceed to write equations of motion.

4.3 Equations of motion

The kinetic energy of the catenary is

$$\mathcal{T} = \frac{1}{2} \int_0^b \bar{m} \left(\dot{u}^2 + \dot{v}^2\right) \sec(\theta)\, \mathrm{d}x \tag{4.15}$$

where the overdot denotes a partial derivative with respect to time, and the potential energy of the catenary, after subtracting a constant corresponding to the equilibrium

configuration, is

$$\mathcal{V} = \int_0^b \bar{m}\, g\, v\, \sec(\theta)\, \mathrm{d}x. \tag{4.16}$$

The Lagrangian

$$\mathcal{L} = \mathcal{T} - \mathcal{V}, \tag{4.17}$$

and the equations of motion are

$$\frac{\mathrm{d}}{\mathrm{d}t}\left(\frac{\partial \mathcal{L}}{\partial \dot{a}_k}\right) - \frac{\partial \mathcal{L}}{\partial a_k} = \lambda \frac{\partial}{\partial a_k}\left(u(b,t)\right), \quad k = 1, 2, \ldots, N. \tag{4.18}$$

In the above, $u(b,t)$ stands for the definite integral in Eq. 4.14, and λ is to be determined as part of the solution. For small oscillations, we want equations that are correct up to first order in the generalized coordinates a_k. This means that for computing the kinetic energy in Eq. 4.15, the integral of Eq. 4.12 must be evaluated only up to first order in the a_k. However, because the expression for $u(b,t)$ in the constraint equation is differentiated once, the integral of Eq. 4.14 must be evaluated up to second order in the a_k. The latter takes the form

$$u(b,t) = \boldsymbol{a}^\top \boldsymbol{q} + \frac{1}{2}\,\boldsymbol{a}^\top \mathbf{B}\,\boldsymbol{a} + \cdots = 0, \tag{4.19}$$

where $\boldsymbol{a} = [a_1, a_2, \ldots, a_N]^\top$ and $\mathbf{B}$ is a constant symmetric matrix of size $N \times N$, or $\mathbf{B} \in \mathbb{R}^{N\times N}$. Then Eqs. 4.18 take the form

$$\mathbf{M}\,\ddot{\boldsymbol{a}} + \boldsymbol{p} = \lambda\,\boldsymbol{q} + \lambda\,\mathbf{B}\,\boldsymbol{a}, \tag{4.20}$$

where the constant vectors $\boldsymbol{p}$ and $\boldsymbol{q}$ are generally nonzero (the degenerate case will be discussed in Section 4.5). Since $\boldsymbol{a}$ is zero at equilibrium, the terms in $\boldsymbol{p}$ and $\boldsymbol{q}$ must cancel exactly at equilibrium. We therefore expect that $\boldsymbol{p}$ and $\boldsymbol{q}$ are parallel, as indeed they are (see appendix F). In Eq. 4.20, $\mathbf{M}$ is a symmetric positive definite matrix of size $N \times N$.

We must now determine λ correct up to linear terms. Considering equilibrium in Eq. 4.20, let $\boldsymbol{a} = \mathbf{0}$, and $\lambda = \lambda_0$. Then

$$\boldsymbol{p} = \lambda_0\,\boldsymbol{q}. \tag{4.21}$$

If the vectors $\boldsymbol{p}$ and $\boldsymbol{q}$ are nonzero, their parallelism ensures that a unique λ_0 can be determined. Having determined λ_0, we can consider small motions. For small $\boldsymbol{a}$, let

$$\lambda = \lambda_0 + \eta, \tag{4.22}$$

where η is of the same order of magnitude as $||\boldsymbol{a}||$. Substituting Eq. 4.22 in Eq. 4.20, and using Eq. 4.21, we obtain up to first order,

$$\mathbf{M}\,\ddot{\boldsymbol{a}} = \eta\,\boldsymbol{q} + \lambda_0\,\mathbf{B}\,\boldsymbol{a}. \tag{4.23}$$

Linearizing Eq. (4.19), we see that the vector $\boldsymbol{a}$ must lie on $\mathcal{X}$, the $(N-1)$ dimensional subspace of $\mathbb{R}^N$ that is orthogonal to $\boldsymbol{q}$. Hence, we write

$$\boldsymbol{a} = \mathbf{Q}\,\boldsymbol{\zeta}, \tag{4.24}$$

where the matrix $\mathbf{Q}$, of size $N \times (N-1)$, provides a basis for $\mathcal{X}$. Note that in the software package Matlab, such a $\mathbf{Q}$ can be easily obtained using the "qr" decomposition. We now have

$$\mathbf{Q}^\top \boldsymbol{q} = \mathbf{0}. \tag{4.25}$$

The vector $\boldsymbol{\zeta} = [\zeta_1, \zeta_2, \ldots, \zeta_{N-1}]^\top$ contains time varying coordinates in the new basis. Substituting Eq. 4.24 in Eq. 4.23, and premultiplying with $\mathbf{Q}^\top$, we obtain

$$\tilde{\mathbf{M}}\,\ddot{\boldsymbol{\zeta}} = \lambda_0\,\tilde{\mathbf{B}}\,\boldsymbol{\zeta}, \tag{4.26}$$

where $\tilde{\mathbf{M}} = \mathbf{Q}^\top\,\mathbf{M}\,\mathbf{Q}$ and $\tilde{\mathbf{B}} = \mathbf{Q}^\top\,\mathbf{B}\,\mathbf{Q}$, and $\tilde{\mathbf{M}}, \tilde{\mathbf{B}} \in \mathbb{R}^{(N-1)\times(N-1)}$.

The finally obtained equation (Eq. 4.26) yields an eigenvalue problem which can be solved for $\boldsymbol{\zeta}$. Subsequently, $N-1$ physical mode shapes can be found from Eq. 4.24.

4.4 Numerical results

We now present numerical results for two cases mentioned in Section 4.2. Numerical calculations were carried out to several digits more than those displayed.

4.4.1 Case 1: $h = 0$

This case refers to a catenary which is symmetrically suspended between two points. We obtain

$$\mathbf{M} = \begin{bmatrix} 3.4764 & 2.5342 & 1.6515 & 2.2369 \\ 2.5342 & 3.3974 & 1.7375 & 2.4056 \\ 1.6515 & 1.7375 & 2.3715 & 1.5337 \\ 2.2369 & 2.4056 & 1.5337 & 3.1275 \end{bmatrix}, \mathbf{B} = \begin{bmatrix} -38.9759 & 0 & -55.2220 & 0 \\ 0 & -127.3652 & 0 & -125.5176 \\ -55.2220 & 0 & -262.1130 & 0 \\ 0 & -125.5176 & 0 & -447.1589 \end{bmatrix}, \tag{4.27}$$

and

$$\boldsymbol{p} = \begin{Bmatrix} 0.5195 \\ 0 \\ 0.3562 \\ 0 \end{Bmatrix}, \boldsymbol{q} = \begin{Bmatrix} 3.1838 \\ 0 \\ 2.1830 \\ 0 \end{Bmatrix}. \tag{4.28}$$

From Eq. 4.21, $\lambda_0 = 0.1631682$. The first three angular frequencies are found to be 2.4294, 4.3590, and 6.1950. The corresponding mode shapes are shown in Fig. 4.3.

4.4.2 Case 2: $h = 0.1$

This case refers to a catenary which is asymmetrically suspended between two points. We obtain

$$\mathbf{M} = \begin{bmatrix} 3.2559 & 2.1171 & 1.2612 & 2.0685 \\ 2.1171 & 2.9911 & 1.1606 & 2.0895 \\ 1.2612 & 1.1606 & 1.9750 & 0.9706 \\ 2.0685 & 2.0895 & 0.9706 & 2.9150 \end{bmatrix}, \mathbf{B} = \begin{bmatrix} -39.1116 & 10.7499 & -55.2174 & 9.7637 \\ 10.7499 & -127.8014 & 27.0240 & -125.5289 \\ -55.2174 & 27.0240 & -263.1210 & 49.8938 \\ 9.7637 & -125.5289 & 49.8938 & -449.0069 \end{bmatrix}, \tag{4.29}$$

and

$$\boldsymbol{p} = \begin{Bmatrix} 0.5205 \\ -0.0435 \\ 0.3551 \\ -0.0268 \end{Bmatrix}, \ \boldsymbol{q} = \begin{Bmatrix} 3.1725 \\ -0.2650 \\ 2.1648 \\ -0.1636 \end{Bmatrix}. \tag{4.30}$$

From Eq. 4.21, $\lambda_0 = 0.1640525$. The first three angular frequencies are 2.4375, 4.3952, and 6.2196. The corresponding mode shapes are shown in Fig. 4.4.

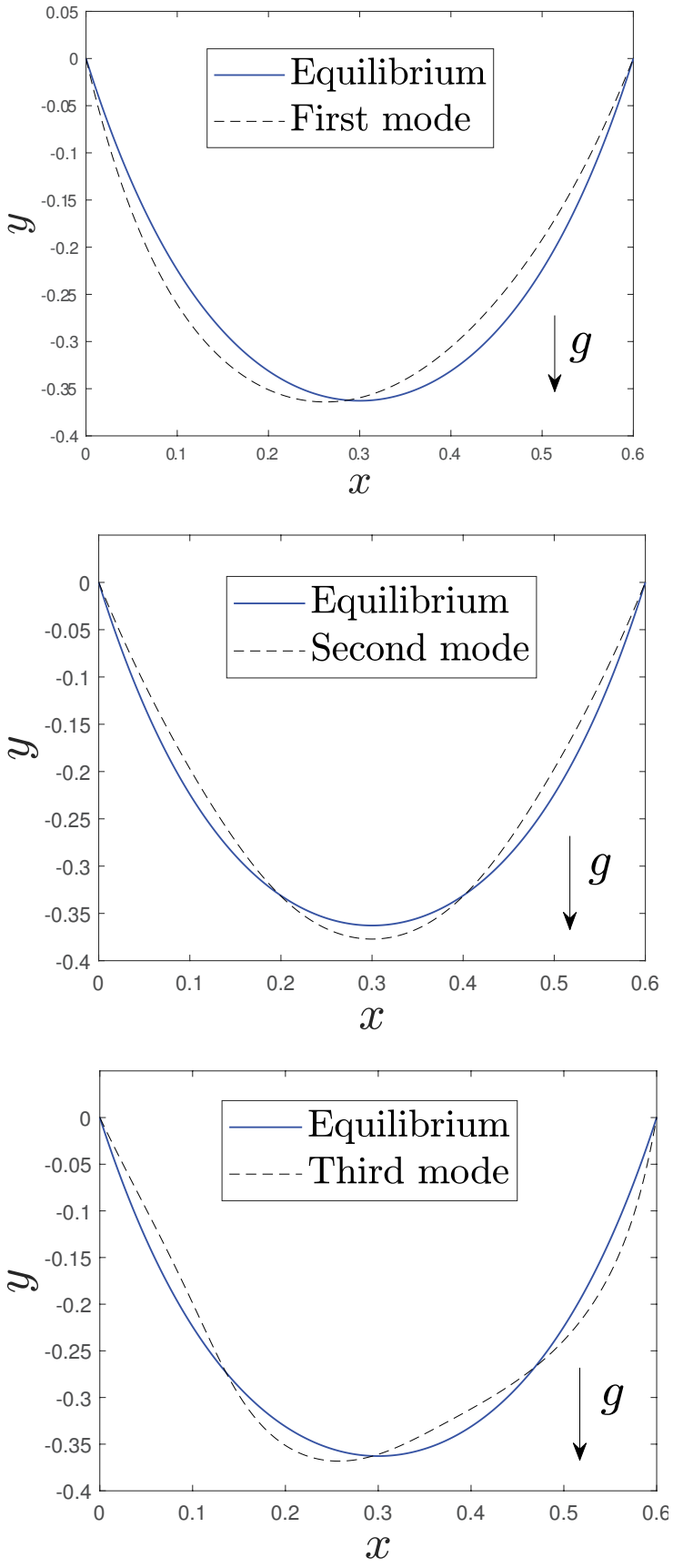

FIGURE 4.3: First three mode shapes of the in-plane oscillations of the catenary with $h = 0$. The solid lines show the equilibrium shape.

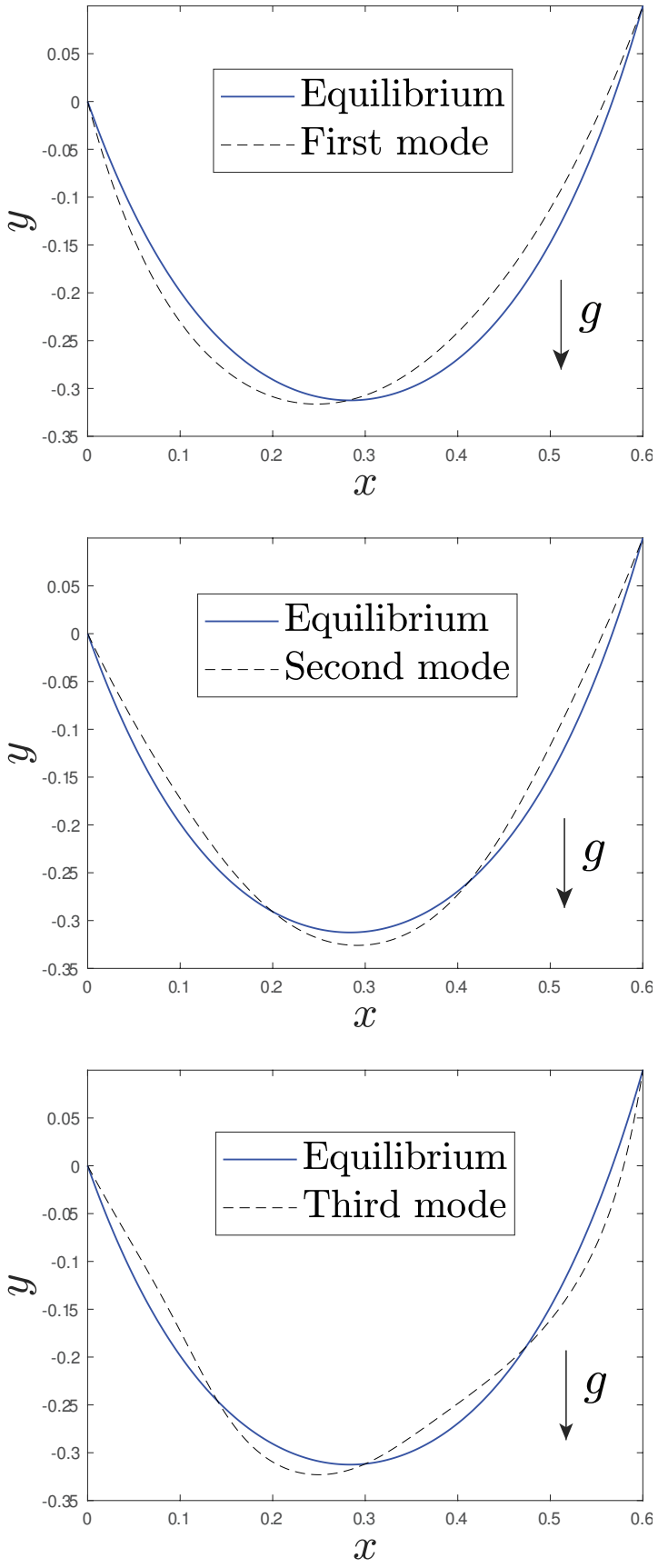

FIGURE 4.4: First three modes of the asymmetrically suspended catenary with $h = 0.1$. The solid lines show the equilibrium shape.

4.5 Degeneracy encountered with actual modes

In usual applications of the Rayleigh Ritz approach (or assumed modes), exact results are obtained when the exact mode shape is used. In this problem, however, use of the mode shapes obtained above leads to an interesting degenerate condition. Specifically, the constraint Eq. 4.19 is satisfied to first order, which means $\boldsymbol{q}$ is zero. There is no inconsistency, and $\boldsymbol{p}$ is zero as well. However, now Eq. 4.21 cannot be solved for λ_0. In other words, when the very modes obtained above are used in the assumed modes calculation in the form

$$v = a_1\,\psi_1 + a_2\,\psi_2 + a_3\,\psi_3 + \cdots\,, \tag{4.31}$$

then we obtain

$$\mathbf{M}\,\ddot{\boldsymbol{a}} = \lambda\,\mathbf{B}\,\boldsymbol{a}, \tag{4.32}$$

with the vectors $\boldsymbol{p}$ and $\boldsymbol{q}$ becoming individually zero. Now λ is indeterminate[2] within the linear formulation.

The reason for this loss of the λ-determining vectors $\boldsymbol{p}$ and $\boldsymbol{q}$ is not that mode shapes are used. In fact, any shape v which satisfies the fixity condition of both endpoints, i.e., which satisfies the constraint Eq. 4.14, will lead to this situation. The reason is that these displacements are measured from the equilibrium position; and the equilibrium position is at minimum potential energy. Thus, *any* displacement that satisfies the essential boundary conditions (fixities at both ends) must necessarily show no change in potential energy at first order. Near the equilibrium position, every displacement must be accompanied by a locally quadratic rise in potential energy.

Thus, if we use assumed modes that satisfy Eq. 4.19, e.g., if we use the approximate mode shapes determined above as the assumed modes to begin with, then a nonlinear treatment is needed. We now develop the same. A full expansion is tedious, with a large number of terms to handle, so we demonstrate the idea by doing a nonlinear treatment of an expansion close to one of these already-determined modes from Sections 4.3 and 4.4.

[2]The leading order term of λ in Eq. 4.32 cannot be determined. Compare with Eq. 4.20, where substisuting $\boldsymbol{a} = \boldsymbol{0}$ leaves behind $\boldsymbol{p} = \lambda_0\boldsymbol{q}$, and λ_0 can be determined.

4.6 Nonlinear treatment using one mode

In the previous sections we have calculated the mode shapes (to a very good approximation), and have observed that an expansion using the modes themselves, as in Eq. 4.31, satisfies the constraint (Eq. 4.14) up to first order of the a's. We now consider a v which is primarily along a single mode, but with a small correction term that is needed to satisfy the boundary condition upto second order in an appropriate expansion. Using ε as a bookkeeping parameter to keep track of sizes, we write

$$v = \varepsilon\, \alpha(t)\, \psi(x) + \varepsilon^2\, \bar{v}(x,t) \tag{4.33}$$

where $\psi(x)$ is a mode (as obtained above: technically an approximation, but a good one), $\alpha(t)$ is the primary time-varying coordinate associated with $\psi(x)$, and the $\bar{v}(x,t)$ a correction that satisfies the zero boundary conditions of vertical displacement at both endpoints[3]. If we calculate the potential energy $\tilde{\mathcal{V}}$ from Eq. 4.16, there is no direct contribution from the $\psi(x)$ part, as explained above. Hence, the potential energy depends on the second order correction term,

$$\tilde{\mathcal{V}} = m\, g\, \varepsilon^2 \int_0^b \bar{v}\, \sec(\theta(x))\, \mathrm{d}x. \tag{4.34}$$

We now turn to the horizontal displacement constraint, Eq. 4.14, which after integration by parts yields

$$u(b,t) = \int_0^b \left\{ y''(x)\, v - \frac{1}{2}\left(1 + y'(x)^2\right) {v_x}^2 + \cdots \right\} \mathrm{d}x. \tag{4.35}$$

In the above, from Eq. 4.4,

$$y''(x) = \frac{1}{W}\, \sec(\theta(x)),$$

and so (as explained using the potential energy calculation),

$$\int_0^b y''(x)\, \psi(x)\, \mathrm{d}x = 0.$$

[3]Note that the horizontal displacements induced by this choice of v will be required to vanish at both endpoints also.

Therefore, correct up to second order, we have

$$u(b,t) = \varepsilon^2 \int_0^b \left\{ \frac{1}{W} \sec(\theta(x))\, \bar{v} - \frac{1}{2} \left(1 + y'(x)^2\right) \alpha^2 \psi'(x)^2 \right\} \mathrm{d}x = 0. \tag{4.36}$$

The first term in the integrand above is related to the integrand in the expression for the potential energy in Eq. 4.34, and we directly obtain

$$\tilde{\mathcal{V}} = \frac{W\, m\, g\, \varepsilon^2}{2} \int_0^b \left(1 + y'(x)^2\right) \alpha^2 \psi'(x)^2 \, \mathrm{d}x = \mathcal{C}_1 \varepsilon^2 \alpha^2. \tag{4.37}$$

For the kinetic energy to be evaluated correct up to second order, $\bar{v}$ can be dropped from Eq. 4.33. So the function $\bar{v}$ need not be determined at this order, after all, and we have

$$\tilde{\mathcal{T}} = \frac{1}{2} \int_0^b \bar{m} \left(\dot{u}^2 + \dot{v}^2\right) \sec(\theta(x)) \, \mathrm{d}x = \mathcal{C}_2\, \varepsilon^2\, \dot{\alpha}^2. \tag{4.38}$$

Now the Lagrangian

$$\tilde{\mathcal{L}} = \tilde{\mathcal{T}} - \tilde{\mathcal{V}} = \mathcal{C}_2\, \varepsilon^2\, \dot{\alpha}^2 - \mathcal{C}_1\, \varepsilon^2\, \alpha^2, \tag{4.39}$$

yielding

$$\ddot{\alpha} + \tilde{\omega}_1^2\, \alpha = 0, \tag{4.40}$$

where

$$\tilde{\omega}_1 = \sqrt{\frac{\mathcal{C}_1}{\mathcal{C}_2}},$$

which upon evaluating the integrals turns out to be 2.4294 for the symmetric case, matching perfectly (recall section 4.4.1).

4.7 Conclusions

A catenary, or an inextensible chain suspended from two endpoints, has the shape of a hyperbolic cosine at equilibrium. Due to pointwise inextensibility, the vertical and horizontal displacement components are related by a differential equation. An assumed mode solution for small oscillations of a slack catenary presents some challenges and has

been missing from the literature. Here, starting with an assumed mode expansion for the vertical displacement, the horizontal displacement was obtained using the inextensibility condition. The horizontal fixity at the distal end was enforced using an additional scalar constraint. Subsequently, a Lagrangian formulation was used. One of the interesting aspects of this problem is that, in the Lagrangian formulation, the potential energy is *linear* in the generalized coordinates. Enforcement of the constraint through a Lagrange multiplier makes the oscillation frequencies determinate. Further, when these same modes, or any other assumed modes that satisfy the fixity constraint up to first order, are used to expand the vertical displacement, then degeneracy is encountered at first order. However, adding a small perturbation to that assumed mode, and carrying out the calculation to second order, gives the usual harmonic oscillator equation and a fully satisfactory solution.

The method used here is semi-numerical and can be implemented in software like Matlab and Maple. The treatment here helps to provide interesting insights that may carry over to some other problems, such as the vibrations of a pre-bent elastica.

Chapter 5

Small In-plane Oscillations of an Elastica Robot

5.1 Introduction

This is the first of two short chapters on the vibration of pre-bent elasticas. In this chapter we discuss the vibration characteristics of an *elastica robot* [1] which is basically an elastica, fixed at one end, and with a taut inextensible string tied to the other end for actuation. By varying the tension in the string, the tip of the beam can be moved. In the literature, such systems are also called continuum robots, and the string, sometimes, is called a 'tendon' [83]. Elastica robots have applications in cases where the working space is limited and constrained in such a way that using a traditional robot with arms and joints turns out to be inconvenient. That is how the word 'robot'[1] earns a mention in its name.

In the existing literature, a great deal of theoretical work has been carried out on the mechanics of elasticas for centuries. Mathematicians like Jacob Bernoulli, Daniel Bernoulli, and Euler [84] paved the way for modern day researchers. As per Euler's definition [85], an elastica is a large deflection beam that can only have deformation due to bending,

[1]The control aspects have not been studied in this work, so our system could also be called an elastica actuator.

and the curvature at a point is proportional to the locally experienced moment. Love [84] (1944) derived the linearized equations of small curvature elasticas. Motivated by the work of Antman and Kennedy [86] (1981) on large buckling of Kirchhoff rods, Calfisch and Maddocks [87] (1984) presented a nonlinear approach to elastica theory using Lyapunov's technique. Several studies on elasticas have been conducted in the light of Cosserat theory [88, 89]. Several interesting studies [90, 91] on elasticas, bent to form an arch, have been conducted. An elastica arch will be discussed in the next chapter.

Introducing further complexities to the elastica problems, researches have shown interest in cases with constraints. Arreaga and Capovilla [92] studied the stability of the shapes of inextensible elastica loops with constant area and proved the existence of equilibria with self-intersections. Donoël and Detourney [93] studied an elastica inserted in a conduit using an Eulerian approach. During compression, metal sheets often get folded and make contacts with compressing plates. This phenomenon was addressed by Pocheau and Roman [94] who considered a case where an elastica is constrained inside a box and investigated the uniqueness of solutions/shapes obtained. In our work, we consider a pre-bent cantilever elastica beam where the distal end is tied to a taut string, enforcing a displacement constraint on the system.

The string actuated tip-control of an elastica is a well-researched problem. Bayo [95], in 1987, suggested a control approach in which the elastica was modeled using Euler beam theory, and FEA was used to formulate the equation. Catto [96] conducted a detailed study, both numerically and experimentally. He used FEM for studying small lateral vibrations of the elastica robot (called an "elasticarm" in his thesis). One of the interesting findings of his work was that out of plane transverse vibration of the elastica robot does not induce in-plane vibrations. Handral and Rangarajan [1] proposed a mechanics-based tip manipulation approach of a planar nonlinear elastica robot just by varying the string tension.

Finally, coming to applications, elastica robots are popular for their applications in fields

like pipe inspection [97], robot-assisted surgery [98] etc., where high maneuverability is desired in a closed and constrained work space. Armanini et al. [99] analyzed the dynamics of an elastica catapult with a motivation for applying them in building soft robotic limbs. In biomechanics, elastica theory has been used to understand the imbalance between closing and tethering forces on the mitral valve [100]. As was the case with catenary oscillations, an assumed-modes treatment of planar oscillations of a constraint elastica is absent from the literature.

We describe our system in section 5.2, obtain the pre-bent equilibrium solution in section 5.3, introduce the assumed mode expansion in section 5.4, derive the governing equations in sections 5.5 and 5.6, and present our results in 5.7.

5.2 The system

We consider a weightless elastica of length L, flexural rigidity EI, and mass per unit length $\bar{m}$. The beam has one end fixed at point O (see Fig. 5.1), and the other end (point P) is tied to a string of constant length L_s. We set up a coordinate system having its origin at O.

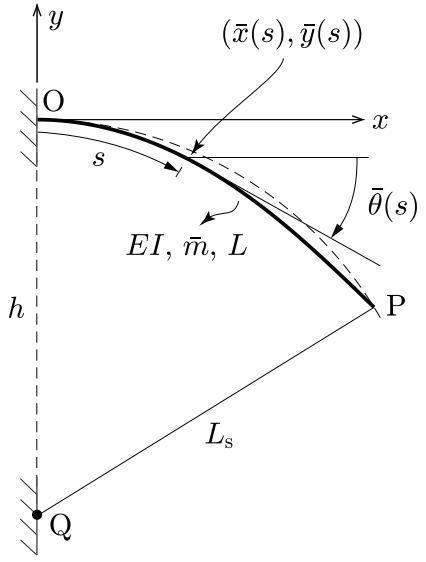

FIGURE 5.1: An elastica robot in a pre-bent configuration.

The other end of the string is attached to a fixed point Q $(0, -h)$. The string is taut and the beam is in a pre-bent configuration. We use the the arclength s as the independent spatial variable. The shape of the beam is determined by its slope angle $\bar{\theta}(s)$. The abscissa and the ordinate of a point on the beam at location s is given by

$$\bar{x}(s) = \int_0^s \cos\bar{\theta}(\xi)\,\mathrm{d}\xi, \quad \text{and} \quad \bar{y}(s) = -\int_0^s \sin\bar{\theta}(\xi)\,\mathrm{d}\xi. \tag{5.1}$$

5.3 The pre-bent equilibrium solution

Initially the beam is in a pre-bent equilibrium state. There is a moment M_O and a force at the fixed end that balance the string tension applied at the distal end. The bending

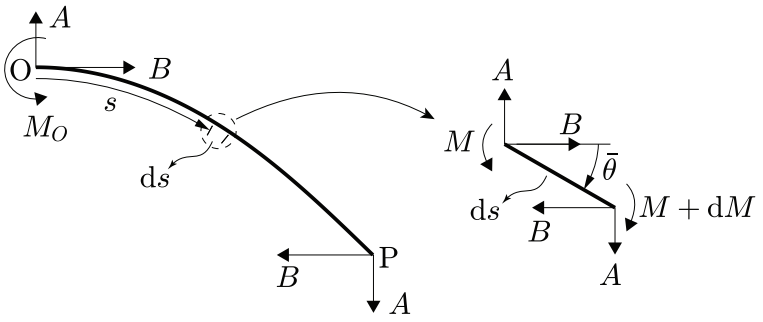

FIGURE 5.2: Free body diagram.

moment at a cross section at s satisfies $M = EI\,\mathrm{d}\bar{\theta}/\mathrm{d}s$. Let the tension of the string have components A and B along $-y$ and $-x$ direction. As the beam is free from any external loading over its length span, there is no change in the force experienced at different cross sections along the length. We write the angular momentum balance equation for an element of infinitesimal length $\mathrm{d}s$ (see Fig. 5.2), which simplifies easily to

$$EI\,\frac{\mathrm{d}^2\bar{\theta}}{\mathrm{d}s^2} = -\left(A\cos\bar{\theta} + B\,\sin\bar{\theta}\right). \tag{5.2}$$

As one end of the beam is fixed at point O,

$$\bar{\theta}(0) = 0 \tag{5.3}$$

is an essential boundary condition. The other end of the beam has no bending moment. Hence

$$\left.\frac{\mathrm{d}\bar{\theta}}{\mathrm{d}s}\right|_{s=L} = 0. \tag{5.4}$$

The point P always maintains a distance L_s from point Q. Hence

$$\bar{x}(L)^2 + (h + \bar{y}(L))^2 = L_\mathrm{s}^2. \tag{5.5}$$

And finally, as the tension on the string is along PQ, we can infer

$$\frac{h + \bar{y}(L)}{\bar{x}(L)} = \frac{A}{B}. \tag{5.6}$$

In order to solve Eq. 5.2, we must know the initial condition $\left.\frac{\mathrm{d}\bar{\theta}}{\mathrm{d}s}\right|_{s=0}$, and the string tension components A and B. So we adjust these three quantities such that the three constraints (Eq. 5.4, 5.5, and 5.6) are satisfied. This is a routine numerical calculation and a minor variant of a two-point boundary value problem.

5.4 Assumed mode expansion

For small oscillations of the pre-bent elastica robot we consider small perturbations added to the equilibrium solution obtained in section 5.3 and define

$$\theta(s,t) = \bar{\theta}(s) + \sum_{k=1}^{N} a_k(t)\,\phi_k(s) = \bar{\theta}(s) + \Phi\,\boldsymbol{a} \tag{5.7}$$

where the ϕ's are assumed modes satisfying the essential boundary condition, i.e., $\phi_k(0) = 0,\ \forall k \in \{1, 2, \cdots, N\}$, and the a's are generalized coordinates. The matrix $\Phi = [\phi_1(s), \phi_2(s), \cdots, \phi_N(s)]$, and the vector $\boldsymbol{a} = [a_1(t), a_2(t), \cdots, a_N(t)]^\top$, allow compact notation. The abscissa and

ordinate of a point on the beam at arclength s in the perturbed configuration are given by

$$\begin{aligned} x(s,t) = &\int_0^s \cos\theta(\xi,t)\,\mathrm{d}\xi = \int_0^s \cos\left(\bar{\theta}(\xi) + \sum_{k=1}^{N} a_k(t)\,\phi_k(\xi)\right)\mathrm{d}\xi \\ =&\bar{x}(s) - \sum_{k=1}^{N} a_k(t) \int_0^s \sin\bar{\theta}(\xi)\,\phi_k(\xi)\,\mathrm{d}\xi \\ &- \frac{1}{2}\sum_{k=1}^{N}\sum_{j=1}^{N} a_k(t)\,a_j(t) \int_0^s \cos\bar{\theta}\,(\xi)\phi_k(\xi)\,\phi_j(\xi)\,\mathrm{d}\xi + \mathcal{O}\left(||\boldsymbol{a}||^3\right). \end{aligned} \tag{5.8}$$

and

$$\begin{aligned} y(s,t) = &-\int_0^s \sin\theta(\xi,t)\,\mathrm{d}\xi = -\int_0^s \sin\left(\bar{\theta}(\xi) + \sum_{k=1}^{N} a_k(t)\,\phi_k(\xi)\right)\mathrm{d}\xi \\ =&\bar{y}(s) - \sum_{k=1}^{N} a_k(t) \int_0^s \cos\bar{\theta}(\xi)\,\phi_k(\xi)\,\mathrm{d}\xi \\ &+ \frac{1}{2}\sum_{k=1}^{N}\sum_{j=1}^{N} a_k(t)\,a_j(t) \int_0^s \sin\bar{\theta}\,(\xi)\phi_k(\xi)\,\phi_j(\xi)\,\mathrm{d}\xi + \mathcal{O}\left(||\boldsymbol{a}||^3\right). \end{aligned} \tag{5.9}$$

5.5 Lagrangian formulation with constraints

The kinetic and potential energy of the system are given by

$$\mathcal{T} = \frac{1}{2}\int_0^L \bar{m}\left\{\left(\frac{\partial x}{\partial t}\right)^2 + \left(\frac{\partial y}{\partial t}\right)^2\right\}\mathrm{d}s, \quad \text{and} \quad \mathcal{V} = \frac{1}{2}\int_0^L EI\left(\frac{\partial\theta}{\partial s}\right)^2\mathrm{d}s. \tag{5.10}$$

and the Lagrangian

$$\mathcal{L} = \mathcal{T} - \mathcal{V}. \tag{5.11}$$

Gravity is not included. During small oscillations, the string always remains taut, and the point P always maintains a distance L_s from the point Q, which imposes the constraint

$$\mathcal{G}\left(\boldsymbol{a}\right) = x(L,t)^2 + \left(h + y(L,t)\right)^2 - L_\mathrm{s}^2 = 0 \tag{5.12}$$

on the system. The Euler-Lagrange equation is

$$\frac{\mathrm{d}}{\mathrm{d}t}\left(\frac{\partial \mathcal{L}}{\partial \dot{\boldsymbol{a}}}\right) - \frac{\partial \mathcal{L}}{\partial \boldsymbol{a}} = \lambda \frac{\partial \mathcal{G}}{\partial \boldsymbol{a}}, \tag{5.13}$$

where λ is the unknown multiplier.

5.6 Equations of motion

Linearization of Eq. 5.13 yields

$$\mathbf{M}\,\ddot{\boldsymbol{a}} + \mathbf{K}\,\boldsymbol{a} + \boldsymbol{p} = \lambda\,\boldsymbol{q} + \lambda\,\mathbf{N}\,\boldsymbol{a} \tag{5.14}$$

where $\mathbf{M}$, $\mathbf{K}$, and $\mathbf{N}$ are known symmetric matrices, the vectors $\boldsymbol{p}$ and $\boldsymbol{q}$ are parallel, and λ is an unknown multiplier. We recall that the equilibrium ($\boldsymbol{a} = \mathbf{0}$) is a solution to Eq. 5.14. Say for $\boldsymbol{a} = \mathbf{0}$, $\lambda = \lambda_0$. Hence

$$\boldsymbol{p} = \lambda_0\,\boldsymbol{q}. \tag{5.15}$$

As the vectors $\boldsymbol{p}$ and $\boldsymbol{q}$ are parallel, λ_0 is uniquely determined from Eq. 5.15. For small $\boldsymbol{a}$, λ has a small deviation from λ_0. So, substituting $\lambda = \lambda_0 + \eta$ in Eq. 5.14, and retaining only the leading order terms yield

$$\mathbf{M}\,\ddot{\boldsymbol{a}} + \mathbf{K}\,\boldsymbol{a} = \eta\,\boldsymbol{q} + \lambda_0\,\mathbf{N}\,\boldsymbol{a}, \tag{5.16}$$

where $||\boldsymbol{a}||$ and η have the same order of magnitude. As the RHS of Eq. 5.14 originates from the gradient of Eq. 5.12 we can write

$$\mathcal{G}(\boldsymbol{a}) = \boldsymbol{a}^\top \boldsymbol{q} + \frac{1}{2}\,\boldsymbol{a}^\top \mathbf{N}\,\boldsymbol{a} + \mathcal{O}\left(||\boldsymbol{a}||^3\right) = 0. \tag{5.17}$$

In order to satisfy the constraint (Eq. 5.17) to the leading order, $\boldsymbol{a}$ must lie in the $(N-1)$ dimensional vector space $\mathcal{X}$ which is orthogonal to $\boldsymbol{q}$. Hence we can write

$$\boldsymbol{a} = \mathbf{Q}\,\boldsymbol{\zeta}, \tag{5.18}$$

where the matrix $\mathbf{Q}$ contains the basis for $\mathcal{X}$, and vector $\boldsymbol{\zeta}$ has the coordinates in the new basis. Substituting Eq. 5.18 in Eq. 5.16, premultiplying with $\mathbf{Q}$, we obtain

$$\tilde{\mathbf{M}}\,\ddot{\boldsymbol{\zeta}} + \tilde{\mathbf{K}}\,\boldsymbol{\zeta} = \lambda_0\,\tilde{\mathbf{N}}\,\boldsymbol{\zeta}, \tag{5.19}$$

where $\tilde{\mathbf{M}} = \mathbf{Q}^\top\mathbf{M}\,\mathbf{Q}$, $\tilde{\mathbf{K}} = \mathbf{Q}^\top\mathbf{K}\,\mathbf{Q}$, and $\tilde{\mathbf{N}} = \mathbf{Q}^\top\mathbf{N}\,\mathbf{Q}$. The mode shapes and the frequencies can be calculated from Eq. 5.19.

The finally obtained equation (Eq. 5.19) yields an eigenvalue problem which can be solved for $\boldsymbol{\zeta}$. Subsequently, $N-1$ physical mode shape can be found from Eq. 5.18.

5.7 Results

With suitable choice of units we take $EI = 1$ and $\bar{m} = 1$, and we choose $L = 1$, $h = 1$, and $L_\mathrm{s} = 1$. We use two sets of basis functions or assumed modes that satisfy the essential boundary condition.

$$(1) : \phi_k(s) = \sin\left(\frac{(2\,k-1)\pi s}{2\,L}\right) \quad \text{and} \quad (2) : \phi_k(s) = \left(\frac{s}{L}\right)^k, \quad k = 1, 2, \cdots, N. \tag{5.20}$$

The first five natural frequencies obtain using these sets of assumed modes are given in table 5.1. The fist set of basis functions, apart from satisfying the essential boundary

TABLE 5.1: Frequencies (in $\mathrm{rad\,s^{-1}}$) for two sets of basis functions.

	(1)	(2)
ω_1	13.55	13.53
ω_2	47.29	47.11
ω_3	100.91	102.71
ω_4	177.47	189.07
ω_5	274.01	637.43

condition, meet the condition of zero bending moment on the distal end of the elastica and are expected to yield more accurate results than the polynomials of the second set of basis functions. The line ST in Fig. 5.3 is the tangent at point P on the circular arc centered at Q with radius L_s. While calculating the mode shapes we integrate Eqs. 5.8 and

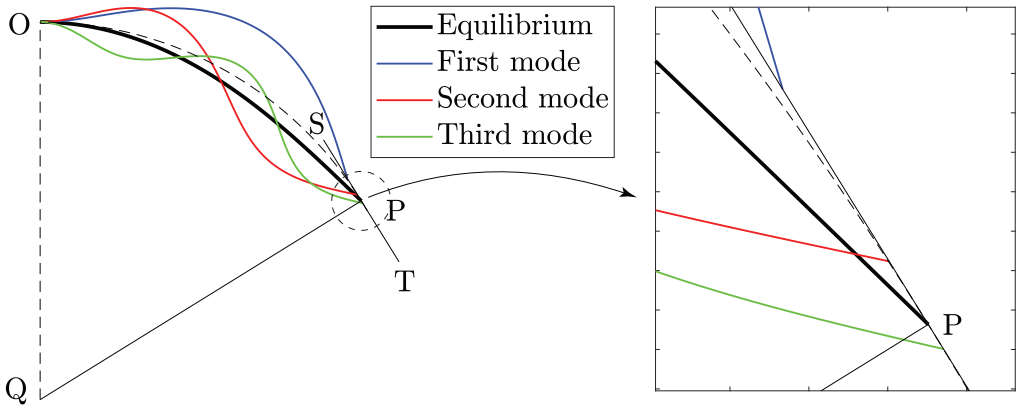

FIGURE 5.3: The first three mode shapes and a magnified view of the region near point P. The dashed line in the magnified view is a portion of the circular arc OP and the solid line ST is a tangent to that arc at point P.

5.9 considering only terms linear in the a's. For this reason the mode shapes terminate on the tangent line.

5.8 Conclusions

An elastica robot consists of an elastica, fixed at one end, with a taut and inextensible string tied to the other end for actuation. We study small planar oscillatory motions of the elastica robot near such a pre-bent configuration. We use an assumed mode expansion for small motions of the beam near the equilibrium. Using the Lagrangian approach, equations are derived where the contributions of the distal end constraint appear with an unknown multiplier. Using the fact that the equilibrium satisfies the equations of motions, we can compute the leading order term of the multiplier, which allows subsequent solution via an eigenvalue problem.

While the elastica has bending rigidity and the catenary does not, the elastica robot has been formulated with a scalar constraint at its distal end, and so the formulation has similarities with that of the catenary.

In the next chapter we study a different elastica problem that involves two scalar constraints, requiring slightly different treatment.

Chapter 6

Small In-plane Oscillations of an Elastica Arch

6.1 Introduction

Slender structures bent to form arch shapes are frequently used in various applications for their load-bearing ability. These structural members, already in a pre-stressed configuration, are susceptible to oscillations. In this chapter, we study the small motions of an elastica arch about its pre-bent equilibrium. Gravity is included.

Love [84] (1944) presented an analysis for shallow elastica arches in the linear regime. As an extension of that, the dynamic stability of a shallow elastica arch under impulsive loading was studied by Hsu [90] (1967). Several studies [101, 102, 103] have been conducted on buckling, post-buckling, and large deformations of heavy elasticas due to self-weight. Perkins [91] (1990) analytically studied the linear planar vibrations of a pre-bent extensible elastica arch, pinned at both end, and subjected to a steady end load. The governing PDEs were derived using the Hamiltonian approach, and variable-separable trial solutions like '$U(s)\exp(\mathrm{i}\,\omega t)$' were used to find the eigenfunctions where s is the arclength coordinate. Experimental validation of theoretically obtained results was also provided by the author. It was experimentally shown by Pippard [104] that a centrally loaded elastica can

lose stability by a symmetric plunging or an asymmetric displacement in the sideways. Following the work of Pippard, the small motions of a centrally loaded elastica arch was studied by Patrício et al. [105] (1998). In this paper, the authors used the Lagrangian formulation with two end fixity constraints, and followed the continuum approach. The PDEs were solved using variable separable functions similar to [91]. In our work, despite using the Lagrangian approach with two distal end fixity constraints, we discretize in advance using an inextensible assumed-modes expansion for small motions near the pre-bent equilibrium, which yields a set of ODEs to work with, and find the Lagrange multipliers to the leading order by using the fact that the equilibrium is a solution to the obtained set of equations.

6.2 The system

We consider an elastica of length L in a pre-bent arch configuration and pinned at the ends O and Q. The flexural rigidity of the beam is EI, and it has a uniform mass per unit length $\bar{m}$. We set up a coordinate system with the origin at O. The coordinate of the point Q is (b, h) where we can consider $b > 0$ and $h > 0$ without loss of generality. Gravity acts along the negative y direction. For our analysis, we use the arc length $s \in [0, L]$ as the independent variable. For an equilibrium configuration (see Fig. 6.1), the slope angle at a point at an arc length s is given by $\bar{\theta}(s)$.

The abscissa and the ordinate of a point at an arc length s in the equilibrium configuration are given by

$$\bar{x}(s) = \int_0^s \cos\bar{\theta}(\xi)\,\mathrm{d}\xi, \quad \bar{y}(s) = \int_0^s \sin\bar{\theta}(\xi)\,\mathrm{d}\xi. \tag{6.1}$$

The bending moment at a section is given by $M = EI\,\mathrm{d}\bar{\theta}/\mathrm{d}s$. As the ends are pinned, the bending moment there is zero.

We consider a small element of length $\mathrm{d}s$ and write the linear and angular momentum balance equations for that.

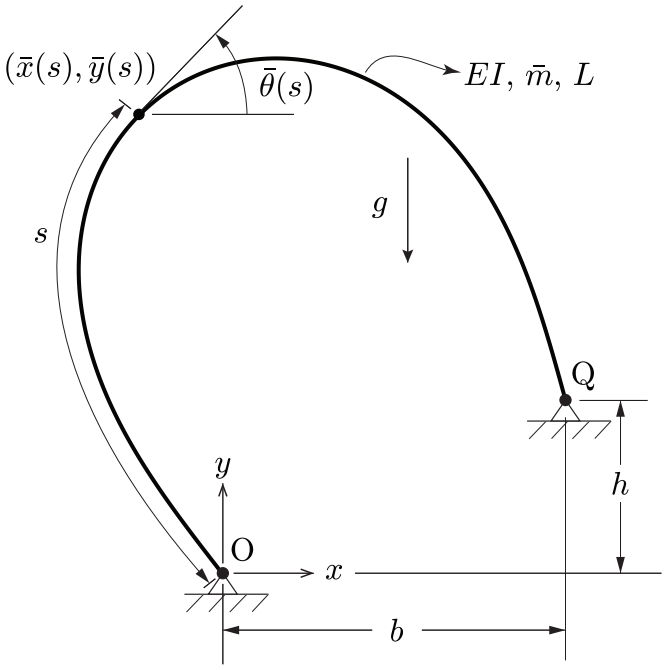

FIGURE 6.1: A pre-bent elastica arch pinned at both ends.

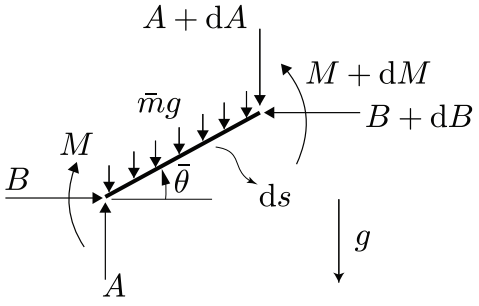

FIGURE 6.2: The free body diagram of a small element of length $\mathrm{d}s$.

The linear momentum balance equations (along x and y direction) yield (at equilibrium)

$$\frac{\mathrm{d}B}{\mathrm{d}s} = 0, \quad \frac{\mathrm{d}A}{\mathrm{d}s} = -\bar{m}\, g$$

whence B is a constant, and $A(s) = A_0 - \bar{m}\, g\, s$ where A_0 is a constant. The angular momentum balance equation yields

$$EI\, \frac{\mathrm{d}^2\bar{\theta}}{\mathrm{d}s^2} = (A_0 - \bar{m}\, g\, s)\, \cos\bar{\theta} - B\, \sin\bar{\theta}. \tag{6.2}$$

We consider Eq. 6.2 as an initial value problem although $\bar{\theta}(0)$ and the constants A_0, B are

not known yet. Regarding the boundary condition, we say that both the end experience zero bending moment as they are pinned, and the coordinate of the end point of the arch is (b, h) which can be mathematically expressed by

$$\left.\frac{\mathrm{d}\bar{\theta}}{\mathrm{d}s}\right|_{s=L0} = 0, \quad \left.\frac{\mathrm{d}\bar{\theta}}{\mathrm{d}s}\right|_{s=L} = 0, \quad \bar{x}(L) = b, \quad \bar{y}(L) = h.$$

Hence we adjust the values of $\bar{\theta}(0)$, A_0, and B in such a way that the boundary conditions at the distal end are satisfied.

We solve Eq. 6.2 and obtain the equilibrium shape $\bar{\theta}(s)$ for the arch. We now proceed towards studying small oscillations about the obtained equilibrium.

As noted above, in [105] the oscillatory solutions were studied without the simplifying a priori assumed-modes discretization used here.

6.3 Small oscillations about equilibrium

We consider small planar perturbations about the pre-bent equilibrium of the arch in terms of a set of assumed basis functions

$$\theta(s,t) = \bar{\theta}(s) + \sum_{k=1}^{N} a_k(t)\,\phi_k(s) = \bar{\theta}(s) + \Phi\,\boldsymbol{a}, \tag{6.3}$$

where the ϕ's are assumed modes and the a's are generalized coordinates associated with them. As Eq. 6.2 is not constrained by any essential boundary condition, the choice of ϕ_k, $k \in \{1, 2, \cdots, N\}$, in this case, can be arbitrary. The matrix $\Phi = [\phi_1, \phi_2, \cdots, \phi_N]$ and the vector $\boldsymbol{a} = [a_1, a_2, \cdots, a_N]^\top$ are introduced for compact notation. The abscissa and ordinate of a point in the perturbed configuration are given by (similar to the preceding

chapter)

$$\begin{aligned} x(s,t) &= \int_0^s \cos\left(\bar{\theta}(\xi) + \sum_{k=1}^{k=N} a_k(t)\,\phi_k(\xi)\right) \mathrm{d}\xi \\ &= \bar{x}(s) - \sum_{k=1}^{N} a_k \int_0^s \sin\bar{\theta}\,\phi_k \;\mathrm{d}\xi - \frac{1}{2}\sum_{k=1}^{N}\sum_{j=1}^{N} a_k\,a_j \int_0^s \cos\bar{\theta}\,\phi_k\,\phi_j \;\mathrm{d}\xi + \mathcal{O}\left(||\boldsymbol{a}||^3\right), \end{aligned} \tag{6.4}$$

and

$$\begin{aligned} y(s,t) &= \int_0^s \sin\left(\bar{\theta}(\xi) + \sum_{k=1}^{k=N} a_k(t)\,\phi_k(\xi)\right) \mathrm{d}\xi \\ &= \bar{y}(s) + \sum_{k=1}^{N} a_k \int_0^s \cos\bar{\theta}\,\phi_k \;\mathrm{d}\xi - \frac{1}{2}\sum_{k=1}^{N}\sum_{j=1}^{N} a_k\,a_j \int_0^s \sin\bar{\theta}\,\phi_k\,\phi_j \;\mathrm{d}\xi + \mathcal{O}\left(||\boldsymbol{a}||^3\right). \end{aligned} \tag{6.5}$$

6.4 Lagrangian formulation

The kinetic and potential energy of the system are given by

$$\mathcal{T} = \frac{1}{2}\int_0^L \bar{m}\,\left(\dot{x}(s,t)^2 + \dot{y}(s,t)^2\right)\,\mathrm{d}s, \;\text{ and }\; \mathcal{V} = \frac{1}{2}\int_0^L EI\,\left(\frac{\partial\theta}{\partial s}\right)^2 \mathrm{d}s + \bar{m}\,g\int_0^L y(s,t)\;\mathrm{d}s, \tag{6.6}$$

where the overdot stands for a derivative with respect to time. The Lagrangian

$$\mathcal{L} = \mathcal{T} - \mathcal{V}. \tag{6.7}$$

The system is subjected to the scalar constraints

$$\mathcal{G}_1(\boldsymbol{a}) = x(L,t) - b = 0, \;\text{ and }\; \mathcal{G}_2(\boldsymbol{a}) = y(L,t) - h = 0. \tag{6.8}$$

The Euler-Lagrange equation is

$$\frac{\mathrm{d}}{\mathrm{d}t}\left(\frac{\partial\mathcal{L}}{\partial\dot{\boldsymbol{a}}}\right) - \frac{\partial\mathcal{L}}{\partial\boldsymbol{a}} = \lambda_1\,\frac{\partial\mathcal{G}_1}{\partial\boldsymbol{a}} + \lambda_2\,\frac{\partial\mathcal{G}_2}{\partial\boldsymbol{a}}, \tag{6.9}$$

where λ_1 and λ_2 are unknown multipliers.

6.5 Equations of motion

Linearizing Eq. 6.9, we obtain

$$\mathbf{M}\,\ddot{\boldsymbol{a}} + \mathbf{P}\,\boldsymbol{a} + \boldsymbol{p} = \lambda_1\,\boldsymbol{q}_1 + \lambda_1\,\mathbf{B}_1\,\boldsymbol{a} + \lambda_2\,\boldsymbol{q}_2 + \lambda_2\,\mathbf{B}_2\,\boldsymbol{a}, \tag{6.10}$$

where $\mathbf{M}$, $\mathbf{P}$, $\mathbf{B}_1$, and $\mathbf{B}_2$ are symmetric matrices of size N, and the vectors $\boldsymbol{p}$, $\boldsymbol{q}_1$, $\boldsymbol{q}_2 \in \mathbb{R}^N$. As the system is perturbed from the equilibrium configuration, zero displacement or $\boldsymbol{a} = \mathbf{0}$ must be a solution to the equation of motion (Eq. 6.10). Consequently, the static part of the equation, evaluated at equilibrium, must vanish. Thus, we expect $\lambda_1 = \lambda_{10}$, and $\lambda_2 = \lambda_{20}$ when $\boldsymbol{a} = \mathbf{0}$. Then we obtain

$$\boldsymbol{p} = \lambda_{10}\,\boldsymbol{q}_1 + \lambda_{20}\,\boldsymbol{q}_2. \tag{6.11}$$

For $N > 2$, Eq. 6.11 appears overdetermined. It has exact and unique solutions for λ_{10} and λ_{20} if and only if the vector $\boldsymbol{p}$ is a linear combination of $\boldsymbol{q}_1$ and $\boldsymbol{q}_2$. Indeed it is numerically found that

$$\boldsymbol{p} \in \text{span}\{\boldsymbol{q}_1, \boldsymbol{q}_2\},$$

and unique λ_{10} and λ_{20} exist that satisfy Eq. 6.11.

For small $\boldsymbol{a}$, let us assume λ_1 and λ_2 to have small perturbations from their respective values at equilibrium, i.e.,

$$\lambda_1 = \lambda_{10} + \eta_1, \quad \text{and} \quad \lambda_2 = \lambda_{20} + \eta_2 \tag{6.12}$$

where η_1, η_2, and $||\boldsymbol{a}||$ have the same order of magnitude. Substituting Eq. 6.12 in Eq. 6.10 and neglecting the higher order terms, we obtain

$$\mathbf{M}\,\ddot{\boldsymbol{a}} + \mathbf{P}\,\boldsymbol{a} = \eta_1\,\boldsymbol{q}_1 + \eta_2\,\boldsymbol{q}_2 + \lambda_{10}\,\mathbf{B}_1\,\boldsymbol{a} + \lambda_{20}\,\mathbf{B}_2\,\boldsymbol{a}, \tag{6.13}$$

in which η_1 and η_2 remain undetermined. The indeterminacy can be removed by looking for a solution, consistent with the constraints, in an appropriate subspace of $\mathbb{R}^N$.

The coefficients of λ_1 and λ_2 in Eq. 6.10 are the gradients of the constraints $\mathcal{G}_1$ and $\mathcal{G}_2$ (Eq. 6.8) respectively with respect to $\boldsymbol{a}$. Hence, we can rewrite the them up to second order as

$$\mathcal{G}_1(\boldsymbol{a}) = \boldsymbol{a}^\top \boldsymbol{q}_1 + \boldsymbol{a}^\top \mathbf{B}_1 \, \boldsymbol{a} = 0 \;\text{ and }\; \mathcal{G}_2(\boldsymbol{a}) = \boldsymbol{a}^\top \boldsymbol{q}_2 + \boldsymbol{a}^\top \mathbf{B}_2 \, \boldsymbol{a} = 0. \tag{6.14}$$

In order to satisfy Eq. 6.14 up to first order, $\boldsymbol{a}$ must be orthogonal to both the vectors $\boldsymbol{q}_1$ and $\boldsymbol{q}_2$. Thus, $\boldsymbol{a}$ must lie in an $N-2$ dimensional vector space $\mathcal{X}$ such that for any $\boldsymbol{v} \in \mathcal{X}$, $\boldsymbol{v}^\top \boldsymbol{q}_1 = \boldsymbol{v}^\top \boldsymbol{q}_2 = 0$. Consequently, we can expand

$$\boldsymbol{a}(t) = \mathbf{R} \, \boldsymbol{\zeta}(t), \quad \mathbf{R} \in \mathbb{R}^{N \times (N-2)}, \tag{6.15}$$

where $\mathbf{R}$ contains $N-2$ basis vectors[1] of $\mathcal{X}$ and the vector $\boldsymbol{\zeta}$ contains new generalized coordinates. Substituting Eq. 6.15 in Eq. 6.13 and pre-multiplying $\mathbf{R}^\top$ on both sides yields

$$\tilde{\mathbf{M}} \, \ddot{\boldsymbol{\zeta}} + \tilde{\mathbf{P}} \, \boldsymbol{\zeta} = \lambda_{10} \, \tilde{\mathbf{B}}_1 \, \boldsymbol{\zeta} + \lambda_{20} \, \tilde{\mathbf{B}}_2 \, \boldsymbol{\zeta} \tag{6.16}$$

where

$$\tilde{\mathbf{M}} = \mathbf{R}^\top \mathbf{M} \, \mathbf{R}, \quad \tilde{\mathbf{P}} = \mathbf{R}^\top \mathbf{P} \, \mathbf{R}, \quad \tilde{\mathbf{B}}_1 = \mathbf{R}^\top \mathbf{B}_1 \, \mathbf{R}, \;\text{ and }\; \tilde{\mathbf{B}}_2 = \mathbf{R}^\top \mathbf{B}_2 \, \mathbf{R}.$$

The finally obtained equation (Eq. 6.16) yields an eigenvalue problem which can be solved for $\boldsymbol{\zeta}$. Subsequently, $N-2$ physical mode shapes can be obtained from Eq. 6.15.

6.6 Results

Using nondimensionalization or with suitable choice of units we can take $L = 1$, $\bar{m} = 1$, and $EI = 1$. We choose $b = 0.3$ and $h = 0.15$ to have an arch-shaped pre-bent initial

[1] MATLAB command `qr`($[\boldsymbol{q}_1, \boldsymbol{q}_2]$) can be used to find a basis to expand $\boldsymbol{a}$.

configuration. The acceleration due to gravity, g, is now understood to be nondimensional and can in principle take arbitrary positive values depending on the actual physical parameters of the elastica.

As the system is not constrained with further essential boundary conditions, we are allowed to choose any arbitrary basis for the oscillatory displacements. We select the Legendre polynomials as the assumed modes, and use an expansion for $\theta(s,t)$ (Eq. 6.3) with $N = 6$. Disregarding the effects of gravity the first three natural frequency obtained are 13.458, 64.739, and 244.996 radian per unit time (nondimensional). The first three mode shapes of small oscillations have been shown in Fig. 6.3.

For investigating the effect of moderate gravity, we do not consider buckling as studied in [105]. We note that for higher nondimensional g, the equilibrium shape of the arch gets more flattened. We calculate the frequencies and mode shapes for $g = 20$. The first three obtained frequencies are 10.788, 62.348, and 239.372 radian per unit time. The first three mode shapes of small oscillations under the influence of gravity have been shown in Fig. 6.4.

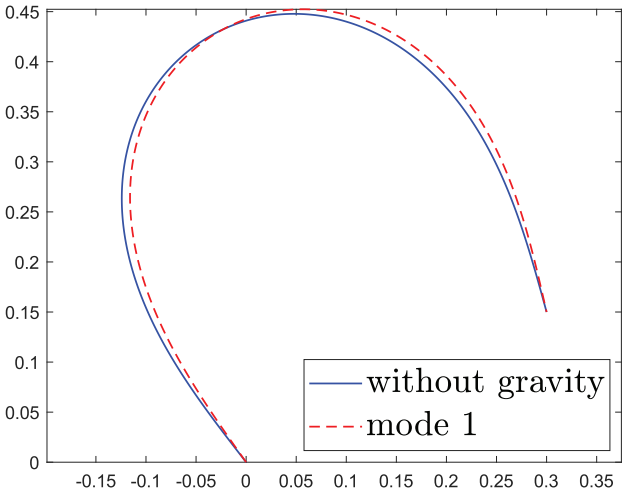

(a) First mode

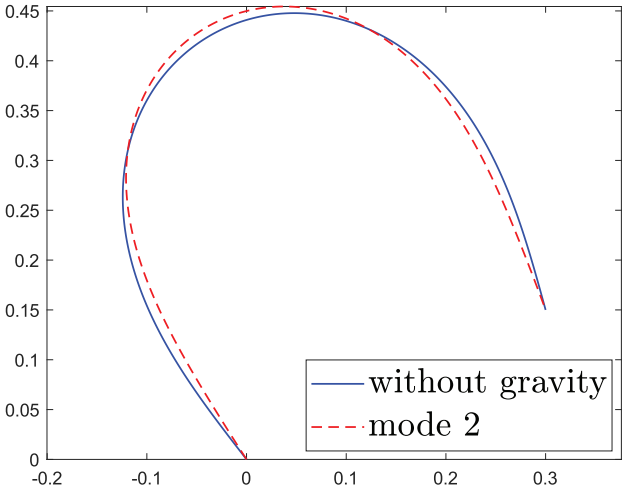

(b) Second mode

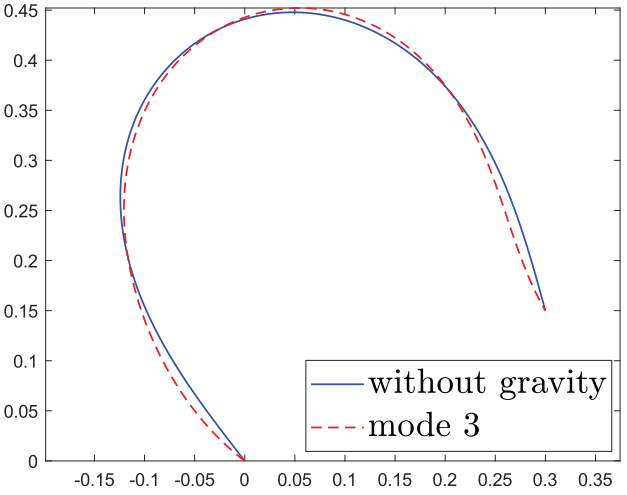

(c) Third mode

FIGURE 6.3: First three mode shapes when gravity is not considered. The black lines show the equilibrium configuration and the red dashed lines show the mode shapes of small oscillation of the elastica arch near the equilibrium.

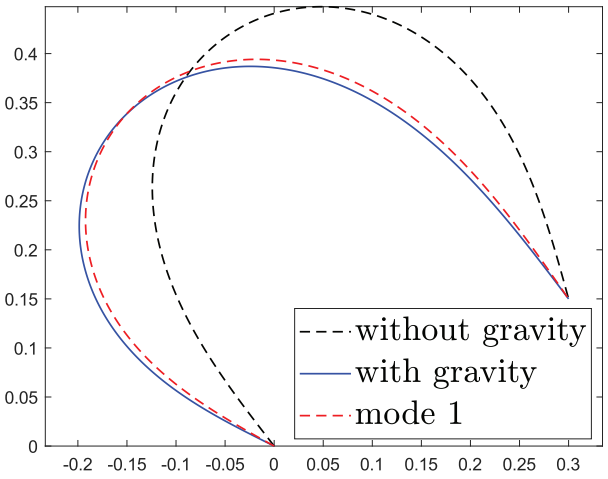

(a) First mode

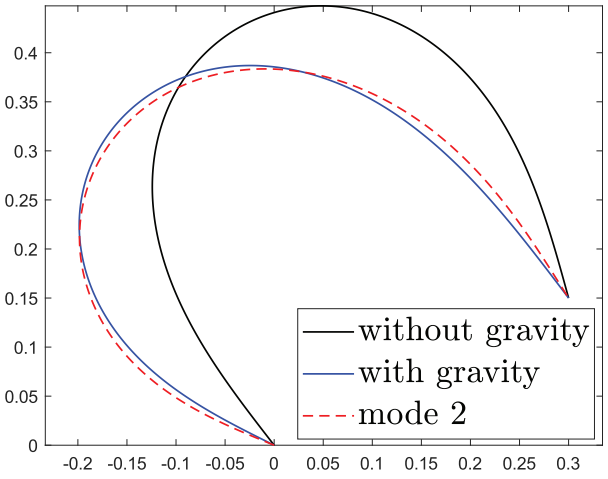

(b) Second mode

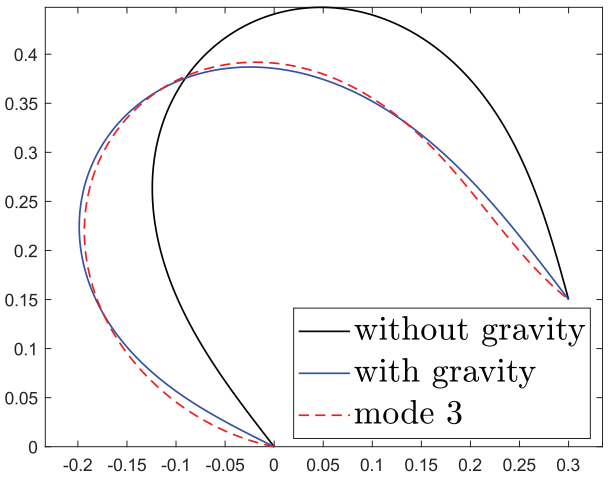

(c) Third mode

FIGURE 6.4: First three mode shapes under the influence of gravity. The black dashed lines show the equilibrium when gravity is not considered. The blue lines show the equilibrium under the influence of gravity. The red dashed lines are the mode shapes of small oscillation of the elastica arch near the equilibrium influenced by gravity.

6.7 Conclusions

We have presented a semi-numerical method for obtaining natural frequencies and mode shapes of small, in plane oscillations of a pre-bent elastica arch. In particular, as also in the previous two chapters, we have used the assumed modes method to obtain eigenvalue problems of small size. We began with finding the equilibrium shape of the beam, and then considered small, in plane perturbations about it in terms of assumed modes. We then used the Lagrangian approach with two scalar constraint equations, unlike in the previous two chapters.

Chapter 7

Concluding Remarks

This thesis delineates solution approaches to five loosely related problems in slender structures addressing applications like the modeling of nonanalytic and nonsmooth damping in structures, model order reduction for such systems with large numbers of state variables, the short-time angular impulse response of Rayleigh beams, and small oscillations of structures subjected to end constraints. For such problems, the existing theoretical framework has its limitations. This thesis presents some unconventional approximate methods that offer reasonably good results and satisfying insights as well. The first problem (Chapter 2) offers a time integration algorithm and a model order reduction technique. The second problem (Chapter 3) contributes a unique asymptotic approximation technique. The third, fourth, and fifth problems (Chapters 4, 5, and 6) have similarity in terms of the solution approach. These problems exploit the assumed-modes method to determine the vibration characteristics of constrained slender structures, and also offer useful insights on the role of constraints in Lagrangian mechanics.

In the study on integrating structures with nonsmooth hysteresis (given in Chapter 1), there are two contributions. First of all, acknowledging the merit of Piché's [32] time integration algorithm, which should be more popular for its outstanding ability to remove numerical instabilities due to higher modes in the structure, we provide a nontrivial modification of it for integrating nonsmooth systems relevant to hysteretic damping. More

generally, referring this part of the work, similar extensions of Piché 's algorithm can be contemplated for systems where apart from the dynamic equations there are first order rate equations that govern the system (e.g., structures with thermoelastic damping [106]). As the second contribution of this work, we propose a model order reduction technique. The modal projection method has been historically effective in substantially reducing the number of dynamic variables (displacements and velocities). We propose a technique which, along with modal reduction, reduces the number of additional state variables (hysteretic variables in our case) using an initial set of simulation data.

The study on the short-time behaviour of slender beams (Chapter 3) subject to angular impulse has somewhat counter intuitive findings. The traditional methods of modal expansion and dimensional analysis lead us to an anharmonic sine series as the obtained response. The functional value of the series at $t = 0$ is 0, and at the same point of time there is a finite jump discontinuity. We introduce an asymptotic expansion (valid for a small times) which breaks the series into two parts (consisting of terms in sequence) and treats them differently. The place where the series is broken, depends on the smallness of the time duration being considered, but in the end it drops out of the results which depends only on the time.

For the last three problems, i.e., the slack catenary, the elastica robot, and the elastica arch (Chapters 4, 5, and 6), the solution approaches are similar. The last of these three problems differs in the number of scalar end-fixity constraints. We have used the Lagrangian formulation with constraints, and have utilized assumed-modes to discretize the system in order to obtain governing ODEs. These problems offer insights into both assumed-modes approximations as well as constraints in Lagrangian Mechanics.

Appendix A

Finite element formulation details

Starting with

$$\hat{u}_{(\mathrm{e})} = \sum_{k=1}^{4} \psi_{(\mathrm{e})k}(x) q_{(\mathrm{e})k}(t), \tag{A.1}$$

recalling Eqs. (2.2, 2.6) and performing the integrals over an element, we obtain

$$\mathbf{M}_{(\mathrm{e})}\ddot{\boldsymbol{q}}_{(\mathrm{e})} + \mathbf{K}_{(\mathrm{e})}\boldsymbol{q}_{(\mathrm{e})} + \boldsymbol{Q}_{(\mathrm{e})} = \mathbf{0}, \tag{A.2}$$

where $M_{(\mathrm{e})ij} = \int_0^{h_\mathrm{e}} \rho A \psi_{(\mathrm{e})i}(x)\psi_{(\mathrm{e})j}(x)\,\mathrm{d}x$, $K_{(\mathrm{e})ij} = \int_0^{h_\mathrm{e}} EI\psi''_{(\mathrm{e})i}(x)\psi''_{(\mathrm{e})j}(x)\,\mathrm{d}x$. The generalised force corresponding to the coordinate $q_{(\mathrm{e})i}(t)$ is given by

$$Q_{(\mathrm{e})i} = \gamma_\mathrm{h} \int_0^{h_\mathrm{e}} z_{(\mathrm{e})}(x,t)\psi''_{(\mathrm{e})i}(x)\,\mathrm{d}x.$$

Letting $x = \frac{h_\mathrm{e}}{2}(1+\zeta)$,

$$\begin{aligned} Q_{(\mathrm{e})_i} &= \frac{\gamma_\mathrm{h} h_\mathrm{e}}{2} \int_{-1}^{1} z_{(\mathrm{e})} \left(h_\mathrm{e} \frac{1+\zeta}{2}, t \right) \psi''_{(\mathrm{e})_i} \left(h_\mathrm{e} \frac{1+\zeta}{2} \right) \mathrm{d}\zeta \\ &= \frac{\gamma_\mathrm{h} h_\mathrm{e}}{2} \int_{-1}^{1} \overline{z}_{(\mathrm{e})}(\zeta, t) \overline{\psi}''_{(\mathrm{e})_i}(\zeta)\, \mathrm{d}\zeta \\ &= \frac{\gamma_\mathrm{h} h_\mathrm{e}}{2} \sum_{p=1}^{n_\mathrm{g}} w_p\, \overline{z}_{(\mathrm{e})}(\zeta_p, t)\, \overline{\psi}''_{(\mathrm{e})_i}(\zeta_p) \text{ (Gauss quadrature)} \\ &= \frac{\gamma_\mathrm{h} h_\mathrm{e}}{2} \sum_{p=1}^{n_\mathrm{g}} \overline{\psi}''_{(\mathrm{e})_i}(\zeta_p)\ \overline{z}_{(\mathrm{e})_p}\, w_p \end{aligned} \tag{A.3}$$

where $\overline{z}_{(\mathrm{e})}(\zeta, t) = z_{(\mathrm{e})}\left(h_\mathrm{e} \frac{1+\zeta}{2}, t \right)$, $\overline{z}_{(\mathrm{e})_p} = \overline{z}_{(\mathrm{e})}(\zeta_p, t)$, $\overline{\psi}''_{(\mathrm{e})_i}(\zeta) = \psi''_{(\mathrm{e})_i}\left(h_\mathrm{e} \frac{1+\zeta}{2} \right)$. The ζ_p and $w_p\,(p = 1, 2, \ldots n_\mathrm{g})$ are the Gauss integration points and their corresponding weights.

The dynamics of hysteretic dissipating moments at the Gauss points within an element are governed by the equations

$$\begin{aligned} \frac{\mathrm{d}}{\mathrm{d}t}\overline{z}_{(\mathrm{e})_p} = \left(\bar{A} - \alpha\, \mathrm{sign}\left(\overline{z}_{(\mathrm{e})_p} \frac{\mathrm{d}}{\mathrm{d}t}\chi_{(\mathrm{e})_p} \right) \left| \overline{z}_{(\mathrm{e})_p} \right|^{n_\mathrm{h}} - \beta \left| \overline{z}_{(\mathrm{e})_p} \right|^{n_\mathrm{h}} \right) \times \\ \frac{\mathrm{d}}{\mathrm{d}t}\chi_{(\mathrm{e})_p},\ \ p \in \{1, 2, \ldots, n_\mathrm{g}\} \end{aligned} \tag{A.4}$$

where $\chi_{(\mathrm{e})_p} = \sum_{i=1}^{4} \overline{\psi}''_{(\mathrm{e})_i}(\zeta_p) q_{(\mathrm{e})_i}(t)$ is the curvature at the p^{th} Gauss point.

$$\boldsymbol{Q}_{(\mathrm{e})} = \mathbf{A}_{(\mathrm{e})} \overline{\boldsymbol{z}}_{(\mathrm{e})},\ \boldsymbol{\chi}_{(\mathrm{e})} = \overline{\boldsymbol{\Psi}}_{(\mathrm{e})}{}^{\top} \boldsymbol{q}_{(\mathrm{e})},\ \mathbf{A}_{(\mathrm{e})} = \frac{\gamma_\mathrm{h}\, h_\mathrm{e}}{2} \overline{\boldsymbol{\Psi}}_{(\mathrm{e})}\, \mathbf{W}, \tag{A.5}$$

where

$$\begin{aligned} \left[\overline{\boldsymbol{\Psi}}_{(\mathrm{e})} \right]_{ip} &= \overline{\psi}''_{(\mathrm{e})_i}(\zeta_p),\ \mathbf{W} = \mathrm{diag}([\zeta_1, \zeta_2, \ldots, \zeta_{n_\mathrm{g}}]), \\ \overline{\boldsymbol{z}}_{(\mathrm{e})} &= [\overline{z}_{(\mathrm{e})_1}, \overline{z}_{(\mathrm{e})_2}, \ldots, \overline{z}_{(\mathrm{e})_{n_\mathrm{g}}}]^{\top},\ i \in \{1, 2, 3, 4\},\ \text{and} \\ p &\in \{1, 2, \ldots, n_\mathrm{g}\}. \end{aligned} \tag{A.6}$$

Appendix B

A numerical example for the algorithm proposed in 2.4.2.1

In this abstract we present a numerical example to demonstrate the algorithm described in section 2.4.2.1. The variables introduced here are not related to the analyses presented in the main body of the thesis.

Let us consider a 4×6 input matrix of normally distributed numbers.

$$\mathbf{A} = \begin{bmatrix} 0.5377 & 0.3188 & 3.5784 & 0.7254 & -0.1241 & 0.6715 \\ 1.8339 & -1.3077 & 2.7694 & -0.0631 & 1.4897 & -1.2075 \\ -2.2588 & -0.4336 & -1.3499 & 0.7147 & 1.4090 & 0.7172 \\ 0.8622 & 0.3426 & 3.0349 & -0.2050 & 1.4172 & 1.6302 \end{bmatrix}.$$

The row numbers chosen according to the algorithm are stored in the row matrix $\mathbf{s}$ which is the output of this algorithm. For now, $\mathbf{s}$ is empty. After every iteration of the algorithm, an integer denoting a row number is appended to $\mathbf{s}$. As the matrix $\mathbf{A}$ has 4 rows, $\mathbf{s}$ will finally have 4 elements.

The row norms of $\mathbf{A}$ are

$$\mathbf{R}_{\mathrm{A}} = \begin{Bmatrix} 3.7667 \\ 4.0527 \\ 3.1816 \\ 3.8444 \end{Bmatrix}.$$

We see that the second row has the largest norm. Hence, we assign

$$\mathbf{s} = [2].$$

Rearranging the rows of $\mathbf{A}$ according to the descending order of row norms, we get the matrix

$$\mathbf{A}_1 = \begin{bmatrix} 1.8339 & -1.3077 & 2.7694 & -0.0631 & 1.4897 & -1.2075 \\ 0.8622 & 0.3426 & 3.0349 & -0.2050 & 1.4172 & 1.6302 \\ 0.5377 & 0.3188 & 3.5784 & 0.7254 & -0.1241 & 0.6715 \\ -2.2588 & -0.4336 & -1.3499 & 0.7147 & 1.4090 & 0.7172 \end{bmatrix}.$$

In the matrix $\mathbf{A}_1$, the rows of matrix $\mathbf{A}$ are arranged in the order

$$\mathbf{p} = [2 \quad 4 \quad 1 \quad 3], \tag{B.1}$$

and the first row of $\mathbf{A}_1$, say $\mathbf{r}_{\max}$, has the highest norm. In the next step we subtract from the rest of the rows their respective components along $\mathbf{r}_{\max}$, i.e.,

$$\mathbf{A}_1(k,:) \to \mathbf{A}_1(k,:) - \frac{(\mathbf{A}_1(k,:) \cdot \mathbf{r}_{\max})}{||\mathbf{r}_{\max}||^2}\, \mathbf{r}_{\max}, \quad k = 2, 3, 4.$$

The matrix $\mathbf{A}_1$, after the row operations, transforms into

$$\mathbf{A}_1 = \begin{bmatrix} 1.8339 & -1.3077 & 2.7694 & -0.0631 & 1.4897 & -1.2075 \\ -0.2202 & 1.1144 & 1.4004 & -0.1678 & 0.5380 & 2.3429 \\ -0.5161 & 1.0702 & 1.9870 & 0.7617 & -0.9801 & 1.3654 \\ -1.5748 & -0.9214 & -0.3170 & 0.6912 & 1.9646 & 0.2668 \end{bmatrix}.$$

The row norms of the transformed $\mathbf{A}_1$ is

$$\mathbf{R}_{\mathbf{A}_1} = \begin{Bmatrix} 4.0527 \\ 3.0097 \\ 2.9606 \\ 2.7996 \end{Bmatrix}.$$

We can see that the second row of $\mathbf{A}_1$ has the second largest row norm which corresponds to the fourth row of the main matrix $\mathbf{A}$ (see Eq. B.1). Hence, we modify

$$\mathbf{s} = [2,\ 4].$$

Similar steps have to be followed to find the rest of the entries of $\mathbf{s}$.

Appendix C

Finite element analysis of a Rayleigh beam

For the finite element analysis of the Rayleigh beam, the effect of rotary inertia is to be incorporated in the mass matrix. However, the stiffness matrix remains same as that of Euler-Bernoulli beams. For the i^{th} element of size $\ell_{(i)}$, the element mass and stiffness matrices are given by

$$\mathbf{M}_{(i)} = \frac{\rho A}{420}\begin{bmatrix} 156\,\ell_{(i)} & 22\,\ell_{(i)}^2 & 54\,\ell_{(i)} & -13\,\ell_{(i)}^2 \\ 22\,\ell_{(i)}^2 & 4\,\ell_{(i)}^3 & 13\,\ell_{(i)}^2 & -3\,\ell_{(i)}^3 \\ 54\,\ell_{(i)} & 13\,\ell_{(i)}^2 & 156\,\ell_{(i)} & -22\,\ell_{(i)}^2 \\ -13\,\ell_{(i)}^2 & -3\,\ell_{(i)}^3 & -22\,\ell_{(i)}^2 & 4\,\ell_{(i)}^3 \end{bmatrix} + \frac{\rho I}{30}\begin{bmatrix} 36 & 3\,\ell_{(i)} & -36 & 3\,\ell_{(i)} \\ 3\,\ell_{(i)} & 4\,\ell_{(i)}^2 & -3\,\ell_{(i)} & -\ell_{(i)}^2 \\ -36 & -3\,\ell_{(i)} & 36 & -3\,\ell_{(i)} \\ 3\,\ell_{(i)} & -\ell_{(i)}^2 & -3\,\ell_{(i)} & 4\,\ell_{(i)}^2 \end{bmatrix} \tag{C.1}$$

$$\mathbf{K}_{(i)} = \frac{EI}{\ell_{(i)}^3} \begin{bmatrix} 12 & 6\,\ell_{(i)} & -12 & 6\,\ell_{(i)} \\ 6\,\ell_{(i)} & 4\,\ell_{(i)}^2 & -6\,\ell_{(i)} & 2\,\ell_{(i)}^2 \\ -12 & -6\,\ell_{(i)} & 12 & -6\,\ell_{(i)} \\ 6\,\ell_{(i)} & 2\,\ell_{(i)}^2 & -6\,\ell_{(i)} & 4\,\ell_{(i)}^2 \end{bmatrix} \tag{C.2}$$

The assembly of the global mass ($\mathbf{M}$) and stiffness ($\mathbf{K}$) matrices is routine [61]. We consider n_{e} equal-length elements for simplicity. The assembled non-homogeneous equations are of the form

$$\mathbf{M}\,\ddot{\boldsymbol{y}} + \mathbf{K}\,\boldsymbol{y} = \boldsymbol{f}, \tag{C.3}$$

where $\boldsymbol{y}$ is the global nodal coordinate vector. In our problem the forcing vector $\boldsymbol{f}$ has all elements equal to zero except $\delta(\tau)$ (Dirac delta function) at the nodal entry corresponding to the rotational degree of freedom at $x = \frac{L}{2}$. Alternatively, we can formulate an equivalent homogeneous equation of motion

$$\mathbf{M}\,\ddot{\boldsymbol{y}} + \mathbf{K}\,\boldsymbol{y} = \mathbf{0} \tag{C.4}$$

with initial conditions

$$\boldsymbol{y}(0) = \mathbf{0}, \qquad \text{and} \qquad \dot{\boldsymbol{y}}(0) = \mathbf{M}^{-1}\,\hat{\boldsymbol{f}} \tag{C.5}$$

where the vector $\hat{\boldsymbol{f}}$ has all elements zero except a '1' at the nodal entry corresponding to the rotational degree of freedom at $x = \frac{L}{2}$. For time integration of Eq. C.4, we have used the implicit time marching algorithm of Piché [32]. We mention that that algorithm has given very good results in some other recent work with slender structures [62].

Appendix D

Proof of Lemma 1

Let us consider a real valued, several-times differentiable function g with the properties $g(x) \to 0$ as $x \to \infty$. Moreover, successive derivatives of g go to zero faster and faster as $x \to \infty$. Then

$$\begin{aligned}\int_N^\infty g(y)\,\mathrm{d}y &= \sum_{k=N}^{\infty}\int_k^{k+1} g(y)\;\mathrm{d}y \\ &\sim \sum_{k=N}^{\infty}\int_k^{k+1}\left(g(k)+(y-k)g'(k)+\frac{1}{2}(y-k)^2g''(k)+\frac{1}{6}(y-k)^3g'''(k)+\cdots\right)\mathrm{d}y \\ &= \sum_{k=N}^{\infty} g(k)+\frac{1}{2}\sum_{k=N}^{\infty} g'(k)+\frac{1}{6}\sum_{k=N}^{\infty} g''(k)+\frac{1}{24}\sum_{k=N}^{\infty} g'''(k)+\frac{1}{120}\sum_{k=N}^{\infty} g''''(k)+\cdots .\end{aligned}$$

Rearranging,

$$\sum_{k=N}^{\infty} g(k) = \int_N^\infty g(y)\,\mathrm{d}y - \frac{1}{2}\sum_{k=N}^{\infty} g'(k) - \frac{1}{6}\sum_{k=N}^{\infty} g''(k) - \frac{1}{24}\sum_{k=N}^{\infty} g'''(k) - \frac{1}{120}\sum_{k=N}^{\infty} g''''(k) + \cdots . \tag{D.1}$$

The same equation can be used recursively on the sums on the right hand side; the advantage in such cases is that the antiderivatives are obvious. More terms can be retained easily if we wish. In this way, we obtain Eq. 3.20.

Appendix E

Infinite series and their sum

Some infinite series are listed below. They can be obtained using some tricks with Fourier series; and they can also be obtained from symbolic algebra packages like Maple. Proofs are omitted.

$$\sum_{k=1}^{\infty} \frac{1}{1+4\,k^2\,a^2} = \frac{1}{4\,a}\left(-2\,a+\pi\coth\left(\frac{\pi}{2\,a}\right)\right) \tag{E.1}$$

$$\sum_{k=1}^{\infty} \frac{1}{(1+4\,k^2\,a^2)^2} = \frac{1}{16\,a^2}\left(\pi^2\left(\coth\left(\frac{\pi}{2\,a}\right)\right)^2-8\,a^2+2\,\pi\coth\left(\frac{\pi}{2\,a}\right)a-\pi^2\right) \tag{E.2}$$

$$\begin{aligned}\sum_{k=1}^{\infty} \frac{1}{(1+4\,k^2\,a^2)^3} = \frac{1}{64\,a^3}&\left(\left(\coth\left(\frac{\pi}{2\,a}\right)\right)^3\pi^3+3\left(\coth\left(\frac{\pi}{2\,a}\right)\right)^2\pi^2 a-32\,a^3\right)\\ &+\frac{1}{64\,a^3}\left(-\coth\left(\frac{\pi}{2\,a}\right)\pi^3+6\,\pi\coth\left(\frac{\pi}{2\,a}\right)a^2-3\,\pi^2 a\right)\end{aligned} \tag{E.3}$$

Appendix F

Parallelism of vectors $\boldsymbol{p}$ and $\boldsymbol{q}$

The leading order term of Eq. 4.14 is

$$\begin{aligned}\int_0^b -y'(x)\, v_x \,\mathrm{d}x &= -y'(x)\, v \Big|_0^b + \int_0^b y''(x)\, v \,\mathrm{d}\xi \\ &= \int_0^b y''(x)\, v \,\mathrm{d}x \\ &= \int_0^b \frac{1}{W} \sec(\theta(x))\, v \,\mathrm{d}x \quad \text{(referring Eq. 4.4)} \\ &= \frac{1}{W} \int_0^b \sec(\theta(x))\, v \,\mathrm{d}x. \end{aligned} \tag{F.1}$$

The potential energy is

$$\mathcal{V} = \int_0^b \bar{m}\, g\, v\, \sec(\theta(x)) \,\mathrm{d}\xi = \bar{m}\, g \int_0^b \sec(\theta(x))\, v \,\mathrm{d}\xi. \tag{F.2}$$

Since the same v appears in both integrals above, they differ only up to a multiplicative constant. This is why $\boldsymbol{p}$ and $\boldsymbol{q}$ are parallel.

Bibliography

[1] Handral, P., and Rangarajan, R., 2020, An elastica robot: Tip-control in tendon-actuated elastic arms, *Extreme Mechanics Letters*, 34: 100584.

[2] Kimball, A. L., and Lovell, D. E., 1927, Internal friction in solids, *Physical Review*, 30(6): 948.

[3] Muravskii, G. B., 2004, On frequency independent damping, *Journal of Sound and Vibration*, 274(3-5): 653-668.

[4] Chapra, S. C., and Canale, R. P., 2011, *Numerical methods for engineers*, Vol. 1221, Mcgraw-hill, New York.

[5] Bouc, R., 1967, Forced vibrations of mechanical systems with hysteresis, *Proceedings of the Fourth Conference on Nonlinear Oscillations, Prague.*

[6] Wen, Yi-Kwei., 1976, Method for random vibration of hysteretic systems, *Journal of the Engineering Mechanics Division*, 102(2): 249-263.

[7] Visintin, A., 2013, *Differential models of hysteresis*, Springer Science and Business Media, Vol. 111.

[8] Vaiana, N., Sessa, S., Marmo, F., Rosati, L., 2019, Nonlinear dynamic analysis of hysteretic mechanical systems by combining a novel rate-independent model and an explicit time integration method, *Nonlinear Dynamics*, 98(4): 2879-2901.

[9] Chang, S. Y., 2010, A new family of explicit methods for linear structural dynamics, *Computers and Structures*, 88(11-12): 755-772.

[10] Abaqus, G., 2011, Abaqus 6.11, *Dassault Systemes Simulia Corporation*, Providence, RI, USA.

[11] MATLAB, 2010, *version 7.10.0* (R2010a), *The MathWorks Inc*, Natick, Massachusetts.

[12] Newmark, N. M., 1959, A method of computation for structural dynamics. *Journal of the Engineering Mechanics Division*, 85(3): 67-94.

[13] Bathe, K. J., 2007, Conserving energy and momentum in nonlinear dynamics: a simple implicit time integration scheme, *Computers and Structures*, 85(7-8): 437-445.

[14] Lee, T. Y., Chung, K. J., and Chang, H., 2017, A new implicit dynamic finite element analysis procedure with damping included, *Engineering Structures*, 147: 530-544.

[15] Hilber, H. M., Hughes, T. J., and Taylor, R. L., 1977, Improved numerical dissipation for time integration algorithms in structural dynamics, *Earthquake Engineering and Structural Dynamics*, 5(3): 283-292.

[16] Triantafyllou, S. P., and Koumousis, V. K., 2014, Hysteretic finite elements for the nonlinear static and dynamic analysis of structures, *Journal of Engineering Mechanics*, 140(6): 04014025.

[17] Mosqueda, G., and Ahmadizadeh, M., 2007, Combined implicit or explicit integration steps for hybrid simulation, *Earthquake Engineering and Structural Dynamics*, 36(15): 2325-2343.

[18] Mosqueda, G., and Ahmadizadeh, M., 2011, Iterative implicit integration procedure for hybrid simulation of large nonlinear structures, *Earthquake Engineering and Structural Dynamics*, 40(9): 945-960.

[19] Guyan, R. J., 1965, Reduction of stiffness and mass matrices, *AIAA Journal*, 3(2): 380-380.

[20] Irons, B., 1965, Structural eigenvalue problems-elimination of unwanted variables, *AIAA Journal*, 3(5): 961-962.

[21] Rouleau, L., Deü, J. F., and Legay, A., 2017, A comparison of model reduction techniques based on modal projection for structures with frequency-dependent damping, *Mechanical Systems and Signal Processing*, 90: 110-125.

[22] Golub, G. H., and Van Loan, C. F., 2013, *Matrix Computations*, John Hopkins University Press, Baltimore, 4^{th} edition.

[23] Stringer, D. B., Sheth, P. N., and Allaire, P. E., 2011, Modal reduction of geared rotor systems with general damping and gyroscopic effects, *Journal of Vibration and Control*, 17(7): 975-987.

[24] Samantaray, A. K., 2009, Steady-state dynamics of a non-ideal rotor with internal damping and gyroscopic effects, *Nonlinear Dynamics*, 56(4): 443-451.

[25] Bhattacharyya, S., and Cusumano, J. P., 2021, An energy closure criterion for model reduction of a kicked Euler–Bernoulli beam, *Journal of Vibration and Acoustics*, 143(4): 041001.

[26] Bhattacharyya, S., and Cusumano, J. P., 2021, Experimental implementation of energy closure analysis for reduced order modeling, *Journal of Vibration and Acoustics*, 1-30.

[27] Chatterjee, A., 2000, An introduction to the proper orthogonal decomposition, *Current Science*, 808-817.

[28] Sengupta, T. K., Haider, S. I., Parvathi, M. K., and Pallavi, G., 2015, Enstrophy-based proper orthogonal decomposition for reduced-order modeling of flow past a cylinder, *Physical Review E*, 91(4): 043303.

[29] Clark, S. T., Besem, F. M., Kielb, R. E., and Thomas, J. P., 2015, Developing a reduced-order model of nonsynchronous vibration in turbomachinery using proper-orthogonal decomposition methods, *Journal of Engineering for Gas Turbines and Power*, 137(5): 052501.

[30] Berkooz, G., Holmes, P., and Lumley, J. L., 1993, The proper orthogonal decomposition in the analysis of turbulent flows, *Annual Review of Fluid Mechanics*, 25(1): 539-575.

[31] Holmes, P. J., Lumley, J. L., Berkooz, G., Mattingly, J. C., and Wittenberg, R. W., 1997, Low-dimensional models of coherent structures in turbulence, *Physics Reports*, 287(4): 337-384.

[32] Piché, R., 1995, An L-stable Rosenbrock method for step-by-step time integration in structural dynamics, *Computer Methods in Applied Mechanics and Engineering*, 126(3-4): 343-354.

[33] Wanner, G., and Hairer. E., 1996, *Solving ordinary differential equations II*, Vol. 375. Springer, Berlin, Heidelberg.

[34] Maiti, S., Bandyopadhyay, R., and Chatterjee, A., 2018, Vibrations of an Euler-Bernoulli beam with hysteretic damping arising from dispersed frictional microcracks, *Journal of Sound and Vibration*, 412: 287-308.

[35] Orban, F., 2011, Damping of materials and members in structures, *Journal of Physics: Conference Series,* Vol. 268., No. 1., IOP Publishing.

[36] Bhattacharjee, A., and Chatterjee, A., 2013, Dissipation in the Bouc–Wen model: small amplitude, large amplitude and two-frequency forcing, *Journal of Sound and Vibration*, 332(7): 1807-1819.

[37] Timoshenko, S. P., 2003, *History of Strength of Materials*, Dover, USA.

[38] Graff, K. F., 1975, *Wave Motion in Elastic Solids*, Oxford University Press, Oxford, UK.

[39] Rayleigh, J. W. S., 1945, *Theory of Sound*, Dover, USA.

[40] Timoshenko, S. P., 1921, On the correction for shear of the differential equation for transverse vibrations of prismatic bars, *Philosophical Magazine*, 41(245): 744-746.

[41] Timoshenko, S. P., 1922, On the transverse vibrations of bars of uniform cross-section, *The London, Edinburgh, and Dublin Philosophical Magazine and Journal of Science*, 43(253): 125-131.

[42] Meirovitch, L., 1997, *Principles and Techniques of Vibrations*, Prentice-Hall, USA.

[43] Chatterjee, A., 2004, The short-time impulse response of Euler-Bernoulli beams, *Journal of Applied Mechanics, ASME*, 71(2): 208-218.

[44] Zener, C., 1941, The intrinsic inelasticity of large plates, *Physical Review*, 59(8): 669.

[45] Schwieger, H., 1965, A simple calculation of the transverse impact on beams and its experimental verification, *Experimental Mechanics*, 5(11): 378-384.

[46] Schwieger, H., 1970, Central deflection of a transversely struck beam, *Experimental Mechanics*, 10(4): 166-169.

[47] Meijaard, J., 2007, Lateral impacts on flexible beams in multibody dynamics simulations, *In IUTAM Symposium on Multiscale Problems in Multibody System Contacts, Springer, Dordrecht*, 173-182.

[48] Bhattacharjee, A., and Chatterjee, A., 2018, Transverse impact of a Hertzian body with an infinitely long Euler-Bernoulli beam, *Journal of Sound and Vibration*, 429: 147-161.

[49] Claeyssen, J. R., Chiwiacowsky, L. D., and Suazo, G. C., 2002, The impulse response in the symbolic computing of modes for beams and plates, *Applied Numerical Mathematics*, 40(1-2): 119-135.

[50] Roy, P. K., and Ganesan, N., 1995, Transient response of a cantilever beam subjected to an impulse load, *Journal of Sound and Vibration*, 183(5): 873-880.

[51] Barkanov, E., Rikards, R., Holste, C., and Täger, O., 2000, Transient response of sandwich viscoelastic beams, plates, and shells under impulse loading, *Mechanics of Composite Materials*, 36(3): 215-222.

[52] Jayaprakash, K., Desai, Y. M., and Naik, N. K., 2013, Fatigue behavior of $[0_n/90_n]_s$ composite cantilever beam under tip impulse loading, *Composite Structures*, 99: 255-263.

[53] Wagg, D. J., Karpodinis, G., and Bishop, S. R., 1999, An experimental study of the impulse response of a vibro-impacting cantilever beam, *Journal of Sound and Vibration*, 228(2): 243-264.

[54] Bhattacharjee, A., and Chatterjee, A., 2020, Restitution modeling in vibration-dominated impacts using energy minimization under outward constraints, *International Journal of Mechanical Sciences*, 166: 105215.

[55] Kenny, S., Pegg, N., and Taheri, F., 2000, Dynamic elastic buckling of a slender beam with geometric imperfections subject to an axial impulse, *Finite Elements in Analysis and Design*, 35(3): 227-246.

[56] Langhaar, H. L., 1951, *Dimensional Analysis and Theory of Models*, John Wiley & Sons (reprinted in 1987 by the Robert E. Krieger Publishing Company, Malabar, FL).

[57] Hagedorn, P., and Dasgupta A., 2007, *Vibration and Waves in Continuous Mechanical Systems*, John Wiley, West Sussex, England.

[58] Gopalakrishnan, S., 2017, *Wave Propagation in Materials and Structures*, CRC Press, USA.

[59] Eringen, A. C., 2002, *Nonlocal Continuum Field Theories*, Springer, USA.

[60] Bender, C. M., and Orszag, S., 1999, *Advanced Mathematical Methods for Scientists and Engineers: Asymptotic Methods and Perturbation Theory*, Springer Science and Business Media.

[61] Cook, R. D., Malkus, D. S., Plesha, M. E., 2000, *Concepts and Applications of Finite Element Analysis*, John Wiley, USA.

[62] Goswami, B., and Chatterjee, A., 2023, Semi-implicit integration and data-driven model order reduction in structural dynamics with hysteresis, *Journal of Computational and Nonlinear Dynamics, ASME*, 18(5): 051002.

[63] Routh, E. J., 1905, *The Advanced Part of A Treatise on the Dynamics of a System of Rigid Bodies: Being Part II of a Treatise on the Whole Subject*, MacMillan and Company, Newyork.

[64] Gelfand, I. M., and Fomin, S. V., 1963, *Calculus of Variations*, Prentice-Hall. Inc., Englewood Cliffs.

[65] Pugsley, A. G., 1949, On the natural frequencies of suspension chains, *The Quarterly Journal of Mechanics and Applied Mathematics*, 2(4): 412-418.

[66] Saxon, D. S., and Cahn, A. S., 1953, Modes of vibration of a suspended chain, *The Quarterly Journal of Mechanics and Applied Mathematics*, 6(3): 273-285.

[67] Goodey, W., 1961, On the natural modes and frequencies of a suspended chain, *The Quarterly Journal of Mechanics and Applied Mathematics*, 14(1): 118-127.

[68] Irvine, H. M., and Caughey, T. K., 1974, The linear theory of free vibrations of a suspended cable, *Proceedings of the Royal Society of London. A. Mathematical and Physical Sciences*, 341(1626): 299-315.

[69] Simpson, A., 1966, Determination of the in-plane natural frequencies of multispan transmission lines by a transfer-matrix method, *Proceedings of the Institution of Electrical Engineers*, 113(5): 870-878.

[70] Gambhir, M. L., and Batchelor, B. D., 1979, Finite element study of the free vibration of 3-D cable networks, *International Journal of Solids and Structures*, 15(2): 127-136.

[71] Ahmadi-kashani, K., 1989, Vibration of hanging cables, *Computers and Structures*, 31(5): 699-715.

[72] Karoumi, R., 1999, Some modeling aspects in the nonlinear finite element analysis of cable supported bridges, *Computers and Structures*, 71(4): 397-412.

[73] Rega, G., 2004, Nonlinear vibrations of suspended cables, part I: Modeling and analysis, *Applied Mechanics Reviews*, 57(6): 443-478.

[74] Rega, G., 2004, Nonlinear vibrations of suspended cables, part II: Deterministic phenomena, *Applied Mechanics Reviews*, 57(6): 479-514.

[75] Bridge, J., and Keshavan, S., 2007, Vibration characteristics of a bi-density drumhead, *Mechanics Research Communications*, 34(3): 267-274.

[76] Chun, S. B., and Lee, C. W., 1996, Vibration analysis of shaft-bladed disk system by using substructure synthesis and assumed modes method, *Journal of Sound and Vibration*, 189(5): 587-608.

[77] Lee, C. W., and Chun, S. B., 1998, Vibration analysis of a rotor with multiple flexible disks using assumed modes method, *ASME Journal of Vibration and Acoustics*, 120(1): 87-94.

[78] Tadikonda, S. S. K., Mordfin, T. G., and Hu, T. G., 1995, Assumed modes method and articulated flexible multibody dynamics, *Journal of Guidance, Control, and Dynamics*, 18(3): 404-410.

[79] Erturk, A., 2012, Assumed-modes modeling of piezoelectric energy harvesters: Euler–Bernoulli, Rayleigh, and Timoshenko models with axial deformations, *Computers and Structures*, 106: 214-227.

[80] Celentano, L., and Coppola, A., 2011, A computationally efficient method for modeling flexible robots based on the assumed modes method, *Applied Mathematics and Computation*, 218(8): 4483-4493.

[81] D'Antonio, D. S., Cardona, G. A., and Saldaña, D., 2021, The catenary robot: Design and control of a cable propelled by two quadrotors, *IEEE Robotics and Automation Letters*, 6(2): 3857-3863.

[82] Zhu, H., Hu, J., Gao, Y., Zhao, H., and Xu, W., 2021, Spatial–temporal mode transition in vortex-induced vibration of catenary flexible riser, *Journal of Fluids and Structures*, 102: 103234.

[83] Rucker, D. C., and Webster III, R. J., 2011, Statics and dynamics of continuum robots with general tendon routing and external loading, *IEEE Transactions on Robotics*, 27(6): 1033-1044.

[84] Love, A. E. H., 1944, *A treatise on the mathematical theory of elasticity*, 4th edition, Dover, New York.

[85] Euler, L., 1744, *De curvis elasticis, Methodus inveniendi lineas curvas.*

[86] Antman, S. S., and Kenney, C. S., 1981, Large buckled states of nonlinearly elastic rods under torsion, thrust, and gravity, *Archive for Rational Mechanics and Analysis*, 76: 289-338.

[87] Caflisch, R. E., and Maddocks, J. H., 1984, Nonlinear dynamical theory of the elastica, *Proceedings of the Royal Society of Edinburgh Section A: Mathematics*, 99(1-2): 1-23.

[88] Whitman, A. B., and DeSilva, C. N., 1970, Dynamics and stability of elastic Cosserat curves, *International Journal of Solids and Structures*, 6(4): 411-422.

[89] Rubin, M. B., 2001, Numerical solution procedures for nonlinear elastic rods using the theory of a Cosserat point, *International journal of solids and structures*, 38(24-25): 4395-4437.

[90] Hsu, C. S., 1967, The effects of various parameters on the dynamic stability of a shallow arch, *ASME Journal of Applied Mechanics*, 34(2): 349-358.

[91] Perkins, N. C., 1990, Planar vibration of an elastica arch: Theory and experiment, *ASME Journal of Vibration and Acoustics*, 112(3): 374-379.

[92] Arreaga, G., Capovilla, R., Chryssomalakos, C., and Guven, J., 2002, Area-constrained planar elastica, *Physical Review E*, 65(3): 031801.

[93] Denoël, V., and Detournay, E., 2011, Eulerian formulation of constrained elastica, *International Journal of Solids and Structures*, 48(3-4): 625-636.

[94] Pocheau, A., and Roman, B., 2004, Uniqueness of solutions for constrained elastica, *Physica D: Nonlinear Phenomena*, 192(3-4): 161-186.

[95] Bayo, E., 1987, A finite-element approach to control the end-point motion of a single-link flexible robot, *Journal of Robotic Systems*, 4(1): 63-75.

[96] Catto, E. S., 1996, *Modeling and control of a cable actuated elastica manipulator*, Cornell University.

[97] Hirose, S., and Yamada, H., 2009, Snake-like robots (Tutorial), *IEEE Robotics and Automation Magazine*, 16(1): 88-98.

[98] Kato, T., Okumura, I., Song, S. E., Golby, A. J., and Hata, N., 2014, Tendon-driven continuum robot for endoscopic surgery: Preclinical development and validation of a tension propagation model, *IEEE/ASME Transactions on Mechatronics*, 20(5): 2252-2263.

[99] Armanini, C., Dal Corso, F., Misseroni, D., and Bigoni, D., 2017, From the elastica compass to the elastica catapult: An essay on the mechanics of soft robot arm, *Proceedings of the Royal Society A: Mathematical, Physical and Engineering Sciences*, 473(2198): 20160870.

[100] Nappi, F., Carotenuto, A. R., Avtaar Singh, S. S., Mihos, C., and Fraldi, M., 2019, Euler's elastica-based biomechanics of the papillary muscle approximation in ischemic mitral valve regurgitation: A simple 2D analytical model, *MDPI Materials*, 12(9): 1518.

[101] Wang, C. Y., 1986, A critical review of the heavy elastica, *International Journal of Mechanical Sciences*, 28(8): 549-559.

[102] Wang, C. Y., 2012, Large post-buckling of heavy tapered elastica cantilevers and its asymptotic analysis, *Archives of Mechanics*, 64(2): 207-220.

[103] Chen, J. S., and Lin, Y. C., 2013, Vibration and stability of a long heavy elastica on rigid foundation, *International Journal of Nonlinear Mechanics*, 50: 11-18.

[104] Pippard, A. B., 1990, The elastic arch and its modes of instability, *European Journal of Physics*, 11(6): 359.

[105] Patrício, P., Adda-Bedia, M., and Amar, M. B., 1998, An elastica problem: instabilities of an elastic arch, *Physica D: Nonlinear Phenomena*, 124(1-3): 285-295.

[106] Basak, A., Nandakumar, K., and Chatterjee, A., 2011, Decoupled three-dimensional finite element computation of thermoelastic damping using Zener's approximation, *Meccanica*, 46: 371-381.